

Molecular Self-Assembly of Surfactants on Solid Surfaces

Manaswee Suttipong

A dissertation submitted in partial fulfilment of

the requirements for the degree of

Doctor of Philosophy

of the

University College London

Department of Chemical Engineering

University College London

United Kingdom

Primary Supervisor

Prof. Alberto Striolo

April 2016

Declaration of Originality

I, Manaswee Suttipong confirm that the work presented in this thesis is my own. Where information has been derived from other sources, I confirm that this has been indicated in the thesis.

Abstract

Understanding adsorption and aggregation of surfactants on solid surfaces is of great importance to many applications. The aim of this thesis is to obtain molecular-level knowledge regarding the role of (1) surfactant-assisted aqueous dispersions of single-walled carbon nanotubes (SWNTs) and (2) surfactant adsorption on heterogeneous surfaces, using computer simulations. For the first objective, molecular dynamics simulations were employed to study the morphology of surfactants self-assembled on (6,6), (12,12), and (20,20) SWNTs. The results show that the surfactant molecular architecture significantly affects the packing of surfactants on SWNTs. The branched sodium dodecyl benzenesulfonate (SDBS) is more effective in stabilising dispersions of narrow SWNTs than its linear counterpart. There is no strong effect of the nanotube diameter seen on the morphology of mixed linear and branched SDBS. Comparing the self-assembled aggregates formed by caesium (Cs^+) and sodium (Na^+) dodecyl sulphate surfactants, Cs^+ ions yield a more compact coverage on the (6,6) SWNT, compared to Na^+ . These outcomes could provide physical guidelines for designing surfactant formulations to improve the quality of the aqueous SWNT dispersions. For the second objective, dissipative particle dynamics simulations were used to investigate the adsorption of surfactants near patterned surfaces. The hydrophobic patterns on which the surfactants could adsorb are surrounded by surfaces that repel the surfactants. On the surfaces containing one hydrophobic stripe, as the stripe width decreases, monolayers become hemi-cylinders, hemi-spheres, and individual surfactants, a consequence of lateral confinement. When two hydrophobic stripes are present on the surfaces, there is evidence of cooperative effects (i.e., hemi-cylindrical shells or irregular structures formed). The morphological (width and depth) and chemical (fully and partially hydrophobic) properties of the trenches predominantly affect the self-assembled surfactant aggregates. These findings could assist in understanding of surfactant adsorption on heterogeneous surfaces and perhaps in facilitating new methods for the fabrication of nano-structured surfaces.

Acknowledgements

First and foremost, I would like to express my sincere appreciation to my supervisor, Prof. Alberto Striolo for giving me the opportunity to join his research group. His professional knowledge, guidance, inspiration, encouragement and support helped me proceed throughout my study. I have appreciated all his contributions of time, effort, advices and ideas to make my Ph.D. experience productive and stimulating. Words cannot describe how fortunate I am to have him as my advisor.

Special thanks are extended to my dissertation committee members, Dr. Flor Siperstein and Dr. Christoph G. Salzmann for their time, patience and guidance throughout my thesis work. I would also like to thank Dr. Ozgur Yazaydin for serving as my secondary advisor and Prof. Brian P. Grady for the collaborations. I would like to express my gratitude towards my former advisor, Assoc. Prof. Boonyarach Kitiyanan for encouraging me to enter postgraduate school and introducing me to Prof. Alberto. Additional gratitude is given to my colleagues in Prof. Alberto's research group and friends for their friendship and assistance.

Furthermore, I wish to thank the funding sources from the Department of Chemical Engineering at the University College London (UCL), the School of Chemical, Biological and Materials Engineering at the University of Oklahoma (OU), and the US National Science Foundation (NSF). I am grateful to the Legion Supercomputer at UCL, the OU Supercomputing Centre for Education and Research (OSCER) at OU and the National Energy Research Scientific Computing Centre (NERSC) at Lawrence Berkeley National Laboratory for generous provision of computational resources.

At the end, my deepest gratitude goes to my wonderful family for their unflagging love and support throughout my life.

Manaswee Suttipong

April, 2016

Contents

Declaration of Originality	2
Abstract	3
Acknowledgements	4
Contents	5
Chapter 1 Introduction	9
Chapter 2 Simulation Model and Method	16
2.1 Molecular dynamics	16
2.1.1 Equations of motion and potential energy	16
2.1.2 Leap-frog algorithm	18
2.1.3 Treatment of non-bonded interactions	19
2.1.4 Periodic boundary conditions.....	19
2.1.5 Thermostat	20
2.2 Dissipative particle dynamics.....	21
2.2.1 Soft and repulsive potential.....	21
2.2.2 Built-in Langevin thermostat	22
2.2.3 Spring force.....	23
2.2.4 Modified velocity Verlet algorithm	24
2.2.5 Units of length and time.....	24
Chapter 3 Role of Surfactant Molecular Structure on Self Assembly: Aqueous SDBS on Carbon Nanotubes	26
3.1 Chapter overview	26
3.2 Introduction	26
3.3 Methodology	29
3.3.1 System composition	29

3.3.2	Force fields.....	30
3.3.3	Algorithms	31
3.4	Results and discussion.....	32
3.4.1	Self-assembly of linear SDBS surfactants on SWNTs	32
3.4.2	Molecular architecture effect: Adsorption of branched SDBS	42
3.5	Conclusions	48
Chapter 4 Equimolar Mixtures of Aqueous Linear and Branched SDBS Surfactants Simulated on Single-Walled Carbon Nanotubes		50
4.1	Chapter overview	50
4.2	Introduction	51
4.3	Methodology	53
4.4	Results and discussion.....	56
4.4.1	Aggregate morphology: Inspection of simulation snapshots	56
4.4.2	Effective surface coverage	59
4.4.3	Aggregate morphology: Radial density profiles	60
4.4.4	Surfactant packing arrangement on SWNT surfaces	63
4.4.5	Discussion	65
4.5	Conclusions	71
Chapter 5 Salt-Specific Effects in Aqueous Dispersions of Carbon Nanotubes ...		72
5.1	Chapter overview	72
5.2	Introduction	73
5.3	Methodology	74
5.3.1	Computational model.....	74
5.3.2	Simulated system	75
5.4	Results and discussion.....	76

5.5	Conclusions	85
Chapter 6 Self-Assembled Surfactants on Patterned Surfaces: Confinement and Cooperative Effects on Aggregate Morphology		
6.1	Chapter overview	86
6.2	Introduction	87
6.3	Methodology	89
6.4	Results and discussion.....	94
6.4.1	Adsorption on homogeneous surfaces	94
6.4.2	Lateral confinement: Effect of stripe widths.....	95
6.4.3	Cooperative effects: Adsorption on neighbouring stripes.....	102
6.5	Conclusions	107
Chapter 7 Surfactant Aggregates Templated by Lateral Confinement.....		
7.1	Chapter overview	109
7.2	Introduction	109
7.3	Methodology	111
7.4	Results and Discussion.....	113
7.5	Conclusions	125
Chapter 8 Summary and Outlook		
Appendix A	Supporting Information for Chapter 3.....	131
Appendix B	Supporting Information for Chapter 5.....	134
B.1	SDS surfactants self-assembled on (6,6) SWNTs	134
B.2	Effective surface area per surfactant headgroup	135
B.3	Radial density distributions of CsDS and SDS surfactants on (12,12) and (20,20) SWNTs	137
B.4	Orientation of adsorbed CsDS and SDS surfactants	138
B.5	Experimental validation	142

Appendix C	Supporting Information for Chapter 6.....	147
C.1	Spring constant.....	147
C.2	Simulated system.....	148
Appendix D	Supporting Information for Chapter 7.....	152
D.1	Self-assembled surfactant aggregates within fully hydrophobic trenches of width $L = 0.99L_S$, $1.91L_S$, and $3.75L_S$	152
D.2	Water-trench system.....	154
Bibliography.....		156
Curriculum Vitae.....		175

Chapter 1 Introduction

Surfactants or surface-active agents are amphiphilic compounds that can occur naturally or be made artificially. All surfactant molecules consist of at least one polar headgroup and at least one hydrophobic tail. The surfactant headgroup can be anionic, cationic, non-ionic or zwitterionic, while the surfactant tail is usually a linear or branched hydrocarbon chain [1]. Due to their dual nature, surfactants have a tendency to adsorb at interfaces. **Figure 1-1** shows a schematic representation of chemical structures of surfactants studied herein.

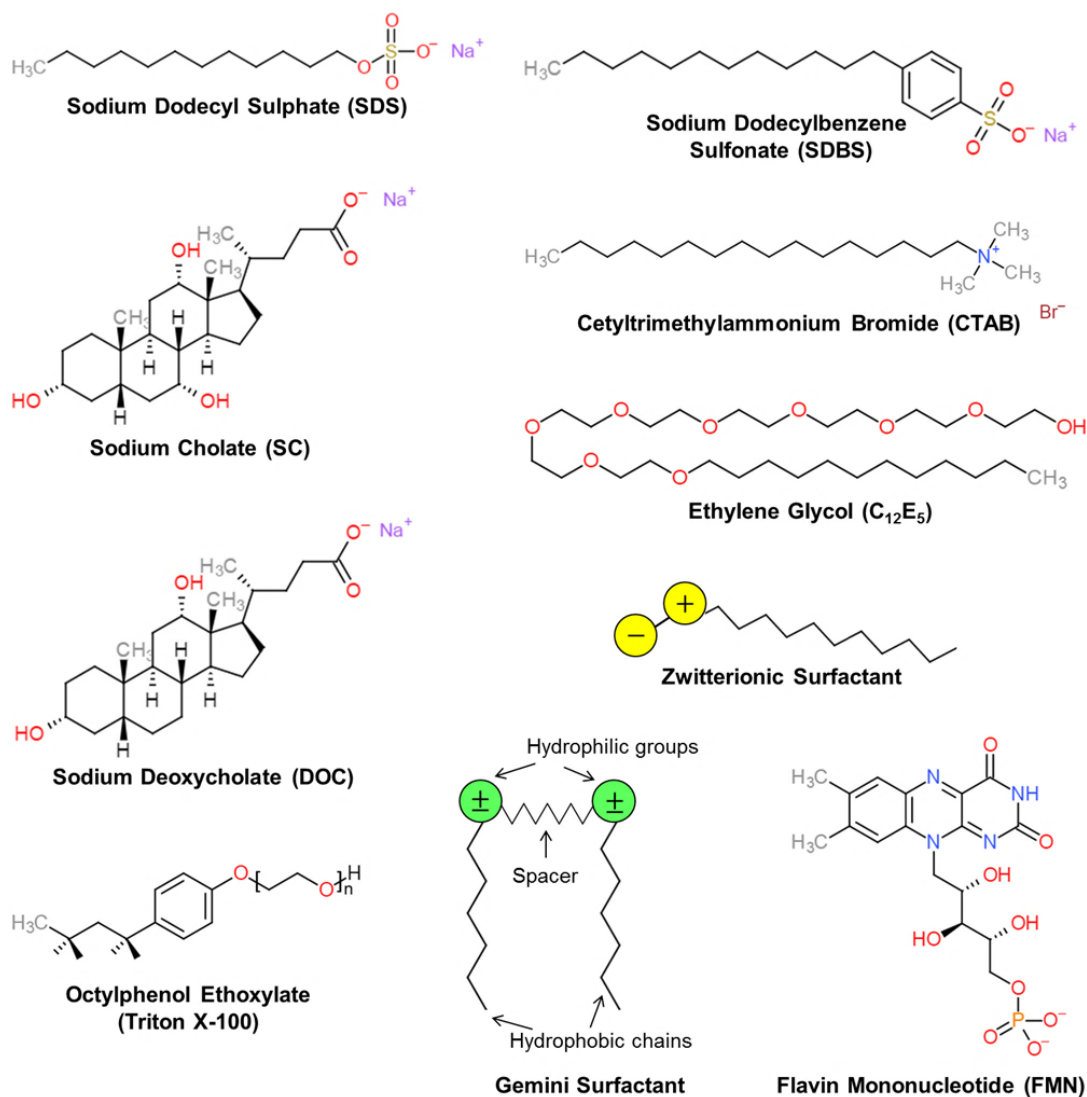


Figure 1-1: Schematic representation of all surfactants considered in this thesis.

Adsorption of surfactants at solid-liquid interfaces has received considerable attention due to its importance in a wide variety of applications. For example, via the adsorption of surfactants and their self-assemblies, it is possible to improve the graphene dispersibility in polymer matrix [2] as well as stabilise carbon nanotubes in water [3,4]. In surface modification with admicellar polymerization, the adsorbing surfactants are used to localise monomers on the surface, for subsequent polymerization [5-7]. Also, during surfactant flooding process for enhanced oil recovery, one of the retention mechanisms invoked is the adsorption of surfactants on the mineral surfaces [8]. Thus, because of their extraordinary characteristics which render their irreplaceable use for numerous applications, efforts have never run short by scientists to study about other unknown natures and properties of surfactants. Motivated by such ambition, this thesis attempts to contribute some fundamental understanding of the role of (1) surfactant-assisted aqueous dispersions of single-walled carbon nanotubes (SWNTs) and (2) surfactant adsorption and aggregation on heterogeneous surfaces.

Discovered in the early 1990s [9], SWNTs have attracted enormous interest because of their unique structure and superior properties [10]. Conceptually, SWNTs are formed by rolling up one layer of a graphene sheet, a planar array of benzene molecules involving only hexagonal rings. The choice of rolling axis relative to (1) the hexagonal network of the graphene sheet (chirality) and (2) the radius of the closed cylinder allows different types of SWNTs [11]. **Figure 1-2**, top panel, provides a schematic illustration for creating various SWNTs by rolling up a sheet of graphene along different chiral vectors $\vec{R} = n\vec{a}_1 + m\vec{a}_2$, where n and m are integers of the unit vectors \vec{a}_1 and \vec{a}_2 . For an ideal SWNT, the diameter is given by $d = \frac{a}{\pi} \sqrt{(n^2 + nm + m^2)}$, where a is the magnitude of either \vec{a}_1 or \vec{a}_2 and is equal 0.246 nm. Typically, d is in the range of 0.7-2 nm [12]. Depending on the diameter and chirality, SWNTs can be either metals or semiconductors based on the two indices (n, m) [13]. SWNTs exhibit metallic behaviour only when $n - m$ is a multiple of three. All other SWNTs are semiconducting. In bottom panel of **Figure 1-2** three types of SWNTs are given, including zigzag [e.g., (6,0)], chiral [e.g., (6,5)] and armchair [e.g., (5,5)].

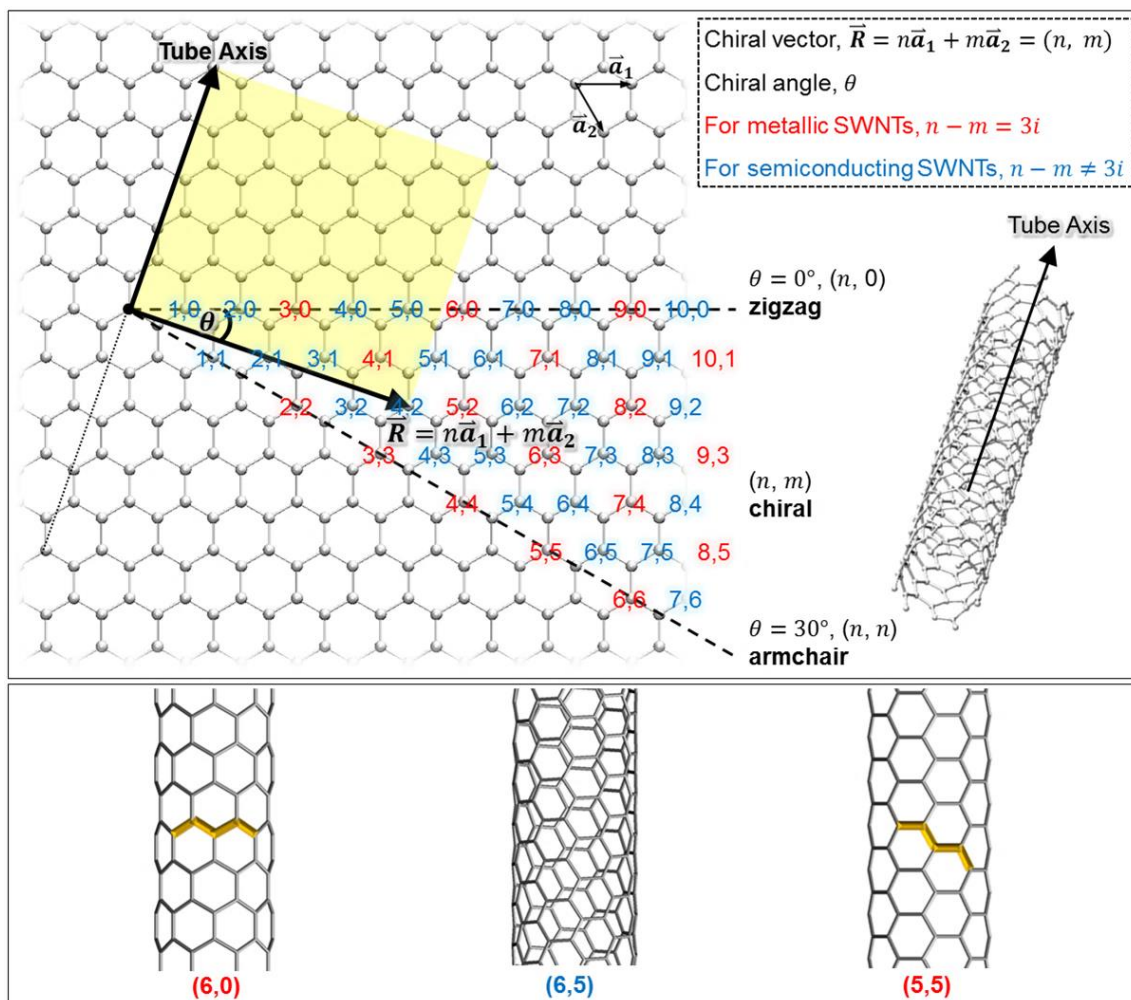


Figure 1-2: Top: a SWNT formed by a sheet of graphene with the unit vectors \vec{a}_1 and \vec{a}_2 , which define the chiral vector $\vec{R} = n\vec{a}_1 + m\vec{a}_2$. The yellow rectangle displays the unit cell of the (4,2) SWNT. When $n - m$ is a multiple of three ($n - m = 3i$ and i is a natural number), SWNTs are described as metallic (indicated by red text), otherwise the SWNTs are semiconductors (indicated by blue text). Bottom: three SWNTs with different structures, including zigzag [e.g., (6,0)], chiral [e.g., (6,5)] and armchair [e.g., (5,5)].

SWNTs are typically produced in samples poly-dispersed in diameter and chirality that cannot be easily sorted. Advance in nanotube separation using effective methods such as density gradient ultracentrifugation (DGU) [14] or aqueous two-phase extraction (ATPS) [15,16] promise to overcome this barrier. To stabilise individually dispersed SWNTs in aqueous systems, one can use polymers [17-19], proteins or DNA [20-23],

but these macromolecules are difficult to remove from the SWNTs. Surfactants came to be considered because they can be easily removed from the nanotubes. Numerous experimental studies are available regarding the stability of carbon nanotube dispersions in the presence of various surfactants [24-39]. For example, McDonald *et al.* [28] employed two-dimensional photoluminescence (PL) contour maps to characterise aqueous carbon nanotube samples stabilised by surfactants, and concluded that sodium dodecyl sulphate (SDS) is not as good a stabiliser as sodium cholate (SC) or sodium dodecylbenzene sulfonate (SDBS) for (9,4) SWNT at 40°C. Wang and collaborators [40] employed small angle neutron scattering (SANS) to characterise SWNT dispersions stabilised by Triton X-100 and SDBS. At low surfactant concentration, the SWNTs were found to easily aggregate because the surfactant is not sufficient to provide a large kinetic barrier to SWNT-SWNT aggregation. At high surfactant concentration, the presence of surfactant micelles induces SWNT-SWNT depletion attractions that lead to SWNT coalescence. Using ultraviolet-visible adsorption spectroscopy (UV/Vis), Di Crescenzo *et al.* [35] reported that Gemini surfactants with aromatic spacers are able to disperse SWNTs at higher surfactant/SWNT weight ratios than SDS, SDBS, or cetyltrimethylammonium bromide (CTAB).

Understanding why some surfactants behave better than others at particular conditions would allow the design of novel compounds to stabilise carbon nanotubes of desired diameter, and perhaps chirality. Computer simulations, coupled with experiments, have proven to be useful in this objective because they can yield a detailed atomic-level picture of the aggregates formed on nanotubes. Tummala and Striolo [41] conducted atomistic molecular dynamics (MD) studies to elucidate the mechanisms responsible for the stabilisation of aqueous SWNT dispersions. The result showed that SDS yields disordered aggregates on SWNTs, although in general, the coverage is uniform and the morphology of the aggregates depends on the nanotube diameter, in qualitative agreement with neutron scattering results [31]. As opposed to SDS, flavin mononucleotide (FMN) surfactants were found to yield a rather complete SWNT coverage [42]. Lin and Blankschtein [43] reported MD simulation results for the

structure of bile salt SC on SWNTs and found that the cholate ions wrap around the tubes with a small tendency to orient perpendicularly to the tube axis.

Building on this knowledge, in **Chapter 3**, MD simulations were performed to investigate the morphology of aqueous SDBS surfactants self-assembled on SWNTs. Simulations were carried out at room conditions for different surface coverages on (6,6), (12,12), and (20,20) SWNTs. Because commercial SDBS samples contain isomeric mixtures, the different self-assembled structures that could be obtained using isomerically pure surfactants were studied. A linear and a branched SDBS in which the benzenesulfonate group was attached to the fifth carbon atom in the tail were chosen. The results suggested that branched SDBS, as opposed to linear isomers, could specifically stabilise SWNTs of narrow diameter. Experimentally, SDBS, however, has not shown specificity [24,25,30,36,38,44]. As an effort to understand the discrepancy between simulated versus experimental results, in **Chapter 4**, a simulation study in which equimolar mixtures of linear and branched SDBS molecules self-assembled on different SWNTs was carried out. The results suggested that there is no strong effect due to nanotube diameter on the morphology of mixed SDBS aggregates, in agreement with experiments.

Previously, using DGU and fluorescence spectroscopy, Duque *et al.* [45] investigated SDS-stabilised SWNT dispersions. Among other interesting observations, Duque *et al.* reported that when aliquots of caesium (Cs^+) ions were added to aqueous SDS-SWNT dispersions, the correlations between SWNTs and water greatly reduced, suggesting changes in the surfactant adsorbed aggregate structure on the SWNTs. Significant reorganization of self-assembled SDS aggregates was also reported by Tummala and Striolo [46], who conducted MD simulations for aqueous SDS on graphite when Na^+ ions were substituted with Cs^+ ones. Motivated by these experimental and simulation results, in **Chapter 5**, MD simulations were employed to study the aggregate morphology of aqueous CsDS surfactants at contact with SWNTs. The results were compared to those for aqueous SDS surfactants on SWNTs [41]. The results suggested that surface aggregates with Cs^+ ions, compared to Na^+ , yield a more compact coverage of the (6,6) SWNTs.

For many years, researchers have investigated the adsorption and aggregation of surfactants on various substrates and environments. Adsorption depends on surface hydrophobicity [47-50], radius of curvature of the surfaces [51-54], surface features [55-59], surfactant molecular structure [60-62], presence and nature of counterions [63-65] and electrolytes [66-68], surfactants concentration [69-71], and system conditions such as temperature [61] and pH [72,73]. Many studies were focused on smooth and uniform surfaces despite the fact that natural solid surfaces exhibit physical and/or chemical heterogeneities. On heterogeneous surfaces, the adsorption characteristics of surfactants differ significantly from those obtained on the homogeneous ones in terms of adsorption capacity [56,59], morphology of adsorbed aggregates [57,58], and even shape of the adsorption isotherms [55,59]. For example, using the atomic force microscope (AFM), Schulz and Warr [74] provided evidence of hemi-spherical surfactant structures on quartz; these structures formed because of the rough surface on which adsorption took place. Schniepp *et al.* [57,58] documented experimentally the influence of Au surface roughness on SDS aggregation. Wu *et al.* [59] and Gutig *et al.* [75] measured adsorption isotherm using the quartz crystal microbalance with dissipation (QCM-D); the authors reported that the amount of adsorbed CTAB surfactant was influenced by surface roughness. Using SANS, Mütter *et al.* [76] found that curvature of cylindrical silica nanopores would affect the aggregate morphology of ethylene glycol (C₁₂E₅) surfactants.

In support of experiments, computational studies can assist in better understanding how surfactants adsorb on heterogeneous substrates. Sammalkorpi and co-workers [77] examined the surfactant aggregates formation on imperfect graphite using MD simulations, and demonstrated that point (i.e., vacancies) and line (i.e., surface steps) defects affected the stability and orientation of SDS aggregates. Tummala *et al.* [78] performed MD simulations to investigate SDS adsorption on graphene nano-sheets and nano-ribbons; they reported pronounced effects due to the edges of the nano-materials.

To gain new insights into the effect of surface heterogeneity on surfactant adsorption behaviour, coarse-grained dissipative particle dynamics (DPD) simulations were employed to investigate the adsorption and aggregation of model surfactants on patterned surfaces. The DPD method was chosen because of its capability to simulate

large systems for extended periods of time and to assess the amount of surfactants adsorbed on surfaces as a function of bulk surfactant concentration. The adsorption on individual hydrophobic stripes surrounded by regions that effectively repelled the surfactants was considered; the effect of stripe width was documented, and the synergistic effects observed when two narrow stripes are found near each other. The results are reported in **Chapter 6**. The adsorption of surfactants within the fully and partially hydrophobic trenches was also examined and the corresponding results are presented in **Chapter 7**.

Chapter 2 Simulation Model and Method

This chapter presents the theoretical basis of this thesis. Details of the molecular dynamics and dissipative particle dynamics simulations are briefly explained in Section 2.1 and 2.2, respectively.

2.1 Molecular dynamics

2.1.1 Equations of motion and potential energy

Molecular dynamics (MD) is a computational technique which is used widely to investigate the structure, dynamics and thermodynamics of molecular systems [79]. The basic idea behind MD method is to solve the equations of motion of a set of interacting atoms and use the resulting trajectories to calculate the microscopic and macroscopic properties. In MD simulation the time evolution of a set of interacting atoms is followed by integrating Newton's equations of motion:

$$\frac{d\vec{r}_i}{dt} = \vec{v}_i, m_i \frac{d^2\vec{r}_i}{dt^2} = \vec{F}_i \quad (2-1)$$

where \vec{r}_i , \vec{v}_i , m_i , and \vec{F}_i are the position, velocity, mass, and force of atom i , respectively.

To start the simulation it is necessary to specify initial positions and velocities to the atoms. The initial positions may be assigned randomly, placed on a simple cubic lattice, obtained from an experimental data, or taken from a theoretical model. The initial velocities typically are selected randomly from a Boltzmann distribution at the temperature of interest [80].

For the system of N interacting atoms, the force is obtained from the gradient of a potential energy function: $\vec{F}_i = -\nabla_{\vec{r}_i} U(\vec{r}_1, \vec{r}_2, \dots, \vec{r}_N)$. The potential $U(\vec{r}_1, \vec{r}_2, \dots, \vec{r}_N)$ is the sum of bonded (i.e., intramolecular forces) and non-bonded (i.e., van der Waals and electrostatics) interaction energies, and can be written as

$$\begin{aligned}
U(\vec{r}_1, \vec{r}_2, \dots, \vec{r}_N) & \quad (2-2) \\
&= \sum_{bonds} \frac{a_i}{2} (r_i - r_{i0})^2 + \sum_{angles} \frac{b_i}{2} (\theta_i - \theta_{i0})^2 \\
&+ \sum_{torsions} \frac{c_i}{2} [1 + \cos(n\omega_i - \gamma_i)] \\
&+ \sum_{atom\ pairs} 4\varepsilon_{ij} \left[\left(\frac{\sigma_{ij}}{r_{ij}} \right)^{12} - \left(\frac{\sigma_{ij}}{r_{ij}} \right)^6 \right] \\
&+ \sum_{atom\ pairs} \frac{q_i q_j}{4\pi \varepsilon_0 \varepsilon_r r_{ij}}
\end{aligned}$$

In Equation (2-2), the first term accounts for the bonded potential modelling a covalent bond in a molecular structure, where r_i and r_{i0} are the bond length and the equilibrium bond length, respectively. The second term describes the angle potential of the angle formed between two bonds sharing a common atom. The corresponding bond angle is indicated by θ_i , and θ_{i0} is its equilibrium value. a_i and b_i are the force constants for the bonded and angle potentials, respectively. The third term determines the torsion angle potential, which is used to constrain the rotation around the chemical bond of four consecutive bonded atoms. This term is expressed by periodic energy with a periodicity determined by n , and rotational energy barriers given by c_i . ω_i and γ_i are the current dihedral angle and the phase angle, respectively. The fourth term is the van der Waals (vdW) repulsive and attractive interatomic forces described by the Lennard-Jones (LJ) 12-6 potential. ε_{ij} is the minimum (well depth) of the potential, σ_{ij} is the collision diameter, and r_{ij} is the distance between atoms i and j . To calculate vdW interactions the Lorentz-Berthelot combination rules are applied, which are given by $\varepsilon_{ij} = \sqrt{\varepsilon_i \varepsilon_j}$ and $\sigma_{ij} = (\sigma_i + \sigma_j)/2$ [81]. ε_i , ε_j , σ_i , and σ_j are the well depths for the atoms i and j and the collision diameters for the atoms i and j , respectively. The fifth term is the electrostatic term, represented by the Coulombic potential. q_i and q_j are charges of the atoms i and j . ε_0 and ε_r are the dielectric permittivity of vacuum and the relative dielectric constant of a medium in which the atoms i and j are placed, respectively.

In this thesis, for MD simulations the carbon atoms within single-walled carbon nanotubes (SWNTs) were treated as rigid uncharged LJ spheres based on the model proposed by Cheng and Steele [82]. The CH_n groups in sodium dodecyl benzenesulfonate (SDBS), sodium dodecyl sulphate (SDS), and caesium dodecyl sulphate (CsDS) surfactants were modelled as united-atom LJ spheres [83-85]. The DREIDING force field [86] was used to describe the benzenesulfonate group in SDBS surfactants. The combinations of force field used for SDBS were tested and successfully applied in the previous study [87]. The sulphate groups in both CsDS and SDS surfactant molecules were modelled as proposed by Dominguez and Berkowitz [88]. Na^+ and Cs^+ ions were described following the models of Schweighofer *et al.* [89] and Smith and Dang [90], respectively. Water molecules were modelled using the simple point charge-extended (SPC/E) model [91].

2.1.2 Leap-frog algorithm

In MD simulations, the leap-frog algorithm was chosen for integrating the equations of motion [80,92]. The position and dynamic properties (velocities and accelerations) can be approximated as

$$\vec{r}_i(t + \Delta t) = \vec{r}_i(t) + \Delta t \vec{v}_i\left(t + \frac{1}{2}\Delta t\right) \quad (2-3)$$

$$\vec{v}_i\left(t + \frac{1}{2}\Delta t\right) = \vec{v}_i\left(t - \frac{1}{2}\Delta t\right) + \Delta t \vec{a}_i(t) \quad (2-4)$$

To implement the leap-frog algorithm the velocities $\vec{v}_i\left(t + \frac{1}{2}\Delta t\right)$ are first calculated from the velocities at time $t - \frac{1}{2}\Delta t$ and the accelerations at time t . The positions $\vec{r}_i(t + \Delta t)$ are then deduced from the velocities just calculated together with the positions at time t . The velocity at time t can be calculated from

$$\vec{v}_i(t) = \frac{1}{2} \left[\vec{v}_i \left(t + \frac{1}{2} \Delta t \right) + \vec{v}_i \left(t - \frac{1}{2} \Delta t \right) \right] \quad (2-5)$$

Accordingly, the velocities leap-frog over the positions to give their values at $t + \frac{1}{2} \Delta t$. The positions then leap over the velocities at time $t + \Delta t$. The integration time step Δt is normally specified by the user. Using too large time step can cause the simulation to become unstable as the energy increases rapidly with time while using too small time step requires a large amount of computational time. The optimum choice of the time step should be approximately a factor of ten smaller than the fastest time scale in the system. In this thesis, for all MD simulations the time step $\Delta t = 2$ fs was used to integrate the equations of motion.

2.1.3 Treatment of non-bonded interactions

The most time-consuming part in MD simulations is the force calculation, specifically to the vdW and electrostatic interactions that must be computed for each pair of interacting atoms. To save time and computational costs, the calculation can be approximated by using a cut-off distance. That is, the interactions between pairs of atoms separated by a distance greater than the given cut-off distance are neglected. This method is appropriate for the vdW forces, which quickly vanish at longer distance. Electrostatic interactions, however, decrease slowly with the distance. If they are computed using a simple truncation at the cut-off distance, significant errors can be introduced. Several approximation algorithms have been developed to handle this concern, and one technique is to split the electrostatic interactions into a short-range component and a long-range component. The short-range component can be calculated in real space, while the long-range one can be calculated using Fourier space. Fourier-based particle-mesh Ewald (PME) method was employed in all MD simulations presented herein.

2.1.4 Periodic boundary conditions

Periodic boundary conditions are commonly used in MD simulations to remove boundary effects caused by finite size. A schematic representation of periodic boundary

conditions is shown in **Figure 2-1**. When using periodic boundary conditions, a computational box is surrounded by periodic images of itself, and its atoms move in a way similar to their images. The atoms near the boundary of the simulation box interact with other atoms in their own box as well as in their periodic images. For each atom leaving the box, at the same time, one of its images enters through the opposite side. As a result, there are no physical boundaries. For all MD simulations presented in this thesis, periodic boundary conditions were applied in all the directions.

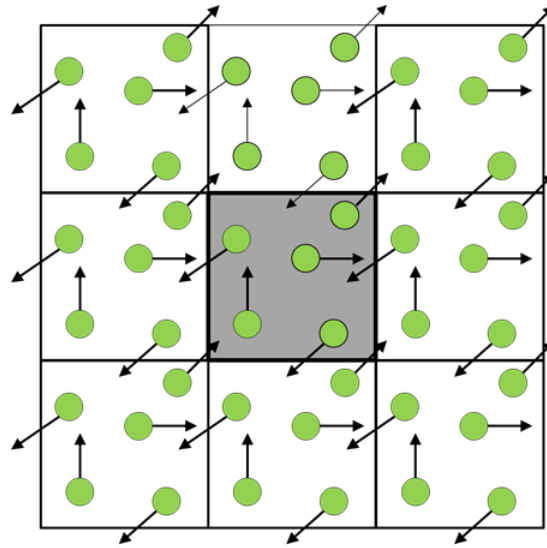


Figure 2-1: Two-dimensional example of periodic boundary conditions. The simulation box is highlighted at the centre, and is surrounded by periodic images of itself.

2.1.5 Thermostat

In this thesis, all MD simulations were carried out under the canonical ensemble, in which the number of atoms (N), the box volume (V), and the temperature (T) were kept constant. Using a thermostat is required to control the temperature of the system and avoid steady energy drifts caused by the accumulation of numerical errors. Nose-Hoover thermostat is efficient for relaxing the system to the target temperature [80] and was implemented in MD simulations. In the Nose-Hoover approach, the equations of motion are modified as $d^2\vec{r}_i/dt^2 = \{(\vec{F}_i/m_i) - [(p\xi/Q)(d\vec{r}_i/dt)]\}$, where ξ is a dynamic

quantity, which impedes or accelerates particles until the temperature T approaches the desired value T_0 . Q determines the relaxation of the dynamics of the friction and its own momentum $p\xi$ is given by $dp\xi/dt = (T - T_0)$.

2.2 Dissipative particle dynamics

Dissipative particle dynamics (DPD) is a mesoscopic simulation technique for simulating equilibrium and dynamical properties of fluids [93-96], introduced in 1992 by Hoogerbrugge and Koelman [97,98] and subsequently modified by Groot *et al.* [93,94,99]. Over the last two decades, the DPD method has been applied in a wide variety of systems including colloidal suspensions [100], surfactants in solution [101,102], polymer mixtures [103], flow in porous media [104], and many more. In DPD, several atoms are coarse-grained into one particle, known as “bead”. The beads interact with each other through pairwise additive forces that conserve momentum and provide correct hydrodynamic behaviour. Similar to MD, the time evolution of DPD beads is governed by Newton’s equations of motion, as given in Equation (2-1). The force \vec{F}_i exerted on bead i is comprised of a conservative force \vec{F}_{ij}^C , a dissipative force \vec{F}_{ij}^D , and a random force \vec{F}_{ij}^R [Equation (2-6)]. All forces act within a sphere of interaction r_c , which is the length scale of the system (DPD cut-off length).

$$\vec{F}_i = \sum_{j \neq i} (\vec{F}_{ij}^C + \vec{F}_{ij}^D + \vec{F}_{ij}^R) \quad (2-6)$$

2.2.1 Soft and repulsive potential

The conservative force \vec{F}_{ij}^C is given by

$$\vec{F}_{ij}^C = \begin{cases} a_{ij}(1 - r_{ij}/r_c)\hat{r}_{ij}, & r_{ij} < r_c \\ 0, & r_{ij} \geq r_c \end{cases} \quad (2-7)$$

where a_{ij} represents the strength of the repulsive interaction between beads i and j , $\vec{r}_{ij} = \vec{r}_j - \vec{r}_i$ (\vec{r}_i and \vec{r}_j are positions vectors of beads i and j), $r_{ij} = |\vec{r}_{ij}|$, and $\hat{r}_{ij} = \vec{r}_{ij}/|\vec{r}_{ij}|$. It is worth noting that the conservative force is finite even when $\vec{r}_j = 0$ (i.e., two DPD beads completely overlap with each other), indicating that DPD is a soft potential. The feature of soft potential allows the use of much larger time scale in DPD, compared to MD method where the potential is based on a theoretical-molecular model of the physical system [105]. **Figure 2-2** shows a plot of conservative force against distance r_{ij} . The conservative force is modelled as a linear function of the distance between two beads and is zero at the cut-off length r_c .

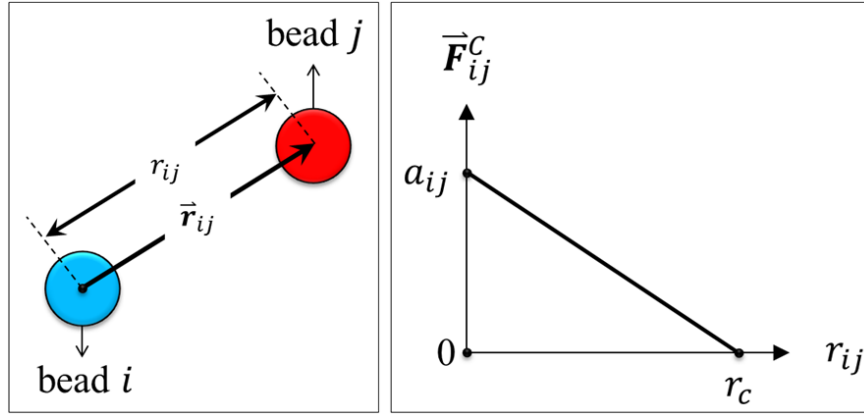


Figure 2-2: Left: definition of distance r_{ij} . Right: a plot of the conservative force \vec{F}_{ij}^C as a function of distance r_{ij} . a_{ij} is constant for the maximum repulsion between the interacting beads. r_c is the cut-off length.

2.2.2 Built-in Langevin thermostat

The dissipative force \vec{F}_{ij}^D describes friction and energy dissipation as bead i moves past bead j , and is given by

$$\vec{F}_{ij}^D = -\gamma\omega^D(r_{ij})(\vec{r}_{ij} \cdot \vec{v}_{ij})\hat{r}_{ij} \quad (2-8)$$

where γ is the friction coefficient, $\omega^D(r_{ij})$ is the dissipative weight function, and $\vec{v}_{ij} = \vec{v}_j - \vec{v}_i$.

The random force \vec{F}_{ij}^R compensates for the loss of kinetic energy from dissipation and is given by

$$\vec{F}_{ij}^R = \sigma \omega^R(r_{ij}) \theta_{ij} \hat{r}_{ij} \quad (2-9)$$

where σ is the strength of the random force, $\omega^R(r_{ij})$ is the random weight function, and θ_{ij} is a random variable with uniform distribution and unit variance. The common relationship between dissipative and random weight functions is $\omega^D(r_{ij}) = [\omega^R(r_{ij})]^2$. The friction coefficient and the strength of random force are linked by the relation $\sigma^2 = 2\gamma k_B T$ that allows maintaining a constant temperature in the course of simulation. T is the absolute temperature of the system and k_B is the Boltzmann constant. The value of $k_B T$ was set as 1 in all DPD simulations.

2.2.3 Spring force

In DPD simulations the surfactant was modelled by a chain of one hydrophilic head and two hydrophobic tail beads. To describe the constraint between the bonded consecutive beads within the surfactant molecule, a spring force \vec{F}_{ij}^S is introduced into the simulations, and is given by

$$\vec{F}_{ij}^S = -k_S \left(1 - \frac{r_{ij}}{r_0}\right) \hat{r}_{ij} \quad (2-10)$$

where k_S is the spring constant and r_0 is the equilibrium bond length. The total force acting on the DPD beads is accordingly the combination of the spring force and the forces given in Equation (2-6)

$$\vec{F}_i = \sum_{j \neq i} (\vec{F}_{ij}^C + \vec{F}_{ij}^D + \vec{F}_{ij}^R + \vec{F}_{ij}^S) \quad (2-11)$$

2.2.4 Modified velocity Verlet algorithm

The dissipative force is dependent on the bead velocity, and the equations of motions are solved by a modified version of the velocity Verlet algorithm [93], which is described as

$$\vec{r}_i(t + \Delta t) = \vec{r}_i(t) + \Delta t \vec{v}_i(t) + \frac{1}{2} (\Delta t)^2 \vec{f}_i(t) \quad (2-12)$$

$$\vec{v}_i'(t + \Delta t) = \vec{v}_i(t) + \lambda \Delta t \vec{f}_i(t) \quad (2-13)$$

$$\vec{f}_i(t + \Delta t) = \vec{f}_i[\vec{r}_i(t + \Delta t), \vec{v}_i'(t + \Delta t)] \quad (2-14)$$

$$\vec{v}_i(t + \Delta t) = \vec{v}_i(t) + \frac{1}{2} \Delta t [\vec{f}_i(t) + \vec{f}_i(t + \Delta t)] \quad (2-15)$$

where $\vec{r}_i(t)$ and $\vec{f}_i(t)$ are the position and force, respectively, for bead i at time t . $\vec{v}_i'(t)$ and $\vec{v}_i(t)$ are the predicted and corrected velocities, respectively, at time t . λ is an adjustable parameter in the range 0-1, with 0.5 being found as preferable. Δt is the integration time step.

2.2.5 Units of length and time

In DPD method, it is convenient to use reduced units. The unit of length is defined by the cut-off length r_c ; the unit of mass is defined by masses of beads; and the unit of energy is defined by $k_B T$. Each water bead represents five water molecules (i.e., the degree of coarse graining $N_m = 5$), and has volume $V_b = \sim 150 \text{ \AA}^3$ [106]. The reduced density of one DPD bead (the average number of beads in $1 r_c^3$) was set to $\rho = 5$. Accordingly, the DPD cut-off length $r_c = \sqrt[3]{5 \times 150} = 9.0856 \text{ \AA}$. The DPD time scale can be evaluated by matching the self-diffusion constant of water. As proposed by Groot

and Rabone [94], the time constant of the simulation is calculated as $\tau = \frac{(N_m D_{sim} r_c^2)}{D_{water}}$, where τ is the DPD time constant, D_{sim} is the simulated water self-diffusion coefficient, and D_{water} is the experimental water self-diffusion coefficient. When $a_{ii} = 15 k_B T / r_c$, $D_{sim} = 3.0615 r_c^2 / \tau$. For $D_{water} = 2.43 \times 10^{-3} \text{ cm}^2/\text{s}$ [107], $\tau = 5.2 \text{ ps}$.

Chapter 3 Role of Surfactant Molecular Structure on Self Assembly: Aqueous SDBS on Carbon Nanotubes

The material presented in this chapter was published in 2011, volume 115, pages 17286-17296 of The Journal of Physical Chemistry C.

3.1 Chapter overview

Stabilising single-walled carbon nanotubes (SWNTs) monodispersed in diameter and chirality in aqueous media remains elusive. Surfactants have proven useful in deploying ultracentrifugation techniques for separating carbon nanotubes, but the molecular mechanism responsible for the effectiveness for such technique remains not fully understood. Based on recent molecular dynamics (MD) results, it appears that the morphology of self-assembled surfactant aggregates on carbon nanotubes strongly affects the effective potential of mean force between pairs of interacting carbon nanotubes. In this chapter, the effect of surfactant molecular structure on the properties of aqueous surfactant self-assembled aggregates was investigated by employing all-atom MD simulations. To quantify how the surfactant molecular structure affects self-assembly, sodium dodecyl benzenesulfonate (SDBS) surfactants with the benzenesulfonate group located either on the fifth or on the twelfth carbon atom along the dodecyl tail were considered. All simulations were conducted at room conditions for different surface coverages on (6,6), (12,12), and (20,20) SWNTs. The results suggest that the surfactant molecular structure strongly affects the packing of surfactants on the nanotubes, therefore modulating effective nanotube-nanotube interactions. In qualitative agreement with experiments, no strong effects due to nanotube diameter were observed.

3.2 Introduction

The unique structure and superior properties of single-walled carbon nanotubes (SWNTs) [10] make them promising materials for a number of applications, including probes, bio-sensors, catalyst supports, hydrogen storages, gas separation, composites and multifunctional materials, and so on [108]. Unfortunately, because SWNTs tend to

agglomerate into bundles when dispersed in either water or organic solvents due to strong van der Waals interactions [109], the realization of their potential has been limited.

One possibility for preventing the SWNT agglomeration is to disperse SWNTs using superacids as solvent [110-112]. Parra-Vasquez *et al.* [111] demonstrated that the protonation of SWNTs in chlorosulfonic acid enables their dispersion at high concentration (5000 ppm by mass) without damaging the SWNTs. SWNTs at concentrations up to 3.5 mg/mL can be dispersed in cyclohexyl pyrrolidone [113]. Modification of the SWNT surfaces, covalently and noncovalently, has been an alternative strategy to stabilise SWNT dispersions. Covalent modification usually causes the SWNTs to lose their exceptional electronic properties because of the disruption of the π system [114]. Dispersing SWNTs by noncovalent functionalization is particularly attractive, as it preserves the intrinsic properties of SWNTs [115]. In this latter approach, dispersing agents such as surfactants [24-31,38,116], polymers [17,18], or biomolecules [20-22] adsorb onto the nanotubes via noncovalent interactions.

Surfactants are extensively used to disperse SWNTs in water. Although they are expected to adsorb on the SWNT surfaces with their hydrophobic tails, while the hydrophilic heads orient towards the solution [40], an ongoing debate attempts to clarify the structure of self-assembled surfactant aggregates on nanotubes. A large number of amphiphilic molecules, including sodium dodecyl sulphate (SDS) [24,25,28,30,31,38], sodium dodecyl benzenesulfonate (SDBS) [24-27,29,30,38,116], cetyltrimethylammonium bromide (CTAB) [30,38], octylphenol ethoxylate (Triton X-100) [30,38], sodium cholate (SC) [24,25], and sodium deoxycholate (DOC) [24,25] have been shown to stabilise SWNT dispersions, with varying effectiveness. Haggemueller *et al.* [25] used optical absorption and fluorescence spectroscopy to evaluate the amount of individual SWNTs suspended by various surfactants and reported that bile salt DOC provides better suspension quality compared to other surfactants.

Among various surfactants, SDBS is commonly used to stabilise aqueous SWNT dispersions without showing strong dependence on the SWNT diameter [29]. It was reported that SDBS can disperse up to 20 mg/mL of individual SWNTs [26]. The benzene ring in the SDBS molecule is believed to provide superior dispersive ability due to π - π interactions with the SWNTs, despite being located near the hydrophilic head of the molecule [26,30,38]. Matarredona *et al.* [27] analyzing their experimental data suggested that hydrophobic interactions dictate for the most part the agglomeration of SDBS on SWNTs.

The many experimental studies available for SDBS-aided SWNT dispersion in water are supported by very few, if any, molecular simulation studies. Tummala and Striolo [41] used extensive all-atom MD simulations and observed that the morphology of SDS surfactant aggregates strongly depends on the nanotube diameter as well as on the surface coverage. Along with Xu *et al.* [117], they attempted to clarify how the aggregate SDS structures on SWNTs determines effective SWNT-SWNT interactions. Aqueous dispersions of SWNTs stabilised using the bile salt surfactant SC were investigated via MD simulations by Lin and Blankschtein [43]. The results showed that the cholate ions wrap around the tubes with a small tendency to orient perpendicularly to the tube axis. Tummala *et al.* [42] used MD simulations to describe the self-assembly of flavin mononucleotide (FMN) adsorbed on SWNTs. They found that the aggregation morphology of aqueous FMN on SWNTs depends on nanotube diameter.

Despite their large technological importance, alkyl benzenesulfonates have rarely been considered in MD simulations. Jang *et al.* [87] simulated sodium hexadecane benzenesulfonate at the water/decane interface. He *et al.* [118] simulated monolayers of a series of linear and branched alkyl benzenesulfonates at the water/air interface and observed that the length of alkyl chain and the position of attachment of the benzene ring on the alkyl chain affect the aggregate morphology and the surface tension of alkyl benzenesulfonates at water/air interface. These results are important because they point at the effect of surfactant morphology on practical quantities, specifically the surface tension.

In this chapter, the adsorption and self-assembly of SDBS surfactants on (6,6), (12,12) and (20,20) SWNTs are investigated via all-atom MD simulations. The effects of SDBS surface coverage and molecular architecture on the aggregate morphology are discussed. Because of computational limitations, the study is limited to relatively dilute systems.

3.3 Methodology

3.3.1 System composition

Extensive all-atom MD simulations of a four-component system, composed of water, SDBS, sodium (Na^+) ions, and SWNTs, were utilised to study the self-assembly of SDBS on the SWNT surface. Three SWNTs [(6,6), (12,12), and (20,20)], with diameters of 0.814, 1.628, and 2.713 nm, respectively, were considered.

To investigate the effect of surface coverage on the surfactant aggregate structure at the water-SWNT interface, two surface coverages were examined including 1.0 SDBS molecules/ nm^2 (1.0 $\text{nm}^2/\text{headgroup}$) and 2.8 SDBS molecules/ nm^2 (0.357 $\text{nm}^2/\text{headgroup}$). Both surface coverages are comparable to those known for SDS [117]. It should be noted that the surface coverages used in this study are much lower than the larger ones, estimated from experimental adsorption isotherms (e.g., the packing density of the sulfonate headgroup was found to be 22.5 molecules/ nm^2 by assuming the nanotube surface area of 2000 m^2/g [27]). On the basis of results, the surface density of 22.5 molecules/ nm^2 appears a rather high estimate. In fact, as detailed below, even at the surface coverage of 2.8 SDBS molecules/ nm^2 , it is found that SDBS agglomerate into micellar aggregates away from the SWNT surface. These results suggest that employing surface coverages higher than 2.8 molecules/ nm^2 would result in the formation of micelle in the aqueous solution. Because of computational limitations, two relatively low surface coverages (defined high and low surface densities below for simplicity) are considered. Other computational techniques, including dissipative particle dynamics (DPD) [119,120] should be employed to study larger surfactant densities. Such techniques could also be implemented to study the effect of surfactant concentration on

the amount adsorbed onto the carbon nanotubes and on the surfactant propensity at forming micelles.

Because SDBS surfactants are found with different molecular architectures [1], this surfactant is ideal for studying the effect of surfactant molecular structure on its efficacy in stabilising dispersions containing SWNTs. Thus, it is of interest to quantify the SDBS packing on SWNTs as a function of the SDBS molecular structure. Two different molecular architectures of SDBS were considered. In the first, benzenesulfonate was attached to the twelfth carbon atom in the dodecane backbone (linear SDBS). In the second, the benzenesulfonate was attached to the fifth carbon atom in the dodecyl chain (branched SDBS). These structures are reported in **Figure 3-1**.

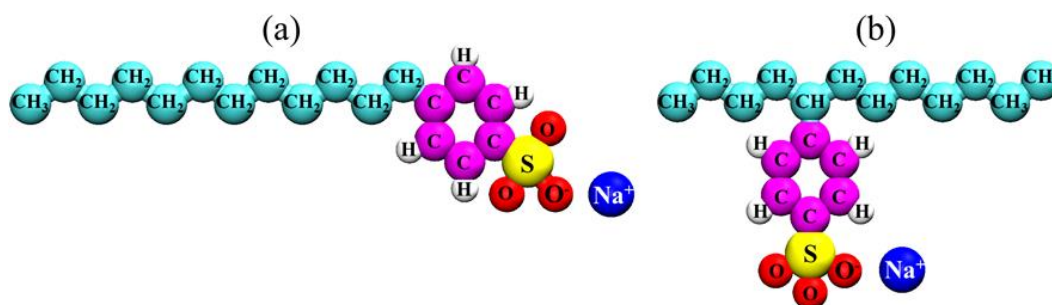


Figure 3-1: Chemical structures of (a) linear and (b) branched SDBS surfactants. Na⁺ ions are considered completely dissociated.

3.3.2 Force fields

The carbon atoms within SWNTs were treated as Lennard-Jones (LJ) spheres and maintained fixed throughout the course of the simulations. The LJ parameters used to describe carbon-carbon interactions were those of Cheng and Steele [82]. Water molecules were modelled using the simple point charge-extended (SPC/E) model [91]. One molecule of SDBS surfactant is composed of one hydrophobic tail of 12 carbon atoms (1 CH₃ and 11 CH₂ groups for linear SDBS; 2 CH₃, 9 CH₂, and 1 CH for branched SDBS) and one hydrophilic head composed of one benzenesulfonate group. The CH_n groups in SDBS were modelled as united-atom LJ spheres [83-85]. The

benzenesulfonate was described implementing the explicit all-atom model using the DREIDING force field [86]. The force field parameters used to calculate the intramolecular interactions were borrowed from Jang *et al.* [87]. It should be pointed out that DREIDING is a general-purpose force field. It has been found to overestimate ring-stacking and the adsorption energy [86] for aromatics on graphite [121]. All force field parameters used to compute the intra- and intermolecular interactions are summarised in Appendix A.

3.3.3 Algorithms

For all simulated systems, one SWNT was maintained at the centre of the simulation box of dimensions $10 \times 10 \times 7.44 \text{ nm}^3$. The cylindrical axis of the SWNT was aligned along the Z direction of the simulation box. The nanotube was not allowed to move during the simulations. To construct the initial configuration, the desired number of surfactants was placed around the SWNT with their tails perpendicular to the nanotube axis. The number of water molecules in the box was adjusted to reproduce bulk liquid water density at ambient conditions. Periodic boundary conditions were applied in X , Y , and Z dimensions. Before initiating the MD simulations, an energy minimization was performed to relax the system. It is known that the results of MD simulations, particularly those for systems with slow relaxation times, can depend on their initial configurations. To minimise these effects, all systems were simulated at 1000 K for 1 ns and then instantaneously brought to 300 K.

The simulations were carried out using the GROMACS package, version 4.0.7 [122]. The equations of motion were integrated with a time step of 0.002 ps using the leap-frog algorithm [79]. The simulations were conducted within the canonical ensemble, in which the number of particles (N), the box volume (V), and the temperature (T) were kept constant. All simulations were carried out at 300 K using the Nose-Hoover thermostat with a relaxation time constant of 0.1 ps [79,123]. The long range electrostatic interactions were handled with the Particle Mesh Ewald method with a precision 10^{-4} [124]. The van der Waals interactions were treated with cut-off at 9 Å, which falls within the typical range of cut-off values used in other publications [42,43,117]. The

trajectories and velocities were saved every 1000 steps (2 ps) for subsequent analysis. At low surface coverage, each system was equilibrated for 250 ns. In the case of high surface coverage, the systems were equilibrated for 400 ns [53 linear SDBS on (6,6) SWNT; 106 branched SDBS on (12,12) SWNT; 178 branched SDBS on (20,20) SWNT] and 500 ns [106 linear SDBS on (12,12) SWNT; 178 linear SDBS on (20,20) SWNT; 53 branched SDBS on (6,6) SWNT]. The last 50 and 100 ns were used for data analysis at low and high surface coverages, respectively. All simulated systems were considered equilibrated when the results did not change during the last 100 ns of simulation. The simulated systems, including the SWNTs, the total numbers of SDBS and water molecules, surfactant coverages, and the simulation times are reported in Appendix A.

3.4 Results and discussion

3.4.1 Self-assembly of linear SDBS surfactants on SWNTs

Representative simulation snapshots of linear SDBS surfactants adsorbed on (6,6), (12,12), and (20,20) SWNTs are illustrated in **Figure 3-2** and **Figure 3-3**. In **Figure 3-2**, the equilibrium configurations at low surface coverage on the three SWNTs are presented. The snapshots show that linear SDBS molecules wrap around the SWNTs. The tail segments and most benzene rings are positioned closely to the SWNT surface, while the sulfonate headgroups are exposed to water. However, it should be noted that, unexpectedly, some headgroups can be found near the nanotube surface.

At high surface coverage, **Figure 3-3**, it is noticed that the tail segments adsorb in a compact manner around the SWNT surfaces. Unexpectedly, on the basis of the argument according to which π - π interactions dictate the packing of SDBS on nanotubes, most benzene rings are found further from the nanotubes, although close to the layer of tail segments. The sulfonate headgroups mainly extend toward the aqueous phase. On (20,20) SWNT, it is found formation of micelles adsorbed on the tubes. Na^+ counterions (blue spheres) can be observed in between the linear SDBS headgroups within the micelle and the linear SDBS headgroups on the (20,20) SWNT, suggesting that strong counterion condensation lead to the formation of the aggregates, shown in **Figure 3-3**.

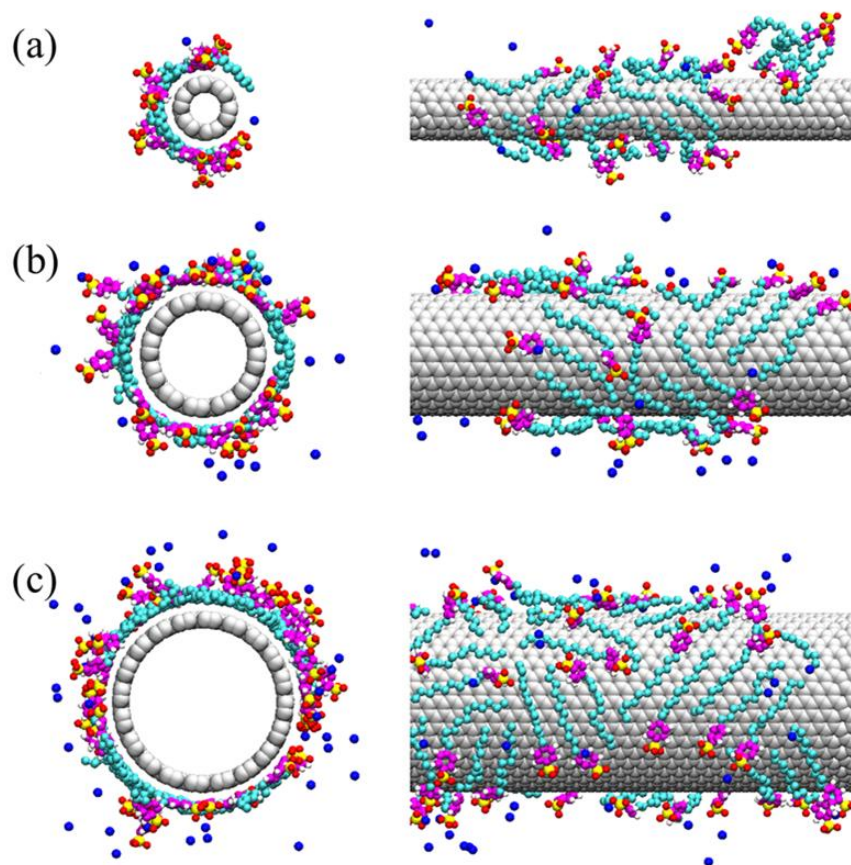


Figure 3-2: Front (left) and side (right) views of representative simulation snapshots of linear SDBS surfactants adsorbed on (a) (6,6), (b) (12,12), and (c) (20,20) SWNTs at low surface coverage. Water molecules are not shown for clarity. Colour code: cyan for CH_n -groups; purple for carbon atoms in benzene rings; white for hydrogen atoms in benzene rings; red for oxygen atoms; yellow for sulphur atoms; blue for Na^+ counterions; grey for carbon atoms in SWNTs.

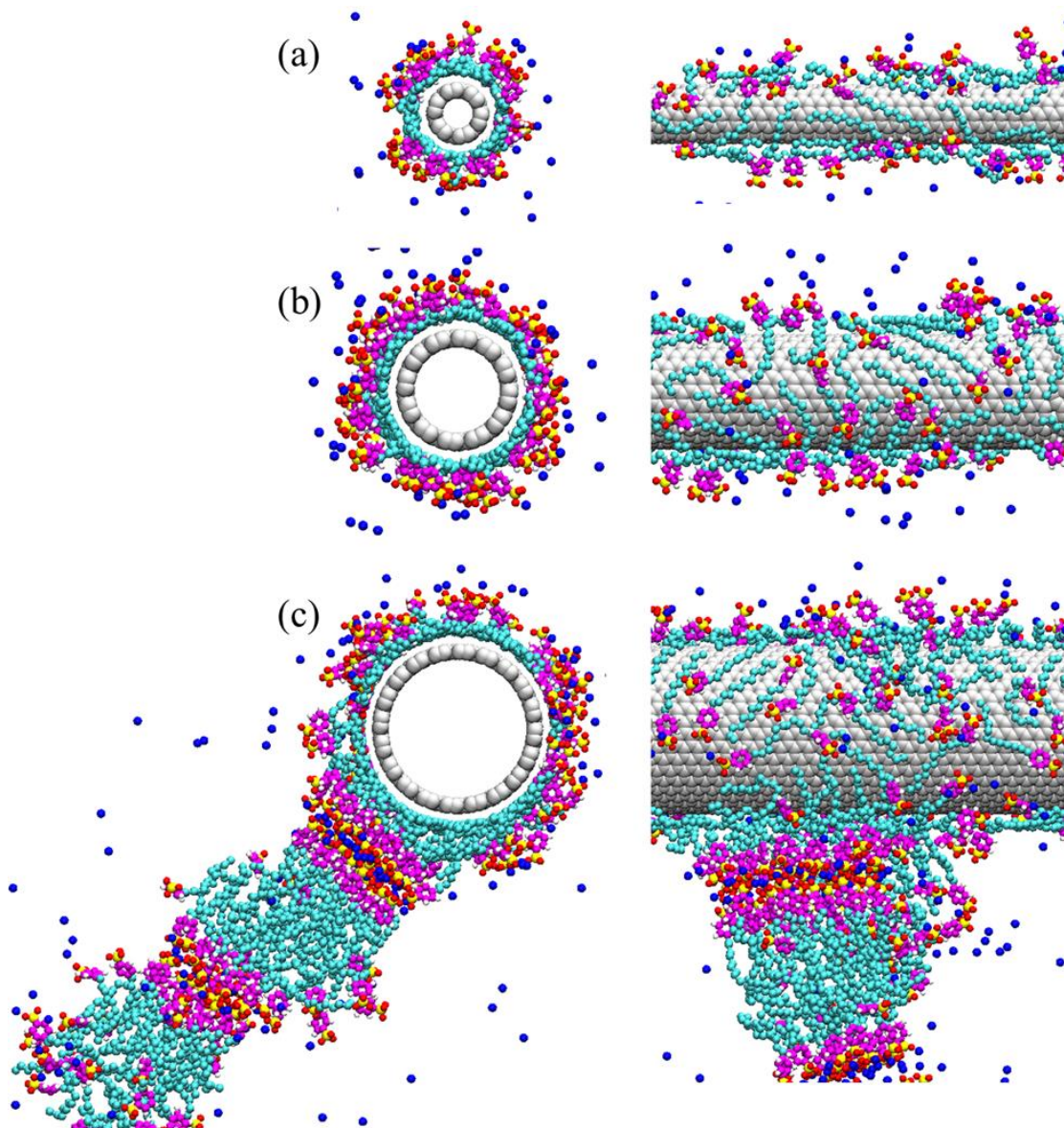


Figure 3-3: Same as **Figure 3-2** but for high surface coverage.

It should be pointed out that small SDBS micelles, as well as isolated SDBS monomers, are found within the aqueous phase for all systems shown in **Figure 3-2** and **Figure 3-3**. However, only on (20,20) SWNT the multi-layered structure shown in the bottom panel of **Figure 3-3** is observed. It is possible that as the surfactant concentrations within the simulated systems increase, exotic structures such as that observed on (20,20) SWNT form also on the other nanotubes considered, leading to surface coverages comparable to

those estimated experimentally by Matarredona *et al.* [27]. Coarse-grain methods such as DPD should be implemented to study such dense systems [119,120]. The results presented here can be used to quantify the surfactant structure at relatively low surface coverage, focusing on those SDBS molecules that, after an extensive equilibration time, remain at contact with the nanotubes.

Focusing on the adsorbed SDBS surfactants, a common feature shared by **Figure 3-2** and **Figure 3-3** is that each SWNT is covered by a monolayer of linear SDBS molecules. The tail segments and the benzene rings remain in contact with the nanotube surface, while the headgroups extend to the aqueous phase. Hydrophobic interactions between the tail segments and the SWNTs are responsible for these results. A great number of Na⁺ counterions accumulate near the sulfonate groups due to the strong electrostatic attraction between the oppositely charged groups. In most cases the Na⁺ ions maintain their hydration water, unless they are found sandwiched in between surfactant layers (**Figure 3-3**, bottom panel), in which case that hydration water molecules are lost. The multi-layered aggregates formed on (20,20) SWNTs were expected. Detailed analysis shows that when the multilayers are compact (e.g., closer to the nanotubes), water molecules are excluded from the region in between the neighboring surfactant heads and Na⁺ counterions. This strong evidence for counterion condensation was observed in simulations for other surfactants in the presence of Na⁺, despite the known tendency of Na⁺ ions to maintain a dense layer of hydration water molecules [41,42,46,54]. Detailed experimental evidence is insufficient to assess whether structures such as the one in **Figure 3-3**, bottom panel, are real. However, such structures would be consistent with a large amount of SDBS adsorbed per unit surface area, consistent with experimental observations of Matarredona *et al.* [27].

In order to quantify the effective surface coverage of linear SDBS on the three SWNTs, the time-average number of linear SDBS adsorbed on the SWNT was computed by integrating the number density profiles of the linear SDBS molecules around the SWNT (density results are shown later) up to a cut-off distance of 12 Å. The linear SDBS molecules located within the cut-off distance from the SWNT surface are considered to be adsorbed on the nanotube, and the linear SDBS molecules that are beyond the cut-off

distance are considered as dispersed in the aqueous media (these can be found as monomers, and, sometimes, as small aggregates). The average number of SDBS not adsorbed was calculated at the difference between the total number of SDBS molecules present in the simulation box and the average number of SDBS molecules adsorbed on the nanotube. Detailed results of population analysis for linear SDBS at both low and high surface coverages are summarised in **Table 3-1**.

Table 3-1: Population analysis results for linear SDBS surfactants adsorbed on SWNTs

SWNT	No. of SDBS simulated [molecules]	Nominal SDBS surface coverage [molecules per nm ²]	No. of SDBS adsorbed [non-adsorbed] [molecules]	Effective SDBS surface coverage [molecules per nm ²]
(6,6)	19	1.0	14 [5]	0.7
(12,12)	38	1.0	27 [11]	0.7
(20,20)	63	1.0	54 [9]	0.9
(6,6)	53	2.8	37 [16]	2.0
(12,12)	106	2.8	56 [50]	1.5
(20,20)	178	2.8	90 [88]	1.4

Despite careful preparation of simulation boxes, it should be noted from **Table 3-1** that the surface coverage at both low and high coverages changes from system to system. At high surface coverage, a large number of linear SDBS molecules do not adsorb, particularly on (12,12) and (20,20) SWNTs. As a consequence, the effective linear SDBS surface coverages considered in this study are 1.5 and 1.4 molecules/nm², respectively. As the nominal surface coverage increases, the number of surfactants present within each simulation box increases, and the probability of forming micelles aggregates not adsorbed on the nanotubes also increases. This leads to effective surface coverages that are much lower than nominal ones.

Focusing on the adsorbed SDBS molecules on the SWNTs, the positions of each SDBS fraction (tail, benzene ring, and headgroup) and the surrounding water molecules can be quantified by calculating density distributions away from the SWNT surface. The position of each surfactant tail is identified by that of both CH₂ or CH₃ groups in the

dodecane backbone. The positions of benzene ring, headgroup, and water are defined as the centre of mass of the benzene ring, the sulfonate group, and water molecule, respectively. The density distributions of tail segments, benzene rings, sulfonate headgroups, Na⁺ counterions, and water molecules on (6,6), (12,12), and (20,20) SWNTs are shown in **Figure 3-4**.

In **Figure 3-4** (left panels), the density distributions obtained on the three SWNTs at low surface coverage are reported. The density profile of the tail segments on the three SWNTs displays a strong peak at 3.5 Å (**Figure 3-4a**), indicating that the tail segments adsorb on the SWNT surface. Most benzene rings are located near the nanotube surfaces (**Figure 3-4b**). A small fraction of the benzene rings extends to water, as can be noticed from the shoulder found at ~ 6 Å. Since benzene groups lie on the SWNT surfaces, some of the sulfonate headgroups are located near the tube surfaces, as demonstrated by the first peak at 4 Å (**Figure 3-4c**). This result was unexpected because the headgroups are hydrophilic. The peak at 5.5 Å and the shoulder at 7.5 Å show that some headgroups are positioned away from the substrate towards the aqueous phase. Na⁺ counterions accumulate near the charged sulfonate groups with the largest peak at 6 Å (**Figure 3-4d**), evidence of counterion condensation [46]. A pronounced peak in the water density profiles is observed at 3.5 Å for three SWNTs (**Figure 3-4e**), corresponding to a large number of water molecules accumulated near the SWNT surface. At longer distances ($r > 12$ Å), the density of interfacial water approaches bulk values. This suggests that the presence of the surfactants affects the density of interfacial water only at short distance.

As shown in **Figure 3-2** and **Figure 3-3**, the linear SDBS aggregate morphology is affected by surface coverage. Comparing the density profiles just discussed to those obtained at high surface coverage (right panels in **Figure 3-4**) allows quantifying such quantitative observations. Even at high surface coverage the tail segments are found predominantly adsorbed on the SWNT, manifesting a strong peak at 4 Å (**Figure 3-4f**). At high surface coverage, the benzene rings are found both close to the nanotube surfaces and a little further, just next to the layer of tail segments (**Figure 3-4g**). The

density profile of benzene rings becomes wider with a thickness of ~ 5 Å. At high surface coverage, the results show that a majority of headgroups are predominantly found away from the SWNT surface, yielding the largest density peak at 8.5 Å (**Figure 3-4h**). However, a few headgroups remain near the substrate, with small density peaks at 4 and 5.5 Å, even at high surface coverage. In the case of (20,20) SWNT, the density profile of headgroups is quite different from that observed for (6,6) and (12,12) SWNTs. This is a consequence of the formation of the micelles at contact with the adsorbed SDBS surfactants shown in the bottom panel of **Figure 3-3**. Because of the micelle, a large number of headgroups can be found away from the SWNT surfaces, and hence the shoulder at 12 and 15 Å in the density profile is observed. At high surface coverage, on all nanotubes the Na^+ counterions associate closely to the sulfonate headgroups (**Figure 3-4i**). The accumulation of the positively charged counterions near the negatively charged sulfonate groups is due to counterion-condensation phenomena. The counterion condensation shields the electrostatic repulsion between the charged sulfonate groups and effectively brings them close to each other, similarly to what has been observed in previous studies [41-43,54]. At high surface coverage, the intensity of the peak in the water density profiles at 3.5 Å decreases because of the compact packing of the adsorbed linear SDBS aggregates (**Figure 3-4j**).

The aggregate morphology of linear SDBS surfactants assemblies on SWNTs depends not only upon the surface coverage but also, to some extent, upon the SWNT diameter. Visual inspection of simulation snapshots suggests that on (6,6) SWNT (**Figure 3-2a**), the tail segments appear to lie parallel to the SWNT axis. As the SWNT diameter increases, the tail segments orient themselves both parallel and perpendicular to the nanotube axis, especially on (20,20) SWNT (**Figure 3-2c**). Similarly results were observed for SDS surfactants and attributed to the stiffness of the surfactant tails [41].

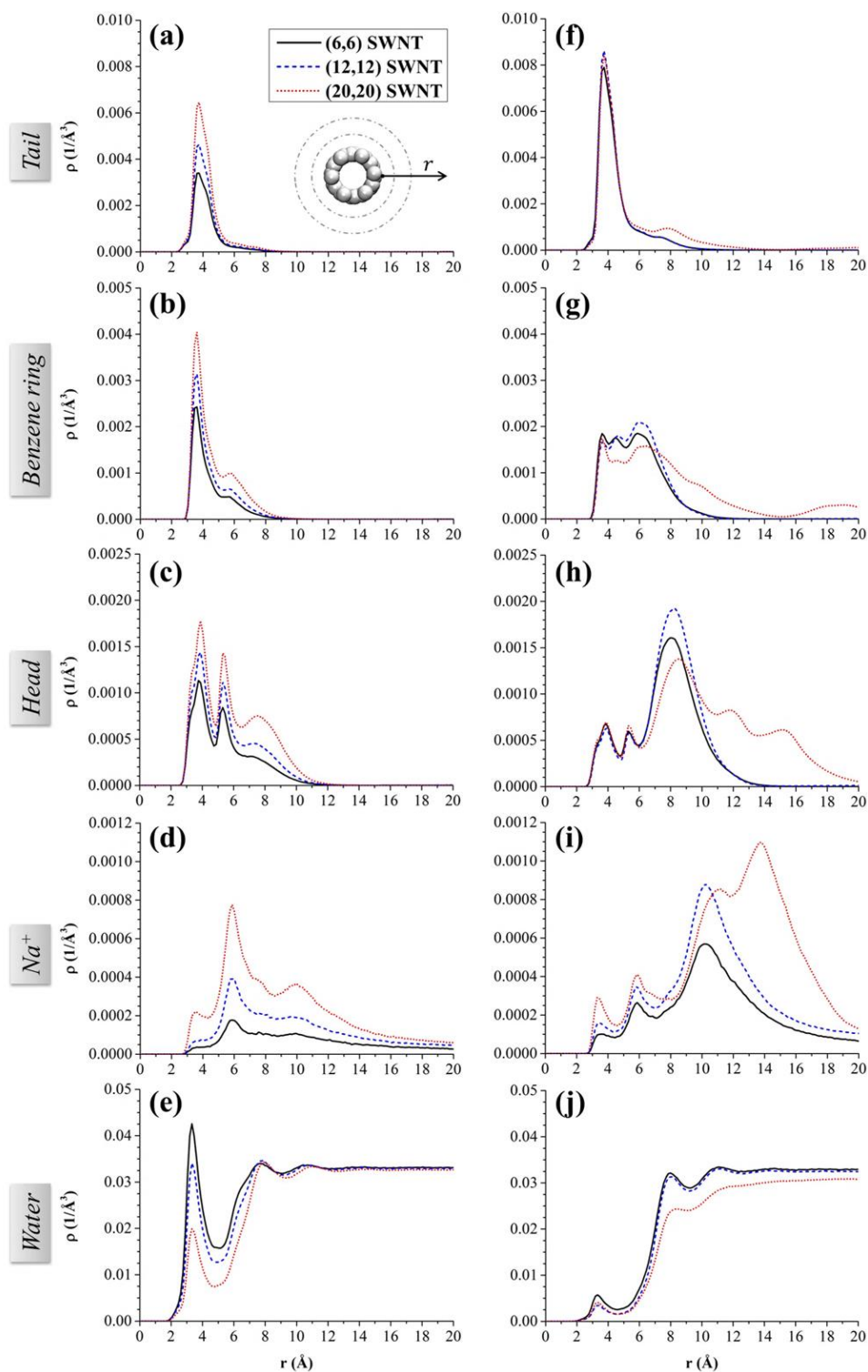


Figure 3-4: Density distributions of (a, f) tail segments, (b, g) benzene rings, (c, h) headgroups, (d, i) Na⁺ counterions, and (e, j) water molecules relative to the SWNT (“ r ” is measured radially from the nanotube surface). The results are obtained for linear SDBS on the three SWNTs at low (left) and high (right) surface coverages. The solid, dashed, and dotted lines represent (6,6), (12,12), and (20,20) SWNTs, respectively.

To quantify the orientation of linear SDBS molecules adsorbed on the three SWNTs, the angle between the vector identified by the surfactant tail and the SWNT axis, and that between the vector identified by the benzenesulfonate and the SWNT axis was calculated. Only linear SDBS molecules located up to a cut-off distance of 9 Å (tail) and 12 Å (sulfonate) from the SWNT surface were considered for these calculations. A schematic illustrating the two vectors defined by one SDBS molecule is shown in **Figure 3-5**. Note that when the angle between either the surfactant tail or the benzenesulfonate and the SWNT axis is 0° or 180° , the correspondent vector is parallel to the nanotube axis. When this angle is 90° , the vector is perpendicular to the nanotube axis.

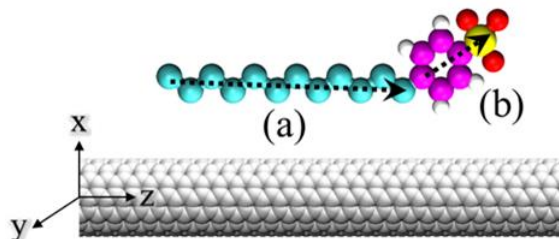


Figure 3-5: The vectors defined by (a) tail segments and (b) benzenesulfonates used to calculate the probability distribution of the orientation angle between linear SDBS molecule and the SWNT axis (parallel to the Z-axis of the simulation box).

The orientation probability distribution for linear SDBS molecules on (6,6), (12,12), and (20,20) SWNTs at low surface coverage is illustrated in **Figure 3-6** (left panels). In **Figure 3-6a**, it is found that the surfactant tail has a preference for orienting parallel to the tube axis on (6,6) and (12,12) SWNTs. On (20,20) SWNT, the tail segments tend to lie with various angles to the nanotube axis. This can be explained by considering that linear SDBS surfactant has the dodecyl chain with length on the order of 2 nm. Thus, when adsorbing onto a narrow tube, particularly on (6,6) SWNT with diameter 0.814 nm, it is energetically favourable for the rigid tails to lie along the tube axis rather than to wrap around its circumference [26]. The probability distribution corresponding to the angle between the benzenesulfonate and the SWNT axis is shown in **Figure 3-6b**. One broad peak around 90° is observed on (20,20) SWNT, suggesting that the sulfonate

group orients preferentially perpendicularly to the tube. There is no preferential orientation of benzenesulfonate groups on (6,6) and (12,12) SWNTs. These results further confirm that the benzene rings do not lie on the nanotube surfaces, as would instead be expected based on the π - π interactions argument [26,30,38].

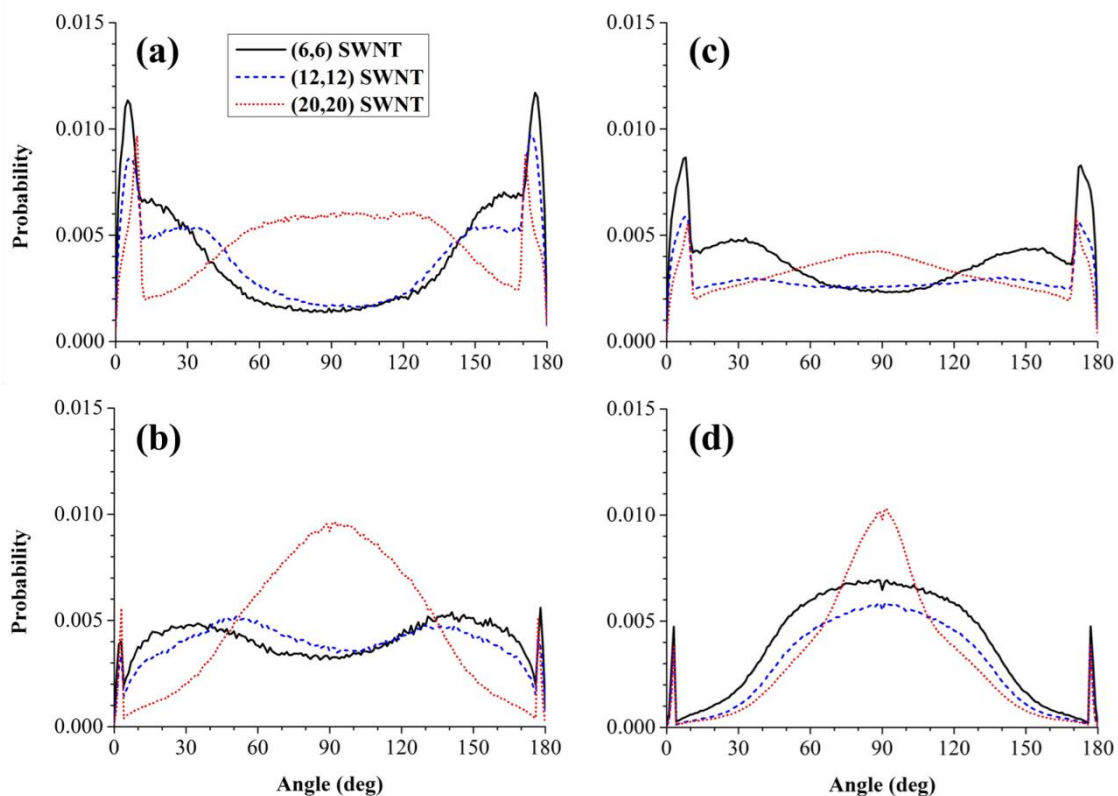


Figure 3-6: Probability distribution of orientation angle formed between (a, c) the vector of the surfactant tail and the SWNT axis and that between (b, d) the vector of the benzenesulfonate and the SWNT axis. In the left panels the results are obtained on the SWNTs at low surface coverage; in the right panels at high surface coverage. The solid, dashed, and dotted lines represent (6,6), (12,12), and (20,20) SWNTs, respectively.

At high surface coverage (right panels), the surfactant tails (**Figure 3-6c**) do not show pronounced preferred orientation. The noticeable peaks at 0° and 180° on (6,6) SWNT suggest some preference for parallel orientation on this SWNT. In **Figure 3-6d**, very broad peaks centred around 90° on (6,6) and (12,12) SWNTs are observed, indicating that the benzenesulfonate groups tend to lie perpendicular to the nanotubes. This tendency is more pronounced on the (20,20) SWNT, where the peak at 90° is sharper.

The small peaks at 0° and 180° indicate that a few benzenesulfonate groups orient parallel to SWNT axis.

In all the cases discussed so far, the structures of linear SDBS aggregates formed on the SWNTs do not agree with the model for the surfactant-nanotube aggregates suggested by Matarredona *et al.* [27]. These authors proposed that the SDBS surfactants lie perpendicular to the surface yielding a cylindrical micelle with the nanotube resting in the interior of the supramolecular complex. The simulations suggest that the linear SDBS aggregates are disordered at the SWNT surfaces. It should be remembered, however, that the simulations are conducted at low surfactant coverage. As the surfactant density increases, it is possible that multi-layered aggregates such as the one shown in the bottom panel of **Figure 3-3** are formed. Unfortunately, atomistic MD cannot be used, within the current computational resources, to investigate such systems.

3.4.2 Molecular architecture effect: Adsorption of branched SDBS

To quantify the SDBS aggregate morphology on SWNTs as a function of the SDBS molecular structure, the self-assembled aggregates formed by “branched” SDBS are studied at conditions comparable to those considered above. The branched SDBS molecules are obtained by grafting the benzenesulfonate to the fifth carbon atom in the dodecane backbone (see **Figure 3-1**). Representative simulation snapshots of branched SDBS adsorbed on (6,6), (12,12) and (20,20) SWNTs at low and high surface coverages are shown in **Figure 3-7** and **Figure 3-8**, respectively. Visual inspection of the simulation snapshots reveals significant qualitative differences compared to results obtained for linear SDBS at comparable surface coverages. A shared feature of snapshots in both figures is that the tail segments adsorb close to the substrates, while the benzene rings are located further from the nanotube surfaces, although next to the layer of tail segments. A large number of headgroups extend to the aqueous phase.

As in the case for linear SDBS, not all branched surfactants present within the various simulation boxes are found adsorbed on the SWNTs after equilibration. Integrating the number density profiles (shown below) near each SWNT up to a cut-off distance of 12

Å, the number of adsorbed branched SDBS was estimated, as well as that of non-adsorbed branched SDBS. The results, together with the effective surface coverage, are reported in **Table 3-2**.

On (6,6) SWNT, the packing density of the branched SDBS molecules is higher than that obtained for linear SDBS both at low and high surface coverages. This observation may be due to the molecular structure of branched SDBS, which appears to be compatible with the diameter of (6,6) SWNT. By contrast, on (12,12) and (20,20) SWNTs the adsorbed branched SDBS surfactants are fewer than linear SDBS. This may be due to preferential adsorption of branched SDBS on narrow SWNTs, although compelling data are not available to support this hypothesis.

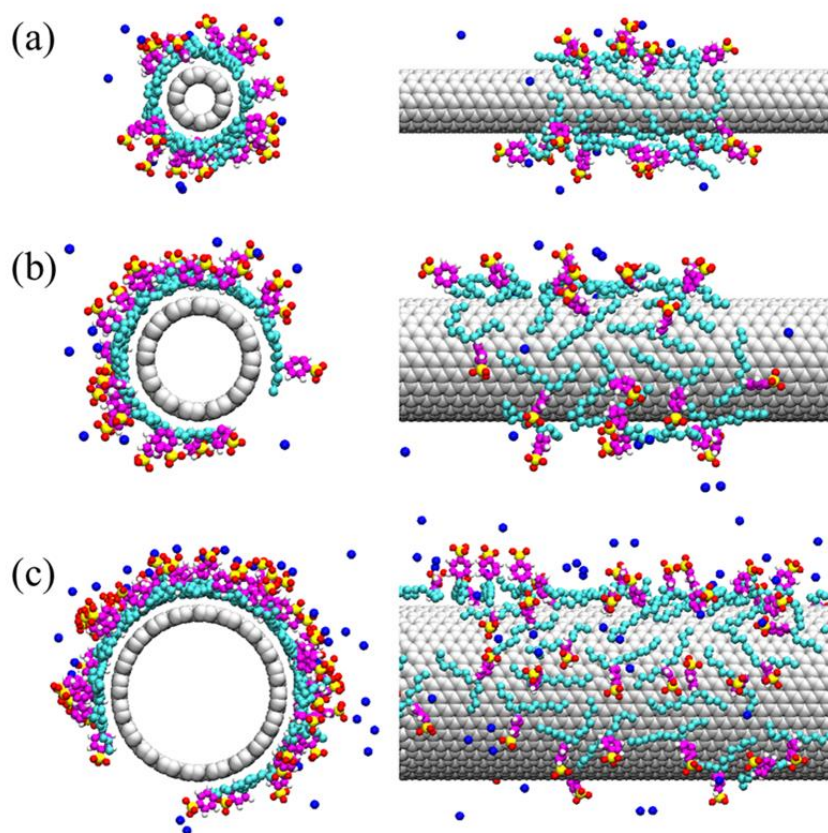


Figure 3-7: Front (left) and side (right) views of representative simulation snapshots of branched SDBS surfactants adsorbed on (a) (6,6), (b) (12,12), and (c) (20,20) SWNTs at low surface coverage. Water molecules are not shown for clarity. The colour code is the same as that used in **Figure 3-2**.

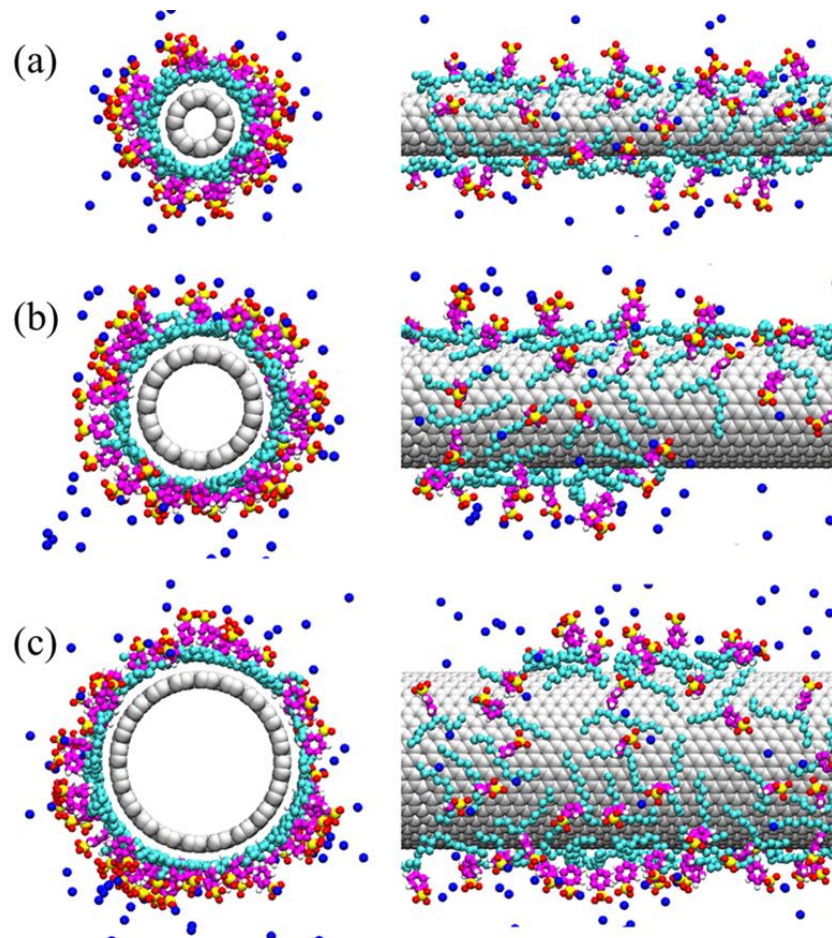


Figure 3-8: Same as **Figure 3-7** but for high surface coverage.

Table 3-2: Population analysis results of branched SDBS surfactants adsorbed on SWNTs

SWNT	No. of SDBS simulated [molecules]	Nominal SDBS surface coverage [molecules per nm ²]	No. of SDBS adsorbed [non-adsorbed] [molecules]	Effective SDBS surface coverage [molecules per nm ²]
(6,6)	19	1.0	19 [0]	1.0
(12,12)	38	1.0	23 [15]	0.6
(20,20)	63	1.0	55 [8]	0.9
(6,6)	53	2.8	40 [13]	2.1
(12,12)	106	2.8	46 [60]	1.2
(20,20)	178	2.8	61 [117]	1.0

As above in the case of linear SDBS, the properties of adsorbed branched SDBS were quantified, focusing on those surfactants found on the nanotubes after equilibration. The arrangements of adsorbed branched SDBS can be quantified by the density profiles of tail segments, benzene rings, headgroups, counterions, and water molecules away from the SWNT surfaces. In **Figure 3-9** (left panels), the density profiles of branched SDBS at low surface coverage are presented. The tail segments remain in contact with the nanotube surfaces, as indicated by the peak $\sim 4 \text{ \AA}$ (**Figure 3-9a**). Although a small portion of the benzene rings is located near the substrate, most of the benzene rings are positioned further from the SWNT surface, next to the monolayer formed by the tail segments (**Figure 3-9b**). The sulfonate headgroups tend to be exposed to water (**Figure 3-9c**). On (20,20) SWNT, a strong peak for the headgroup density profile is found at $\sim 10 \text{ \AA}$, indicating that headgroups are predominantly away from the nanotube surfaces. On all SWNTs, the Na^+ counterions accumulate near the headgroups due to the counterion condensation (**Figure 3-9d**), in qualitative agreement with results obtained for linear SDBS. A strong peak in the water density profiles is found at 3.5 \AA (**Figure 3-9e**), suggesting most of the water molecules are in contact with the nanotube surface.

The density profiles of branched SDBS at high surface coverage are shown in the right panels of **Figure 3-9**. The tail segments strongly adsorb on the three SWNTs, yielding a peak at 4 \AA (**Figure 3-9f**). It is possible to find a few benzene rings near the SWNT surfaces (**Figure 3-9g**), but most of the benzene rings are positioned further from the nanotube surfaces, next to the monolayer of tail segments, yielding the largest peak density at $\sim 6 \text{ \AA}$. The sulfonate headgroups are for the most parts extended into water (**Figure 3-9h**). The Na^+ counterions pack close to the charged of sulfonate headgroups (**Figure 3-9i**). Although it might be a coincidence, micellar structures formed at contact with branched SDBS adsorbed on the nanotubes were not observed when branched SDBS were simulated. As more branched SDBS are absorbed, more water molecules are expelled from the interfacial region, in particular on the (6,6) SWNT. Thus, the intensity of the peak at 3.5 \AA in the water density profiles decreases as the surfactant surface coverage increases (**Figure 3-9j**).

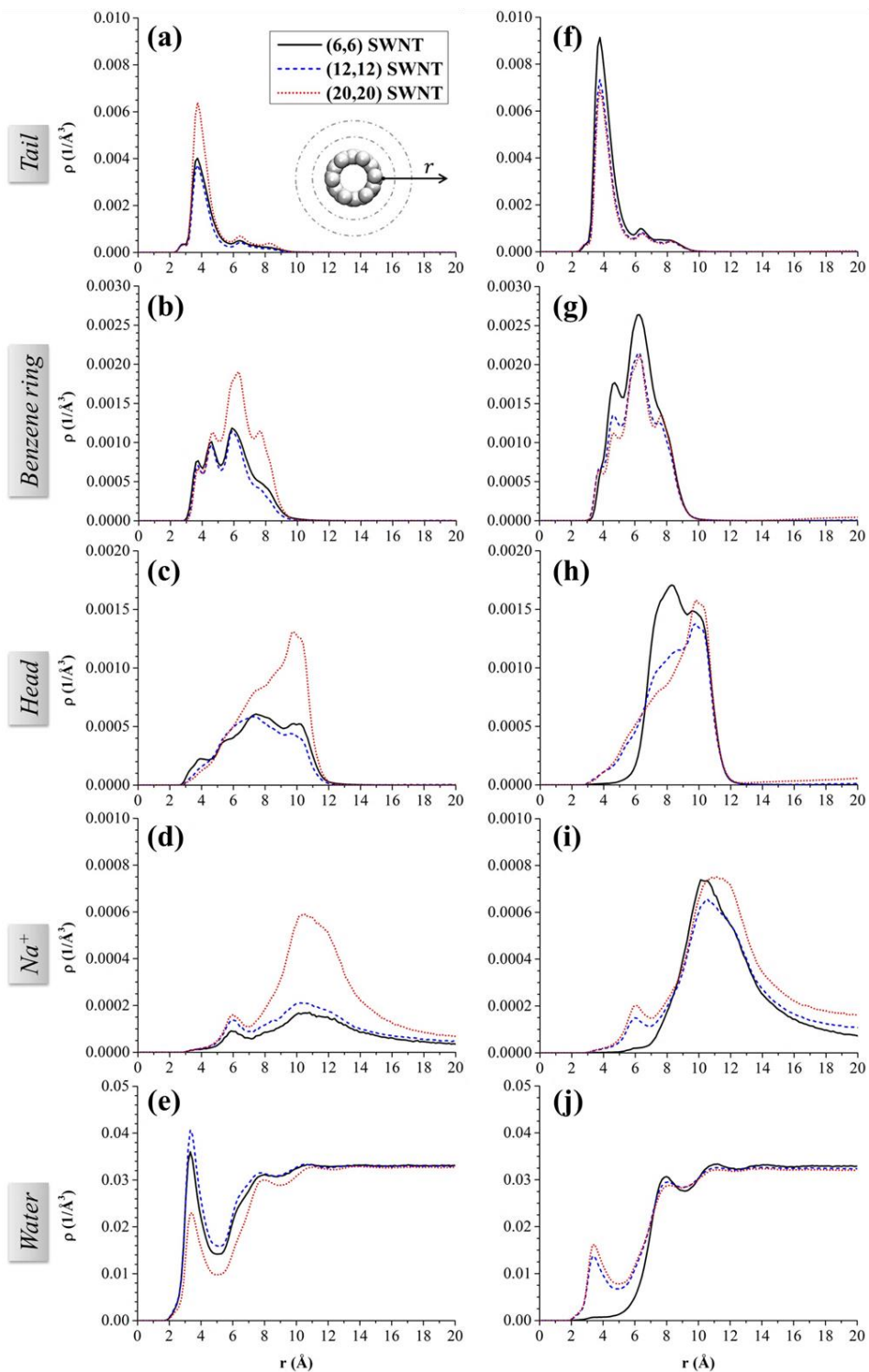


Figure 3-9: Density distributions of (a, f) tail segments, (b, g) benzene rings, (c, h) headgroups, (d, i) Na^+ counterions, and (e, j) water molecules relative to the SWNT (“ r ” is measured radially from the nanotube surface). The results are obtained for branched SDBS on the three SWNTs at low (left) and high (right) surface coverages. The solid, dashed, and dotted lines represent (6,6), (12,12), and (20,20) SWNTs, respectively.

In summary, the density profiles suggest that as the benzenesulfonate group moves from the end of the alkyl chain to the fifth carbon atom, a change in the aggregate morphology of SDBS on SWNTs can be observed

To quantify the orientation of branched SDBS adsorbed on the three SWNTs, the probability distribution of the angle between the vector identified by the surfactant tail and the SWNT axis, and that angle between the vector identified by the benzenesulfonate and the SWNT axis was calculated. For these calculations, only the branched SDBS molecules around the SWNT located up to a cut-off distance of 9 (tail) and 12 Å (sulfonate) from the SWNT surface were considered. A schematic describing the two vectors defined by one SDBS molecule is shown in **Figure 3-10**.

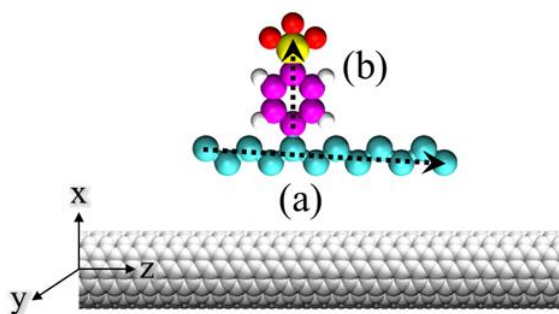


Figure 3-10: The vectors of (a) tail segment and (b) benzenesulfonate group used to calculate the probability distribution of the orientation angle between branched SDBS molecule and the SWNT axis (parallel to the Z-axis of the simulation box).

The probability distribution of the orientation of branched SDBS molecules on the various SWNTs is shown in **Figure 3-11**. The left and right panels are for results observed at low and high surface coverages, respectively. The results show no significant difference between the two surface coverages. The tail segments tend to form any angle to the SWNT axis (**Figure 3-11a** and **Figure 3-11c**). The benzenesulfonate groups tend to orient perpendicularly to the SWNT axis, indicating the broad peak at 90° (**Figure 3-11b** and **Figure 3-11d**). On the basis of the previous calculation for the potential of mean force between SWNTs in the presence of aqueous surfactants [42], the

ability to orient the SDBS headgroups perpendicularly to the SWNT axis should promote long-ranged repulsive forces between the nanotubes, and therefore should lead to effective stabilisation of aqueous dispersions.

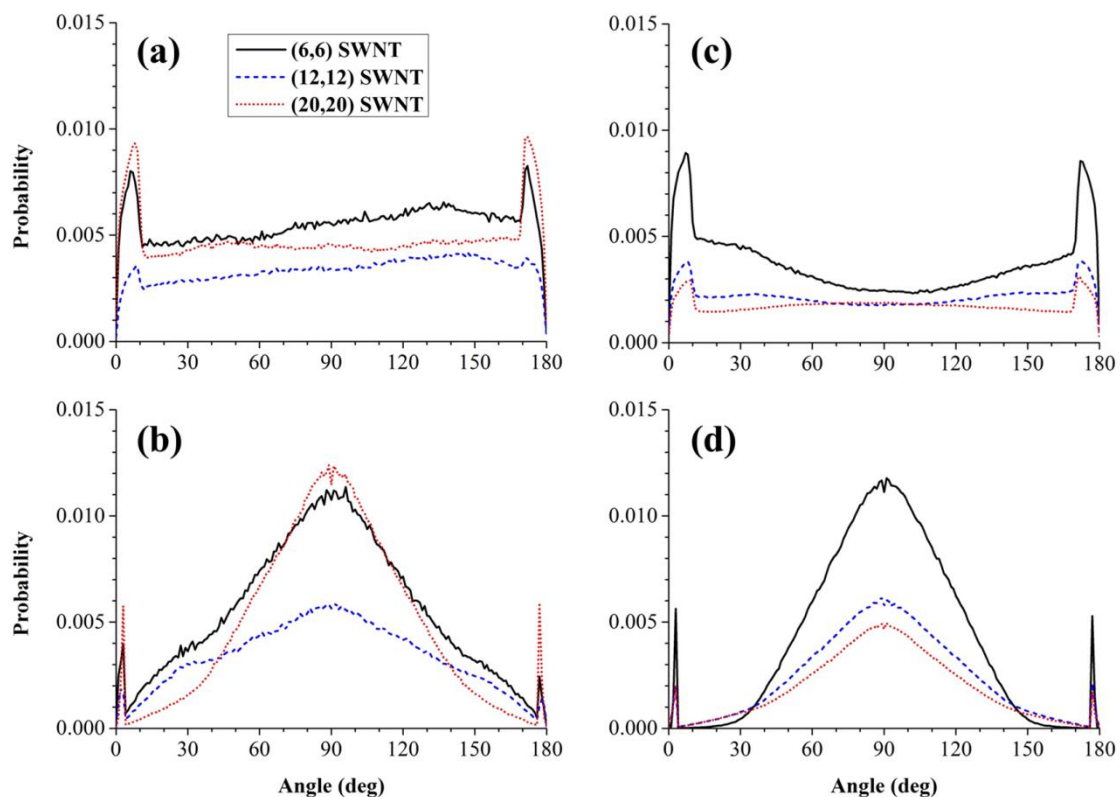


Figure 3-11: Probability distribution of orientation angle formed between (a, c) the vector of the surfactant tail and the SWNT axis and that between (b, d) the vector of the benzenesulfonate and the SWNT axis. In the left panels the results are obtained on the SWNTs at low surface coverage; in the right panels at high surface coverage. The solid, dashed, and dotted lines represent (6,6), (12,12), and (20,20) SWNTs, respectively.

3.5 Conclusions

All-atom molecular dynamics simulations were performed for elucidating the aggregate morphology of aqueous SDBS surfactants adsorbed on (6,6), (12,12), and (20,20) SWNTs. The effect of surface coverage and SDBS molecular structure was investigated. Because of computing limitations, relatively low surface concentrations were considered. The results showed that the self-assembly of SDBS molecules depends on

the surface coverage as well as the SWNT diameter. Changing the SDBS molecular architecture affects the surfactant arrangement on the nanotubes. The results were quantified using representative simulation snapshots, density profiles away from the nanotube surfaces, and orientation probability maps. Both surfactants tend to yield disordered aggregates on all the nanotubes simulated. Linear SDBS, especially at low surface coverages, tends to orient parallel to the (6,6) SWNT axis because of the relative rigidity of the surfactant tail and the small diameter of the nanotube. At low surface coverages the linear SDBS adsorbs via both surfactant tail and benzene ring on the nanotube surface. As the surface coverage increases, the surfactant headgroups protrude extensively towards the aqueous phase, effectively pulling the benzene rings present within SDBS away from the nanotube surfaces. The morphology of self-assembled aggregates formed by branched SDBS surfactants appears to depend more significantly on the SWNT diameter than those obtained for linear SDBS, especially at low coverages. Specifically, the branched SDBS simulated appears to be compatible with the curvature of (6,6) SWNTs. On all nanotubes considered the branched SDBS tails remain adsorbed onto the nanotube surfaces, while the benzene rings and the sulfonate groups protrude towards the aqueous phase. These results showed that it is possible to manipulate the morphology of self-assembled surfactant aggregates on SWNTs by tailoring their molecular architecture. Based on calculations for the effective potential of mean force between carbon nanotubes in aqueous surfactant systems available in the literature, it appears that by controlling the morphology of the surfactant aggregates will lead to the selective stabilisation of aqueous carbon nanotube dispersions.

Chapter 4 Equimolar Mixtures of Aqueous Linear and Branched SDBS Surfactants Simulated on Single-Walled Carbon Nanotubes

The material presented in this chapter was published in 2015, volume 5, pages 90049-90060 of RSC Advances.

4.1 Chapter overview

In **Chapter 3**, branched sodium dodecyl benzenesulfonate (SDBS) surfactants showed self-assembled structures on single-walled carbon nanotubes (SWNTs) that were strongly dependent on tube diameter. Those results suggested that branched SDBS, as opposed to their linear counterparts, could specifically stabilise SWNTs of narrow diameter. Experimental data, however, show that SDBS stabilises aqueous SWNTs of many diameters. This discrepancy between simulated and experimental results could be explained by the fact that experimental SDBS samples are isomeric mixtures (linear and branched isomers). Here molecular dynamics (MD) simulation results for equimolar mixtures of aqueous linear and branched SDBS on (6,6) and (20,20) SWNTs at ambient conditions are reported. The results suggest that there is no strong effect due to nanotube diameter on the morphology of mixed SDBS surfactant aggregates, although the adsorbed aggregate structure strongly depends on surfactant coverage. In-plane radial distribution functions suggest that linear and branched molecules distribute evenly onto the surfaces of (6,6) SWNTs, while some evidence of segregation, in which branched SDBS predominantly packs near other branched molecules, was obtained on (20,20) SWNTs at high surface coverage. These results suggest that the lack of specificity in stabilising aqueous dispersions of carbon nanotubes using SDBS surfactants is probably due to the presence of multiple isomeric molecules in commercial surfactant samples. Perhaps more importantly, these simulations suggest that using mixtures of surfactants could affect the structure of the adsorbed aggregates, and the stability of aqueous dispersion of carbon nanotubes.

4.2 Introduction

Surfactants are extensively used in stabilising dispersions of single-walled carbon nanotubes (SWNTs) [26]. As it is the case with polymers [19] and lipids [125], surfactants physically adsorb on the SWNT surfaces without altering their electronic properties. This adsorption is in general due to hydrophobic forces between the surfactant tails and the SWNT surfaces, yielding self-assembled structures in which the surfactant tails adsorb on the nanotube walls and the hydrophilic heads are exposed to water.

A wide variety of surfactants have been investigated for stabilising aqueous dispersions of SWNTs, and it is now well-known that the surfactant aggregates self-assembled on SWNTs depend on surfactant type [30,32,126,127], molecular architecture [128-131], concentration [31,45,132,133], the presence of salts [134-136], nanotube diameter [29,36,42], temperature [28], pH [127,137], etc. For example, flavin mononucleotide (FMN) surfactants were shown to provide selectivity in stabilising (8,6) SWNTs in water, due to the helical self-assembly of the flavin moiety on the SWNT surfaces [36]. Sodium dodecyl benzenesulfonate (SDBS) and sodium deoxycholate (DOC) were found to be effective dispersants for HiPCO nanotubes [24]. Sodium dodecyl sulphate (SDS) was found not as good a stabiliser as sodium cholate (SC) or SDBS for (9,4) SWNTs at 40°C [28]. Gemini surfactants with aromatic spacers were found able to disperse SWNTs at higher surfactant/SWNT weight ratios than SDS, SDBS, or cetyltrimethylammonium bromide (CTAB) [35]. Two co-surfactants (DOC and SDS) were used to successfully suspend and isolate individual SWNTs with diameter up to 1.7 nm [16].

Using molecular dynamics (MD) simulations, Tummala and Striolo [41] found disordered aggregates of SDS on SWNTs. Xu *et al.* [117] computed the potential of mean force (PMF) between SWNTs covered by SDS; the results showed that the structure of adsorbed aggregates affects the PMF, with higher surfactant densities yielding more repulsive pair potentials. Lin and Blankschtein [43] reported the structure of SC on SWNTs and calculated the SWNT-SWNT PMF. Suttipong *et al.* [64] reported

that the morphology of anionic dodecyl sulphate surfactants is affected by the counterions (Cs^+ instead of Na^+), with Cs^+ ions yielding a more compact coverage of (6,6) SWNTs. Lin *et al.* [138] examined how self-assembled SC, SDS, and CTAB aggregates pre-formed on a SWNT influence the adsorption of aryl diazonium salt. They found that less rigid surfactant structures facilitate the formation of ionic bonds between the nanotube and the aryl group. Shih *et al.* [139] developed coarse-grained (CG) MD simulations, combined with colloidal theories, to predict the amount of SC surfactant adsorbed as a function of bulk surfactant concentration. At high SC concentration small-diameter SWNTs can adsorb higher SC amounts than large-diameter ones, while the opposite occurs at low SC concentrations.

In **Chapter 3**, the effect of SDBS molecular structure on the morphology of adsorbed self-assembled aggregates was investigated. Isomerically pure linear and branched SDBS surfactants were considered in the calculations. While the simulations were analysed by quantifying the structure of the self-assembled aggregates on SWNTs of different diameter [i.e., (6,6), (12,12) and (20,20) SWNTs were compared] and at different surface coverage, combining the results with insights from PMF calculations [42], the results suggested that the branched molecules could be used to selectively stabilise aqueous dispersions of narrow, i.e., (6,6), SWNTs. This appears to be at odds with experimental observations. In fact, experiments show that SDBS can stabilise carbon nanotubes of a wide range of diameters [24,25,30,36,38,44]. The present investigation stems from the observation that commercial SDBS samples typically contain isomeric mixtures: the structure of self-assembled aggregates formed on (6,6) and (20,20) SWNTs is quantified by equimolar mixtures of linear and branched SDBS molecules, to understand whether the lack of specificity observed experimentally in the stabilisation of SWNTs using SDBS surfactants could be due to the isomeric composition of the typical commercial samples. Linear-rich and branched-rich SDBS surfactant mixtures were not simulated, as it is expected that such systems would show features more similar to isomerically pure SDBS surfactants (linear and branched, respectively). SDBS surfactants in which the benzene ring is tethered to carbon atoms other than the first or the middle of the alkane chain also were not considered, as it is

expected that these surfactants would yield results intermediate between those obtained for the surfactants considered here and in the prior work [140].

4.3 Methodology

MD simulations of aqueous mixtures containing SDBS surfactants self-assembled on (6,6) and (20,20) SWNTs were performed using the GROMACS 4.6.1 software package [141]. Each simulated system was composed of one SWNT, a 50:50 mixture of linear and branched dodecyl benzenesulfonate surfactants, a sufficient number of Na^+ ions to obtain an electrically neutral system, and water molecules. The schematic chemical structures for linear and branched SDBS surfactants are shown in the top panel of **Figure 4-1**. One SDBS consists of the dodecane backbone, one benzene ring, and one sulfonate head. In the branched molecule, the benzenesulfonate group is attached to the fifth carbon atom in the tail. Each portion of the surfactant [i.e., CH_2 (CH for branched) and CH_3 tail segments, centre of mass of benzene rings, centre of mass of the sulfonate group in the head groups, and Na^+ ions] and centre of mass of the water molecules were used in quantifying the density profiles away from the SWNT surface.

The vectors represented in the bottom panel of **Figure 4-1**, one to identify the surfactant tail \vec{v}_{tail} and the other to identify the benzenesulfonate segment \vec{v}_{bs} , were used to compute the probability distribution of the orientation angle between each SDBS molecule and the SWNT axis. \vec{v}_{tail} was defined as the vector originating from the terminal CH_3 group to the primary CH_2 (linear SDBS) or CH_3 (branched SDBS) group. \vec{v}_{bs} was defined as the vector originating from the carbon atom within the benzene ring [which is linked to CH_2 (linear SDBS) or CH (branched SDBS) group of the tail] to the sulphur atom of the head.

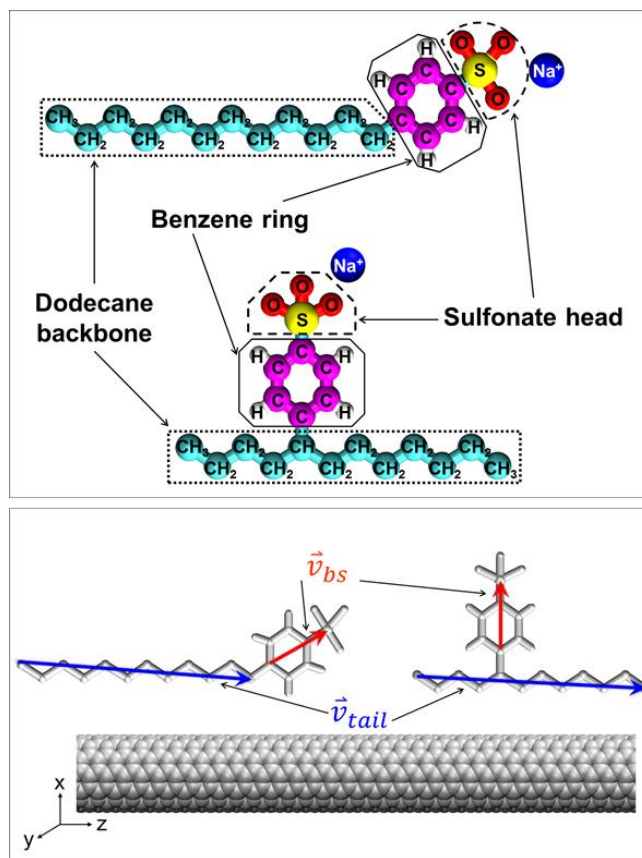


Figure 4-1: Top panel: schematic chemical structures of linear and branched SDBS surfactants; Bottom panel: vectors defined by surfactant tail \vec{v}_{tail} and benzenesulfonate segment \vec{v}_{bs} . Colour code: cyan for CH_n groups in surfactant tail; purple and white for carbon and hydrogen atoms in benzene rings, respectively; red for oxygen atoms; yellow for sulphur atoms; blue for Na⁺ ions; and grey for carbon atoms in SWNTs.

The (6,6) and (20,20) SWNTs of 7.44 nm in length were considered. Periodic boundary conditions were applied in three dimensions. Because of periodic boundary conditions, the SWNTs were infinitely long. The SWNTs diameters were of 0.814 and 2.713 nm for (6,6) and (20,20) SWNTs, respectively. The following SDBS surface coverages were examined: 1.0 SDBS molecules/nm² (\cong 1.0 nm²/headgroup) and 2.8 SDBS molecules/nm² (\cong 0.4 nm²/headgroup), which is referred to as ‘low’ and ‘high’ surface coverage, respectively. The composition of the simulation systems studied in this work is listed in **Table 4-1**. The number of water molecules was sufficient to obtain a

molecular density comparable to that of liquid water at ambient conditions far from the SWNTs (~ 33 water molecules per nm^3).

Table 4-1: Composition of simulated systems and population analysis results for equimolar mixtures of linear and branched SDBS surfactants adsorbed on SWNTs

SWNT	No. of C atoms in SWNT	No. of water molecules	No. of SDBS molecules simulated		Nominal surface coverage [molecules per nm^2]	No. of adsorbed [non-adsorbed] SDBS molecules				Effective surface coverage [molecules per nm^2]
			Linear	Branch		Linear	Branch	Linear	Branch	
(6,6)	520	24105	10	10	1.0	10	[0]	10	[0]	1.0
(20,20)	2400	21465	32	32	1.0	30	[2]	29	[3]	0.9
(6,6)	520	23441	27	27	2.8	22	[5]	22	[5]	2.3
(20,20)	2400	19313	89	89	2.8	48	[41]	32	[57]	1.3

The carbon atoms in SWNTs were treated as rigid uncharged Lennard-Jones (LJ) sites, based on the model proposed by Cheng and Steele [142]. SDBS surfactants were assumed to completely dissociate into dodecyl benzenesulfonate ions and Na^+ ions. The SDBS hydrophobic tails (dodecyl groups) were modelled as chains of united-atom LJ spheres [83,143,144]. The benzenesulfonate groups were described within the all-atom formalism using the DREIDING force field [145]. Water molecules were modelled using the SPC/E formalism [146].

In all simulated systems, one SWNT was maintained at the centre of the simulation box of size $10 \times 10 \times 7.44 \text{ nm}^3$, and kept rigid throughout the simulation. The empty space outside of the SWNT was filled with the solvent molecules (mixed linear and branched molecules, Na^+ ions, and water). The number of Na^+ ions was always equal to the number of surfactants. Water was placed in the simulation system by using the genbox algorithm available in GROMACS. As the nanotube is hollow, the software inserted water molecules within it. These were removed, as the behaviour of surfactants outside of the SWNTs was considered. The equations of motion were integrated with the leap-frog algorithm using a time step of 0.002 ps [79]. All simulations were conducted under the *NVT* ensemble using the Nose-Hoover thermostat with a relaxation time of 0.1 ps [79]. The long-range electrostatic interactions were calculated with the particle mesh Ewald method with a precision of 10^{-4} [124]. All interactions were treated with cut-off

set at 9 Å. The conjugate gradient algorithm was utilised to minimise the energy of the initial configurations for ~ 2 ps. To ensure that the results were not affected by the initial configurations, they were randomised by performing short (1 ns) MD runs at $T = 600$ K. The systems were then abruptly brought to $T = 300$ K, at which T equilibration was followed by production. Most systems were simulated for 250 ns, and one system, comprising of the (6,6) SWNT with surfactants at high surface coverage, was simulated for 300 ns. All systems were considered equilibrated when the results did not change over 50 ns of simulation time. Only the results collected during the last 20 ns of each simulation are reported in what follows.

4.4 Results and discussion

4.4.1 Aggregate morphology: Inspection of simulation snapshots

Representative simulation snapshots of an equimolar mixture of linear and branched SDBS surfactants adsorbed on (6,6) and (20,20) SWNTs at low and high surface coverages are shown in **Figure 4-2** and **Figure 4-3**, respectively. At low coverage, SDBS molecules lie flat on the SWNT surface. The surfactant tails and most benzene rings are close to the nanotube surfaces, while most of the head groups are slightly protruded into water. Some head groups can be found near the substrates. On (6,6) SWNT the linear SDBS molecules tend to align along the nanotube axis (see **Figure 4-2a**). Similar to what reported in the case of SDS [41], isomerically pure linear SDBS [140], CTAB [147], and single-tailed lipids [125] self-assembled on narrow SWNTs, this preferential orientation rises from the maximization of the contacts between the alkane chain and the SWNT surface, while minimizing the bending of the alkyl tails [148]. The branched SDBS molecules are found to assemble randomly on the nanotube surfaces on both (6,6) and (20,20) SWNTs at low coverage. On (20,20) SWNT, shown in **Figure 4-2b**, linear and branched SDBS surfactants wrap around the tube. Some linear molecules preferentially lie near each other, maximizing favourable tail-tail contacts. The simulation results show evidence of a few surfactants forming a small aggregate in water, even though unoccupied SWNT surface is available for adsorption. As noted previously [43], MD atomistic simulations are not long enough to describe the

equilibrium amount of surfactants adsorbed on a SWNT. The effective surface coverage observed in the simulations is reported in **Table 4-1** for all systems considered.

Upon increasing the surface coverage, the results in **Figure 4-3** show that equimolar SDBS mixtures not only pack more densely, but also remain highly disordered on both SWNTs. The results shown in **Figure 4-3a** demonstrate that at the conditions chosen linear and branched molecules cover most of (6,6) SWNT surfaces. Due to the reduction in nanotube surface area available per each surfactant molecule, most benzene rings and head groups are protruded toward the water phase. Similar behaviour is observed on (20,20) SWNT (**Figure 4-3b**), suggesting that the aggregate structure is due mostly to the surface density rather than to the SWNT diameter. Within the simulated system containing (20,20) SWNT, one surfactant micelle adsorbed on the aggregate, and two small micelles dispersed in water are observed, suggesting that perhaps the amount of surfactants simulated exceeds the maximum amount that could be adsorbed on this SWNT. It is possible that the amount of surfactant simulated was larger than that which can be adsorbed on (20,20) SWNT at the thermodynamic conditions considered, although it is also possible that the initial configurations led to the desorption of some of the surfactants from the nanotubes. As mentioned above, atomistic simulations are at present not able, because of computing power limitations, to assess the equilibrium amount of surfactants adsorbed. Coarse-grained approaches such as those proposed by Lin *et al.* [138] will allow this type of calculations. Because a few surfactants desorbed in some of the systems simulated, the effective surface coverage differed from the nominal one in some cases. Both effective and nominal surface coverages are reported in **Table 4-1**. At high surface coverage, the simulation snapshots suggest that there is no preferential orientation of the linear molecules with respect to the nanotube axis, but instead the linear molecules tend to adopt random orientations.

In all cases considered in **Figure 4-2** and **Figure 4-3**, it is clear that many counterions accumulate near the head groups. This is due to the strong electrostatic interactions between the oppositely charged groups on the sulfonate heads and on the Na⁺ counterions. On (20,20) SWNT, at high surface coverage it can be observed a high concentration of Na⁺ ions sandwiched between the head groups belonging to the

surfactants in the micelle and those adsorbed on the SWNT (see **Figure 4-3b**). Several reports document similar counterion-condensation phenomena [41,43,54,64,140].

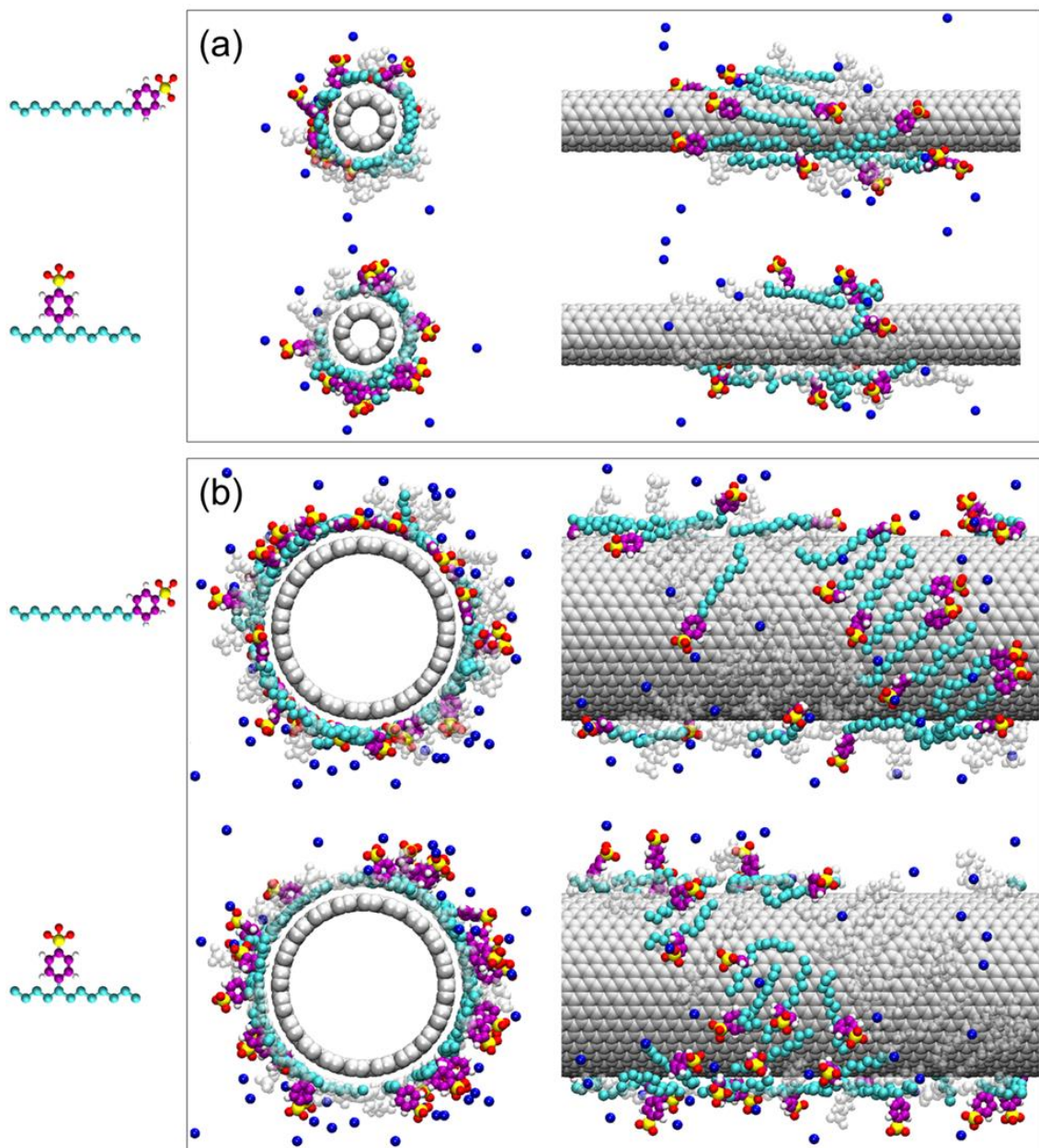


Figure 4-2: Front (left) and side (right) views of representative simulation snapshots for mixed linear and branched SDBS surfactants self-assembled on (a) (6,6) and (b) (20,20) SWNTs at low surface coverage. In the top panels of (a) and (b) the linear SDBS molecules are highlighted (the branched isomer is transparent); in the bottom panels the branched SDBS molecules (the linear isomer is transparent). Water molecules are not shown for clarity. The colour code is the same as that used in **Figure 4-1**.

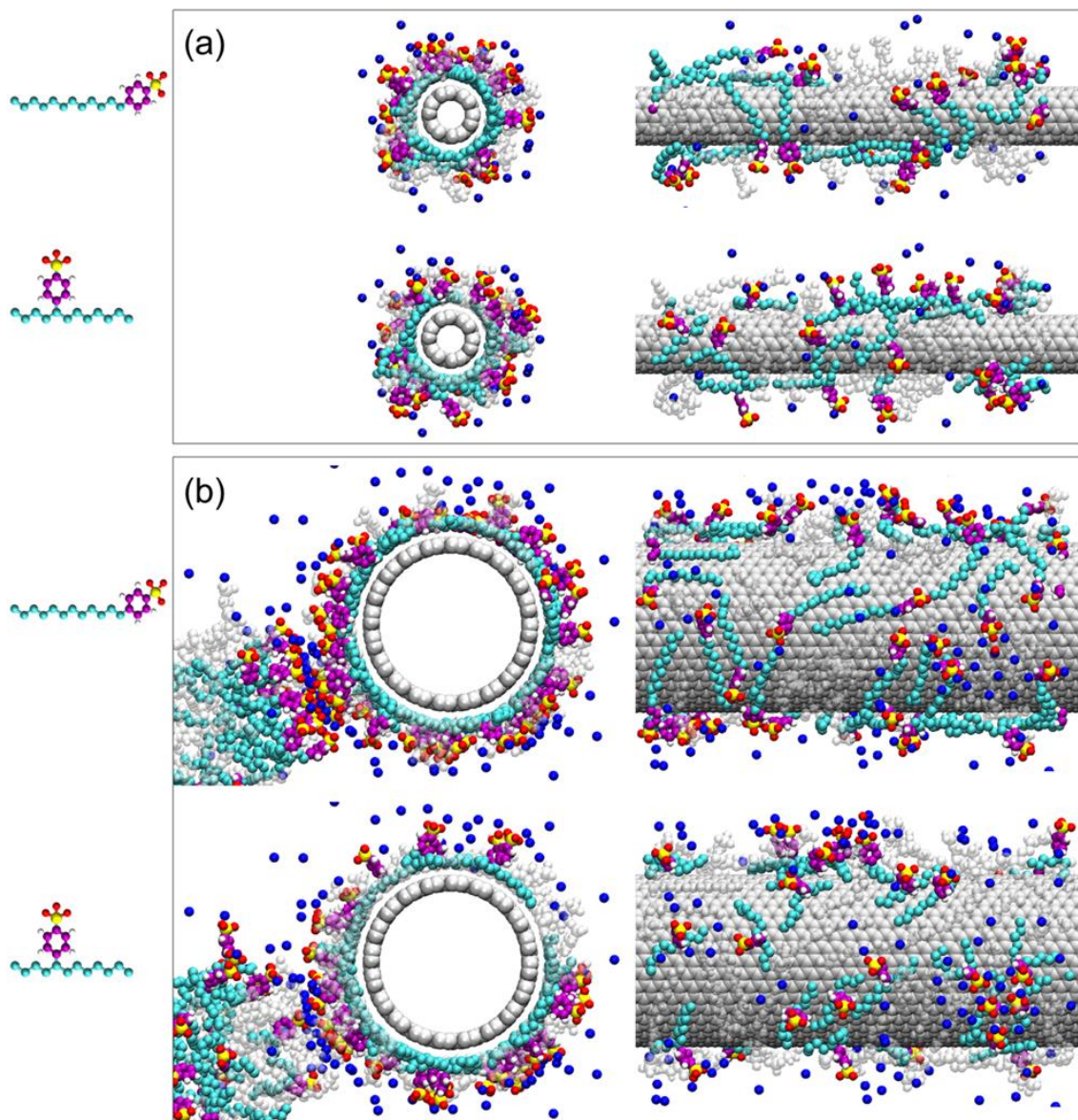


Figure 4-3: Same as **Figure 4-2** but for high surface coverage.

4.4.2 Effective surface coverage

To quantify the effective surfactant coverage on the SWNTs, the time-averaged number of surfactant molecules adsorbed was computed. One surfactant molecule was considered adsorbed if its centre of mass was found within a cut-off distance of 12 Å and 14 Å at low and high surface coverages, respectively, from the nanotube surface. The number of non-adsorbed SDBS molecules was calculated as the difference between

the latter number and the total number of SDBS molecules in the simulation box. Results regarding the population analysis are shown in **Table 4-1**. At low surface coverage all surfactants (linear and branched) remain adsorbed on the (6,6) SWNT, yielding the effective surface coverage of 1.0 molecules per nm² ($\cong 0.95$ nm² per SDBS head group). In the case of (20,20) SWNTs some SDBS molecules form one small aggregate in the bulk, yielding a higher effective surface coverage than that obtained on the narrow SWNT. As the number of surfactants in the simulated system increases, the number of non-adsorbed surfactants also increases, with the trend more pronounced on the (20,20) than on the (6,6) SWNT. On the (6,6) SWNT both at low and at high surface coverages, the numbers of linear and branched molecules adsorbed onto the tubes are equivalent, maintaining an equimolar surfactant mixture. This is not the case for the (20,20) SWNT, on which the adsorbed surfactants are enriched in linear molecules at both conditions considered. While these results suggest that perhaps different surfactant isomers have different propensity for adsorbing on the SWNTs, this cannot be guaranteed by the present simulations, because of the already mentioned limitations in the real time accessible with the available computing power. This, however, does not compromise the conclusions from the present study.

4.4.3 Aggregate morphology: Radial density profiles

The structural observations were quantified by calculating density distributions of surfactant tail, benzene ring, sulfonate head, Na⁺ ion, and water along the radial distance from the nanotube surface. These results are reported in **Figure 4-4**. Left and right panels are obtained at low and high surface coverages, respectively. At low surface coverage, the results suggest no strong effect of SWNT diameter on the adsorbed aggregate. Only the intensity of the peaks depends on the nanotube diameter. A strong peak in the density profiles of the tail groups at 4.0 Å is observed, indicating the formation of one surfactant layer near the SWNT surfaces (**Figure 4-4a**). It should be noted that this aggregate structure on (6,6) SWNT is different than that proposed by Matarredona *et al.* [27], who suggested the formation of a cylindrical micelle of SDBS molecules with SWNTs at the centre. The results are instead consistent with a disordered surfactant aggregate on the SWNT surfaces, which has been discussed for many

simulated surfactant-SWNT systems reported in the literature [54]. The surfactant aggregate is expected to resemble that proposed by Matarredona *et al.* [27] only when the surfactants surface density is extremely high [117].

The density profiles obtained at low surfactant density show that most benzene rings are positioned close to the substrates, yielding a peak at 4.0 Å and a shoulder at 6.0 Å (**Figure 4-4b**). Although some head groups are located near the SWNTs, as illustrated by two small peaks at 4.0 Å and 5.5 Å (**Figure 4-4c**), one broad peak located at 7.5-10 Å from the nanotube surfaces indicates that the head groups are in large part projected towards water. On the two SWNTs, the results obtained for the counterion density profiles show that the Na⁺ ions strongly correlate to the head groups (**Figure 4-4d**). In water density profiles, density peaks of high intensity at 3.5 Å are observed, notably for (6,6) SWNT, suggesting that the amount of surfactants available on the nanotube surface are too low to prevent water from being contact with the SWNTs (**Figure 4-4e**).

When the surface coverage increases, the peak at 4.0 Å in the tail density profiles for (6,6) and (20,20) SWNTs becomes stronger, suggesting that the surfactant monolayer becomes more compact via the packing of linear and branched molecules on the nanotube surfaces (**Figure 4-4f**). The benzene rings are mainly away from (6,6) SWNT, as demonstrated by a strong density peak at 6.5 Å (**Figure 4-4g**), although some benzene rings remain positioned near the nanotube surface. The majority of head groups on (6,6) SWNT are projected into water, manifesting a broad peak at ~ 9.0 Å (**Figure 4-4h**), while a few remain in contact with (20,20) SWNT surfaces, as suggested by the density peaks at 4.0 Å and 5.5 Å. On (20,20) SWNT, a small peak at 14 Å in the head group density profiles is due to the formation of the micellar aggregate adsorbed on the aggregate (the snapshot discussed in **Figure 4-3b**). As mentioned above, coarse-grained approaches are needed to clarify why some surfactants desorb from the nanotubes. The counterion density profiles show that the Na⁺ ions pack close to the head groups, yielding a strong peak at ~ 10.0 Å (**Figure 4-4i**). On (20,20) SWNTs, some Na⁺ ions are located near the substrate, where they are attracted by the presence of sulfonate heads.

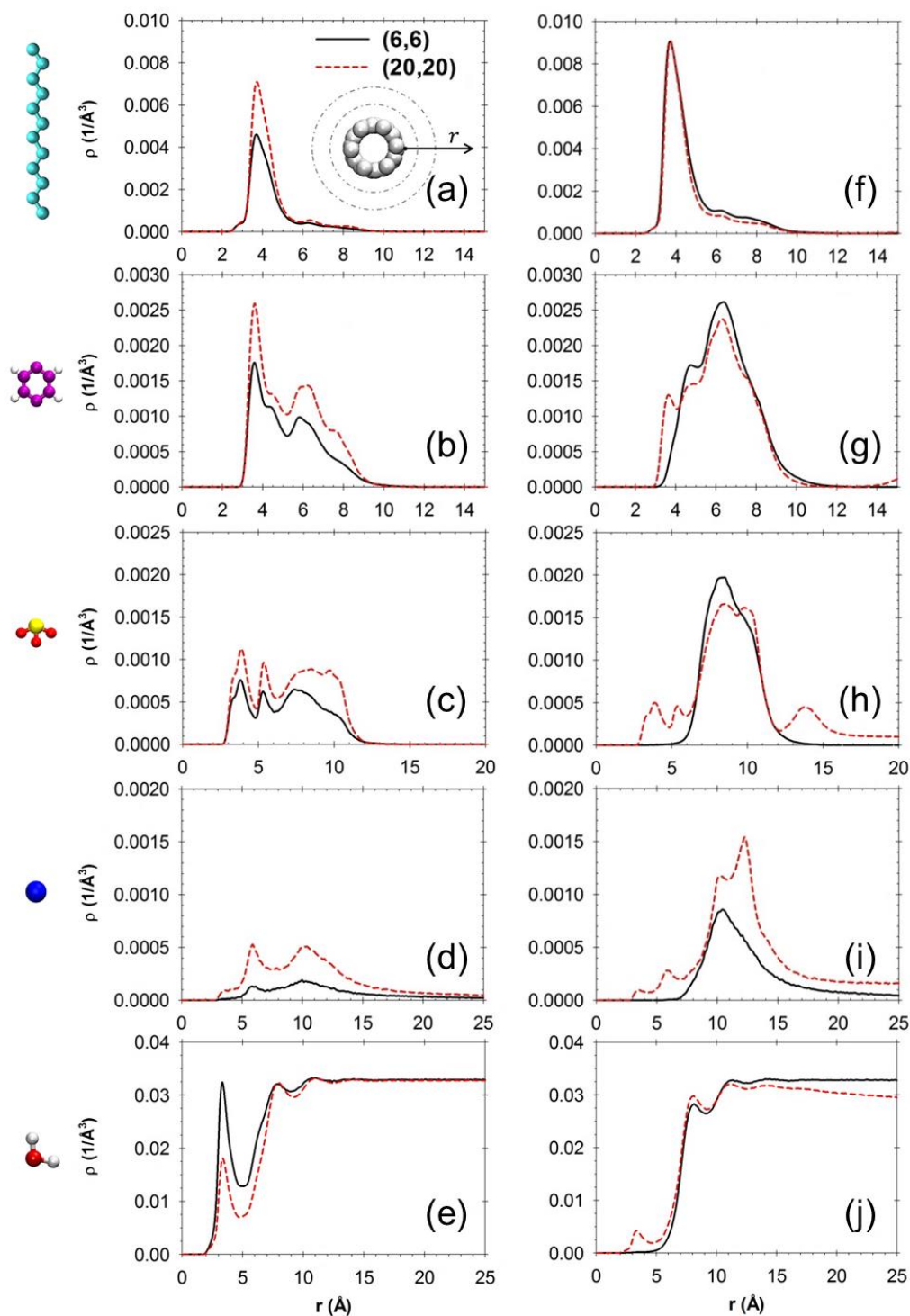


Figure 4-4: Atomic density profiles of (a, f) tails, (b, g) benzene rings, (c, h) head groups, (d, i) Na^+ ions, and (e, j) water molecules relative to the SWNT (r is measured radially from the nanotube surface). The results are obtained for mixed linear and branched SDBS at low (left) and high (right) surface coverages, respectively. The black-solid and red-dashed lines represent the results obtained on (6,6) and (20,20) SWNTs, respectively. System compositions and effective coverages are reported in **Table 4-1**.

The density profiles of water show the disappearance of the density peak at 3.5 Å for (6,6) SWNT, suggesting that adsorbed linear and branched SDBS surfactants are effective at shielding the narrow (6,6) SWNT from being at contact with water (**Figure 4-4j**). In the case of (20,20) SWNT, however, a small amount of water near the nanotube surface is still observable.

In summary, based on the results at low and high surface coverages, the structure of linear and branched SDBS aggregates formed on the SWNTs does not depend strongly on the nanotube diameter. It is worth noting that the position of the head groups is expected to play an important role in the stabilisation of aqueous SWNT dispersions [41,43,117]. Prior simulations have indeed suggested that the electrostatic repulsion between like-charged head groups, as well as the steric repulsion between such groups experienced at relatively close nanotube-nanotube separations, are necessary for stabilising aqueous SWNT dispersions.

4.4.4 Surfactant packing arrangement on SWNT surfaces

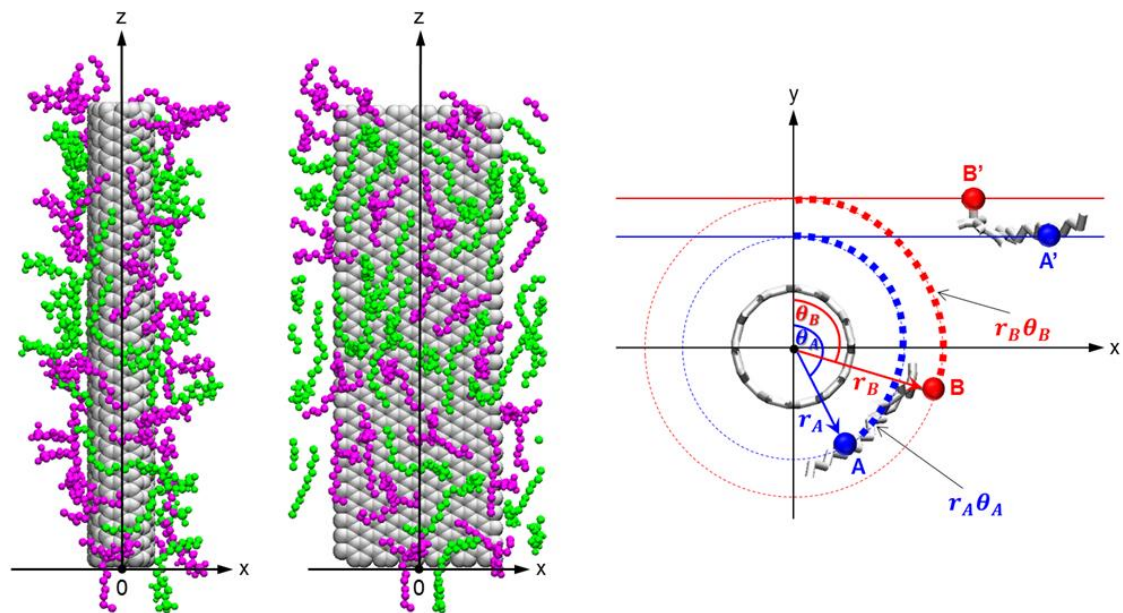


Figure 4-5: Left panel: SDBS surfactants adsorbed on a (6,6) SWNT. Middle panel: projection of the adsorbed surfactants on a plane. Right panel: schematic for the algorithm implemented to project atoms A and B of adsorbed surfactant onto a flat plane, where they are labelled A' and B' . Linear and branched SDBS are shown in green and purple, respectively. Water molecules are not shown for clarity.

To quantify whether linear and branched surfactants segregate from each other on the SWNT surfaces, in-plane radial distribution functions (RDFs) between the sulphur atoms in the head groups were computed. Only the adsorbed surfactants were considered for these calculations. The position of each atom of the surfactants adsorbed on the SWNT was projected onto a plane parallel to the nanotube axis. According to this procedure, the projected x' , y' and z' coordinates of an atom (originally in position x , y , and z) are obtained, as illustrated in **Figure 4-5**, by unwrapping a circular arc of length $r\theta$ onto a linear segment [r is the distance between the atom of interest and the centre of the nanotube, θ is the angle between the reference vector (oriented from the centre of the nanotube along the Y direction, as illustrated in **Figure 4-5**), and the vector connecting the centre of the nanotube to the atom of interest]. The x' coordinate then equals $r\theta$. The y' coordinate corresponds to the radial distance of the atom from the centre of the nanotube ($y'=r$). The z' coordinate corresponds to the z coordinate of the atom.

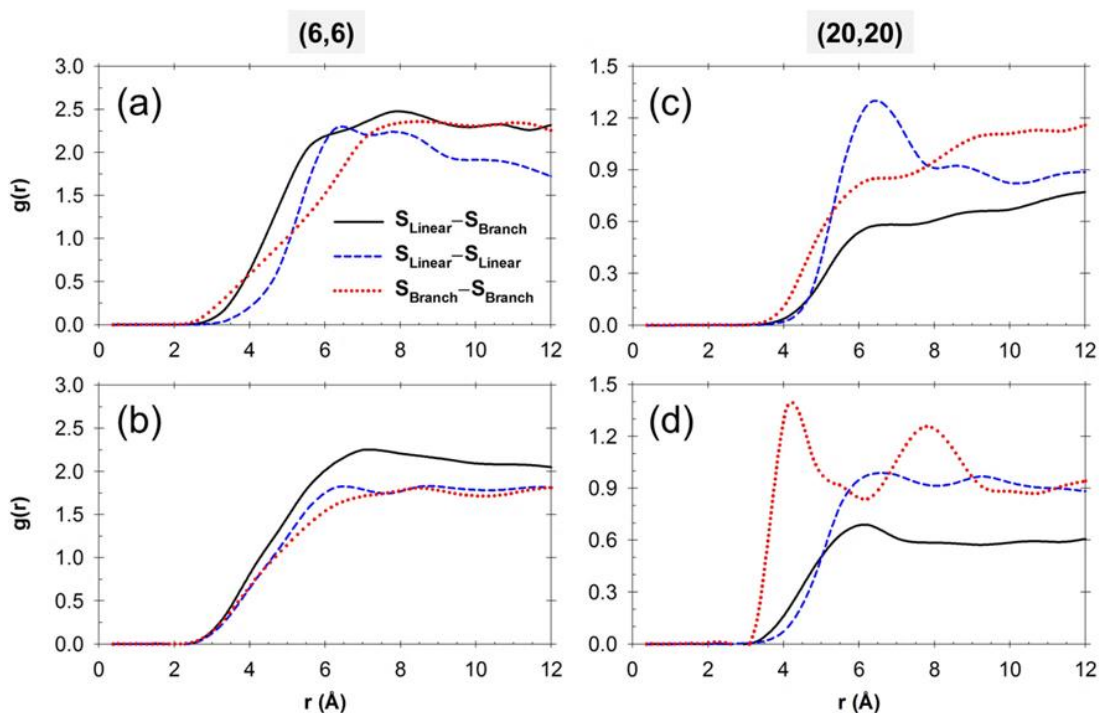


Figure 4-6: In-plane sulphur-sulphur radial distribution functions (RDFs) for SDBS molecules adsorbed on (a, b) (6,6) and (c, d) (20,20) SWNTs. The results are obtained at low (top panels) and high (bottom panels) surface coverage, respectively. The black-solid, blue-dashed, and red-dotted lines represent results for linear-branched, linear-linear, and branched-branched SDBS molecules, respectively.

The unwrapped coordinates were used to calculate in-plane RDFs [81]. The in-plane RDFs between linear-branched, linear-linear, and branched-branched SDBS molecules self-assembled on (6,6) and (20,20) SWNTs are shown in **Figure 4-6**. On (6,6) SWNT, at low and high surface coverages (**Figure 4-6a** and **Figure 4-6b**, respectively) the results are indicative of random packing, suggesting that linear and branched SDBS surfactants do not segregate on this substrate but instead they mix on the nanotube surfaces. On (20,20) SWNT, at low surface coverage a relatively strong peak at 6.5 Å in the RDF between linear surfactants is instead observed (**Figure 4-6c**), suggesting that the linear isomers prefer to segregate with other linear surfactants. Some evidence of preferential segregation among branched surfactants is observed at high surface coverage (**Figure 4-6d**), but in general the results are consistent with a good degree of mixing of the two surfactant types on both SWNTs. Note that, theoretically, a liquid or gaseous RDF approaches unity at large r . RDF with positive, non-unity values imply an enhanced or reduced probability relative to being evenly distributed [149]. Since branched SDBS mostly packs near other branched molecules, in **Figure 4-6d**, the RDF between linear and branched SDBS surfactants is conceivably less than one.

4.4.5 Discussion

In this section the preferential orientation of linear and branched SDBS molecules adsorbed on SWNT surfaces was analysed, and the results were compared to those obtained for isomerically pure surfactants presented in **Chapter 3** (Ref. [140]). The orientation vectors shown in **Figure 4-1**, bottom panel, with respect to the SWNT axis were considered. An angle of 0° or 180° indicates that the correspondent vector is parallel to the nanotube axis, 90° indicates that the vector is perpendicular to the nanotube axis. The results are shown in **Figure 4-7** and **Figure 4-8**, obtained on (6,6) and (20,20) SWNTs, respectively, in the form of probability distributions.

On (6,6) SWNT at low surface coverage, the surfactant tails of equimolar mixtures of linear and branched SDBS surfactants tend to be parallel to the SWNT axis, as indicated by the largest peaks in the angle distribution profiles at 0° and 180° (**Figure 4-7a**). At these conditions the benzenesulfonate segments are preferentially perpendicular to the

SWNT axis, yielding one broad peak centred at $\sim 90^\circ$ (**Figure 4-7b**). As the surface coverage increases, the surfactant tails in equimolar SDBS mixtures are neither parallel nor perpendicular to the nanotube axis (**Figure 4-7c**), while a significant amount of benzenesulfonate groups remain perpendicular to the tube axis (**Figure 4-7d**). Comparing the probability distributions just discussed against those obtained for pure linear and branched SDBS molecules, the results suggest that the surfactants from an equimolar mixture of linear and branched surfactants behave preferentially like pure branched SDBS surfactants, which orient their benzenesulfonate groups for the most part perpendicularly to the nanotube axis. This is probably a consequence of the fact that when both linear and branched surfactants are present on the nanotube (1) the surfactant molecules wrap more tightly around (6,6) SWNT than pure linear isomers do, and (2) linear molecules within the equimolar mixtures accommodate the presence of the branched counterparts.

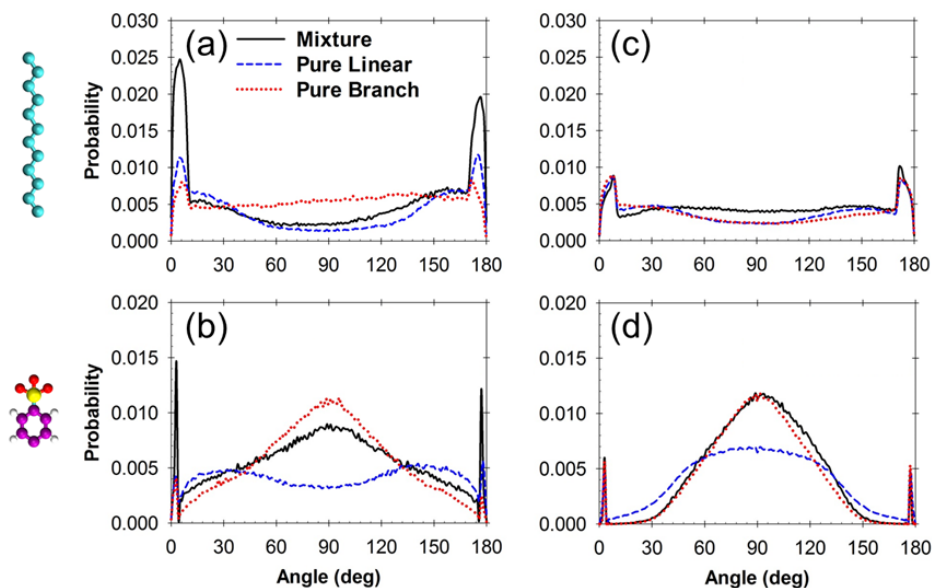


Figure 4-7: Probability distribution of (a, c) the surfactant tail and (b, d) the benzenesulfonate segment orientation angle with respect to the (6,6) SWNT axis. In the left and right panels the results are obtained at low and high surface coverages, respectively. The black-solid, blue-dashed, and red-dotted lines represent the results obtained for mixed linear and branched, pure linear, and pure branched molecules, respectively. The results of pure linear and branched SDBS are reproduced from Ref. [140].

On (20,20) SWNT, at low and high surface coverages the results show no significant difference in orientation probability distributions for either surfactant tails or benzenesulfonate groups among those obtained for equimolar SDBS mixtures, pure linear and branched surfactants (**Figure 4-8**). The surfactant tails tend to form any angle with respect to the nanotube axis (**Figure 4-8a** and **Figure 4-8c**), while the benzenesulfonate segments mainly orient perpendicular to it, as indicated by the broad peak at 90° .

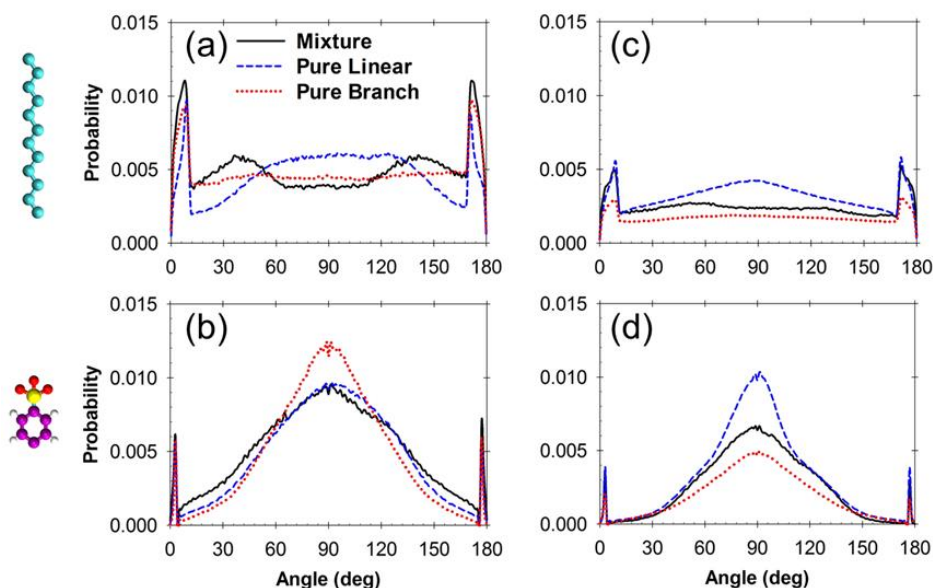


Figure 4-8: Same as **Figure 4-7** but for surfactants adsorbed on (20,20) SWNTs. The results of pure linear and branched SDBS are reproduced from Ref. [140].

Finally, the radial density profiles obtained from equimolar mixtures of linear and branched SDBS surfactants were compared to those obtained for pure linear and branched ones [140]. The results are shown in **Figure 4-9** and **Figure 4-10**, obtained on (6,6) and (20,20) SWNTs, respectively. On (6,6) SWNT, at low surface coverage the peak positions of each surfactant segment (i.e., tail groups, benzene rings, head groups, and Na^+ ions) and water molecules in the density profiles for equimolar SDBS mixtures are found near the correspondent peaks obtained for pure linear and branched surfactants (**Figure 4-9**, left panels). This can, for instance, be seen clearly in the benzene ring and

sulfonate group density profiles, in which some benzene rings and head groups for equimolar SDBS mixtures remain in contact to the nanotube surfaces (which is consistent with results obtained for pure linear surfactants), while some other benzene rings are further from substrate (consistent with results obtained for pure branched molecules). When the surface coverage increases, the adsorbed aggregates formed by equimolar SDBS mixtures are very similar to those obtained for the pure branched surfactants (**Figure 4-9**, right panels). In particular, the results show that most head groups from the equimolar mixture of linear and branched SDBS surfactants are exposed to water, as was the case for pure branched surfactants. The Na^+ ions accumulate near their head groups. On (20,20) SWNT the radial density profiles obtained for the equimolar mixtures of linear and branched SDBS surfactants show that the results obtained for the surfactants near the tube surfaces are similar to those obtained for the pure linear surfactants, while those obtained for the surfactants whose heads are protruded into water are similar to those obtained for pure branched SDBS surfactants. This is observed both at low (**Figure 4-10**, left panels) and high (**Figure 4-10**, right panels) surface coverages.

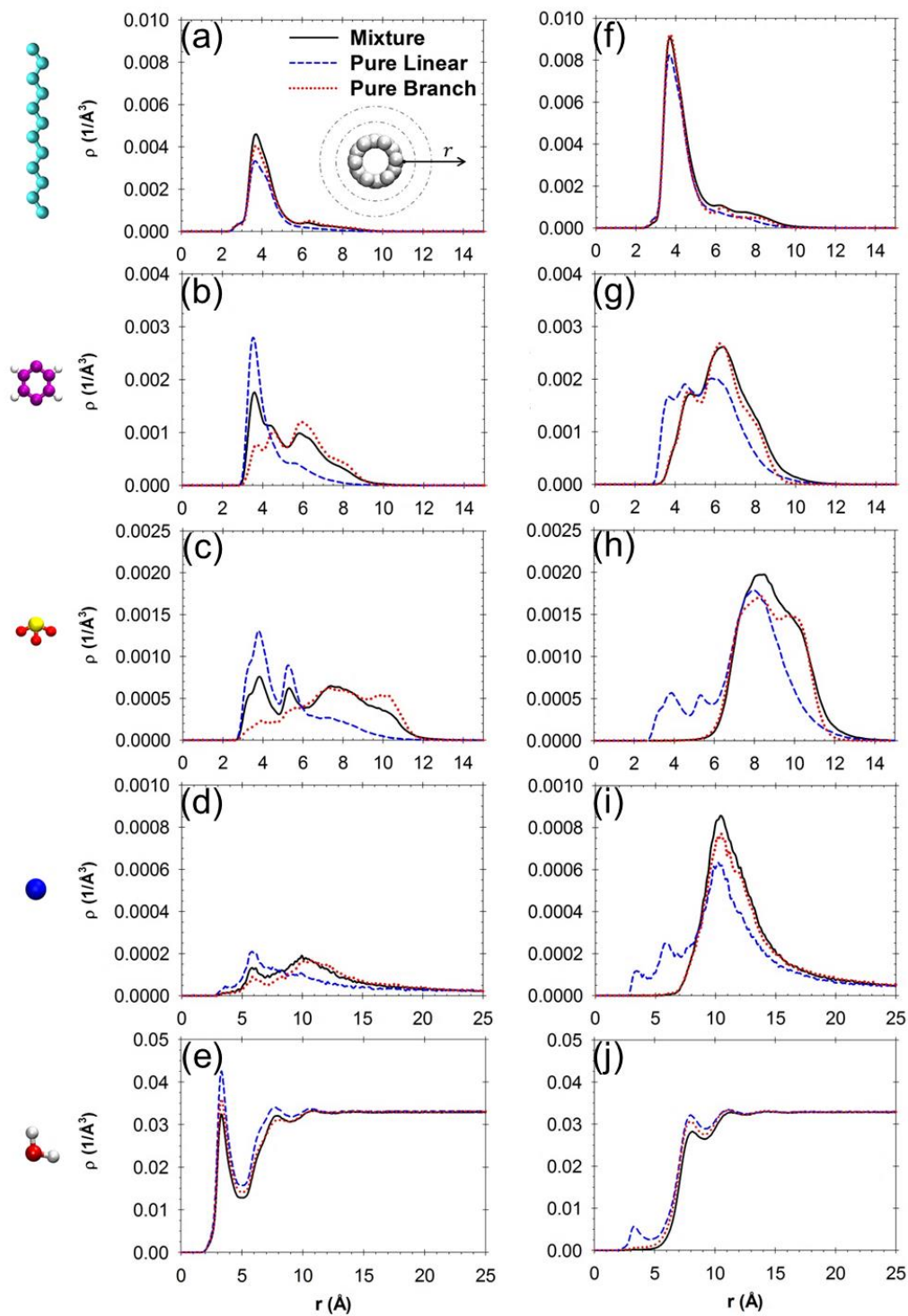


Figure 4-9: Radial atomic density profiles of (a, f) surfactant tails, (b, g) benzene rings, (c, h) sulfonate heads, (d, i) Na^+ ions, and water molecules relative to the SWNT. The results are obtained for mixed linear and branched (black-solid line), pure linear (blue-dashed line) and pure branched (red-dotted line) surfactants adsorbed on the (6,6) SWNT, at low (left panels) and high (right panels) surface coverages. The results of pure linear and branched SDBS are reproduced from Ref. [140].

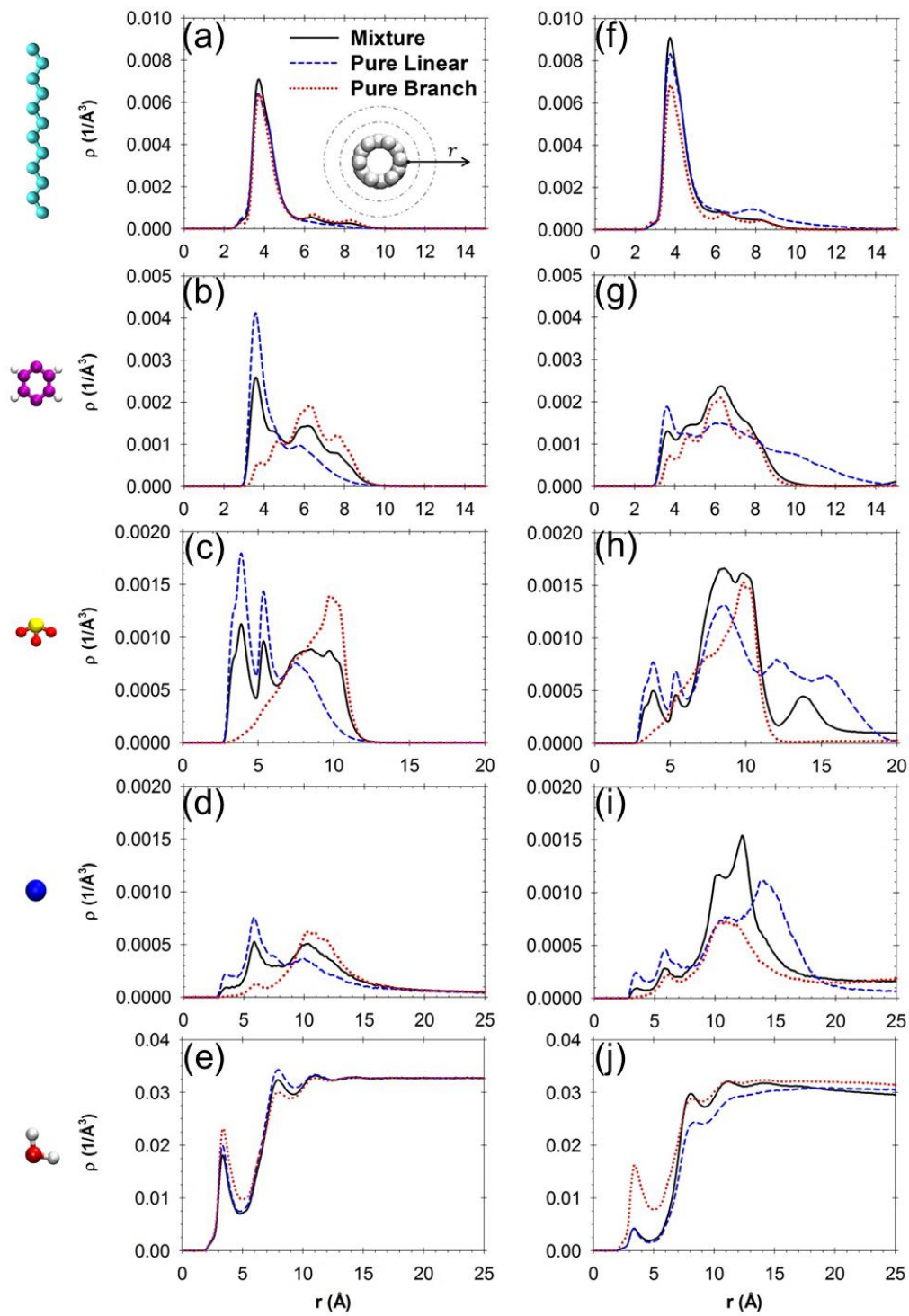


Figure 4-10: Same as **Figure 4-9** but for the (20,20) SWNT. The results of pure linear and branched SDBS are reproduced from Ref. [140].

4.5 Conclusions

All-atom molecular dynamics simulations were employed to investigate the morphology of equimolar mixtures of linear and branched SDBS surfactants on (6,6) and (20,20) SWNTs in water. Equimolar SDBS mixtures were found to yield disordered aggregates on both SWNTs, although the aggregate structure depends on surface coverage. At both surface coverages considered, the surfactant tails pack on the SWNT surfaces, while the head groups tend to extend more towards water as the surfactant coverage increases. No significant changes in the structure of the adsorbed aggregates as a function of the SWNT diameter were observed. Comparing the self-assembled aggregates formed by equimolar SDBS mixtures against prior simulation results obtained for isomerically pure linear and branched SDBS surfactants at comparable surface densities, it was found that, in general, mixtures of SDBS surfactants yield features (e.g., probability orientation distribution and radial density profiles for each surfactant portion) that are consistent with those obtained for either pure linear or pure branched SDBS surfactants. These simulation results suggest that experimentally SDBS does not show the ability of stabilising SWNTs of selective diameters because experimental samples contain isomeric mixtures of the surfactants. While experimental validation is required to assess the reliability of the predictions, the simulations suggest that using mixtures of different surfactants could help manipulate the stability of aqueous dispersions of carbon nanotubes, which is consistent with recent advances reported in the literature (*ACS Nano*, 2015, **9**, 5377).

Chapter 5 Salt-Specific Effects in Aqueous Dispersions of Carbon Nanotubes

The material presented in this chapter was published in 2013, volume 9, pages 3712-3719 of *Soft Matter*.

5.1 Chapter overview

Tremendous progress has been made to stabilise carbon nanotube dispersions using surfactants. Although theoretical investigations have uncovered, often using molecular simulations, some of the molecular phenomena thought to be responsible for the dispersions stability, many questions await answer to design surfactant formulations that selectively stabilise nanotubes monodispersed in diameter and chirality. Stimulated by experimental observations [*JACS*, 2010, **132**, 16165], how changing the counterion (Cs^+ instead of Na^+) affects the morphology of dodecyl sulphate surfactants adsorbed on carbon nanotubes was quantified. Using atomistic molecular dynamics (MD), aqueous cesium dodecyl sulphate (CsDS) surfactants adsorbed on (6,6), (12,12), and (20,20) single-walled carbon nanotubes (SWNTs) were simulated at ambient conditions. When compared to results for sodium dodecyl sulphate (SDS), the results suggest that Cs^+ ions, compared to Na^+ , yield a more compact coverage of the nanotubes at the surfactant surface coverage of 4.0 molecules/nm² ($\cong 0.25$ nm²/headgroup), with the surfactant heads extended towards the bulk aqueous solution, and prevent water from accessing the nanotube surface. These morphological results, which are in qualitative agreement with experimental data, suggest that CsDS should be more effective than SDS at stabilising aqueous carbon nanotubes dispersions. More importantly, these results were obtained only for the (6,6) nanotubes simulated. For the wider nanotubes the simulations show limited, if any, differences in the morphology of the surfactant aggregates when the Na^+ ions are substituted with Cs^+ ones. The different salt-specific behaviour observed for the surfactants adsorbed on narrow versus wide carbon nanotubes could be exploited for the selective stabilisation of mono-dispersed carbon nanotube samples.

5.2 Introduction

Due to strong van der Waals interactions [109], single-walled carbon nanotubes (SWNTs) tend to agglomerate in aqueous media, which limits their utilization [10,150,151]. Many surfactants [24-39] have been used to stabilise aqueous SWNTs dispersions, and some of them show pronounced selectivity towards stabilising SWNTs of given diameter, and sometimes chirality [36,37]. In general, it is expected that the hydrophobic interactions between surfactant tails and nanotube surfaces facilitates surfactant adsorption, while the hydrophilic surfactant heads, hydrated, provide effective nanotube-nanotube repulsion [40]. For example, McDonald *et al.* [28] demonstrated that some surfactants [e.g., sodium dodecyl benzenesulfonate (SDBS) and sodium chlorate (SC)] are better than others [e.g., sodium dodecyl sulphate (SDS)] at stabilising SWNTs dispersions; Duque *et al.* [45] suggested that SWNTs with narrow diameter are more easily stabilised than wider ones; Wang and collaborators [40,132] showed that, in the case of Triton X-100, the quality of SWNTs dispersions is optimal at bulk surfactant concentrations comparable to, or slightly smaller than the critical micelle concentration; Rativ-Roth *et al.* [152] found isotropic dispersions of SWNTs in solutions of spherical micelles of the ionic cetyltrimethylammonium bromide (CTAB) surfactants by cryogenic-temperature transmission electron microscopy (Cryo-TEM).

Mastering a reliable molecular-level understanding to explain such observations will allow the design of new surfactants, or surfactant formulations, to sort carbon nanotubes in samples mono-dispersed in diameter and maybe chirality. To achieve such goals a number of simulation studies conducted both at the atomistic [42,43,140] or at the coarse-grained levels [119,120] contributed to a detailed understanding of the morphology of surfactant aggregates self-assembled on SWNTs, and how such structures change when two SWNTs approach each other, yielding an effective SWNT-SWNT potential of mean force.

The present study stems from recent experimental observations briefly reported in an interesting article by Duque *et al.* [45], who employed density gradient ultracentrifugation and fluorescence spectroscopy to study SWNT dispersions stabilised

using SDS surfactants. Among other interesting observations, Duque *et al.* reported that when aliquots of cesium (Cs^+) ions were added to aqueous SDS-SWNT dispersions, the correlations between SWNTs and water significantly diminished, suggesting a reorganisation of the self-assembled surfactant aggregates adsorbed on the SWNTs. The results were found to be more pronounced for small- than for large-diameter SWNTs. Significant reorganisation of self-assembled SDS aggregates upon replacement of Na^+ with Cs^+ ions was also reported by Tummala and Striolo [46], who conducted molecular dynamics (MD) simulations for aqueous SDS on graphite.

In this chapter equilibrium all-atom MD simulation results for the morphology of self-assembled CsDS surfactant aggregates on SWNTs are reported. Different surfactant surface coverages on (6,6), (12,12), and (20,20) SWNTs are considered. All simulations are conducted at ambient conditions. The results are compared to those for aqueous SDS surfactants on SWNTs [41].

5.3 Methodology

5.3.1 Computational model

The simulation package GROMACS, version 4.0.7 [122], was employed to study the aggregate morphology of aqueous CsDS surfactants at contact with SWNTs. Three SWNTs, (6,6), (12,12) and (20,20), with diameters of 0.814, 1.628, and 2.713 nm, respectively, were considered. The diameters are obtained as the centre-to-centre distance between carbon atoms. The SWNTs were empty, and effectively treated as infinitely long because of periodic boundary conditions. Water molecules, ions, and surfactants were not allowed to enter the SWNTs.

Within SWNTs, the carbon atoms were treated as uncharged Lennard-Jones (LJ) spheres and maintained fixed throughout the course of the simulations. The LJ parameters used to describe carbon-carbon interactions were those of Cheng and Steele [82]. Water molecules were modelled using the simple point charge extended (SPC/E) model [91]. SDS and CsDS molecules were assumed to completely dissociate into dodecyl sulphate

ion and Na^+ or Cs^+ counterion. The parameters for dodecyl sulphate ion were borrowed from those for SDS as described in Ref. [22] and [23]. Cs^+ ions were modeled as proposed by Smith and Dang [90], although ion polarizability was not considered. Other details regarding the force field used in the simulations are reported in Ref. [32].

The equations of motion were integrated with a time step of 0.002 ps using the leap-frog algorithm [33,153]. The simulations were conducted within the canonical ensemble in which the number of particles (N), the simulation box volume (V), and the temperature (T) were kept constant. All simulations were carried out at 300 K using the Nose-Hoover thermostat with a relaxation time constant of 0.1 ps [123]. The long-range electrostatic interactions were handled with the particle mesh Ewald method with a precision 10^{-4} [154]. The van der Waals interactions were treated with a switching cut-off starting at 8 Å and ending at 10 Å. The trajectories and velocities were saved every 1000 steps (2 ps) for subsequent analysis.

5.3.2 Simulated system

One SWNT was maintained at the centre of one simulation box of dimensions $7.00 \times 7.00 \times 6.15 \text{ nm}^3$. The cylindrical axis of the SWNT was aligned along the Z direction of the simulation box and maintained fixed during the simulations. To construct the initial configuration for the systems containing CsDS water and SWNTs, the final configurations obtained from the prior simulations for the correspondent SDS systems were used [41], but the sodium (Na^+) ions were substituted by Cs^+ ions. When configurations for the SDS systems were not available [i.e., 2.3 molecules/ nm^2 ($\cong 0.44 \text{ nm}^2/\text{headgroup}$) and 4.0 molecules/ nm^2 ($\cong 0.25 \text{ nm}^2/\text{headgroup}$) on (12,12) and (20,20) SWNTs], initial configurations were generated by first setting the nanotube at the centre of the simulation box and then inserting dodecyl sulphate surfactants perpendicularly to the nanotube axis. The Cs^+ and Na^+ ions were randomly placed in the simulation box. The number of water molecules in the box was adjusted to reproduce bulk liquid water density at ambient conditions. Periodic boundary conditions were applied in X , Y , and Z dimensions.

All simulations for CsDS and SDS surfactants on (6,6) SWNTs were conducted for 100 ns. In case of SDS surfactants, final configurations from the previous work were employed [41] and further increased the simulation time to 100 ns. For surfactants on (12,12) and (20,20) SWNTs, the systems were equilibrated for 200 ns. Each system was considered equilibrated because the results did not change during the last 40 ns of the simulations. The trajectories from last 20 ns were used for data analysis. Details regarding the composition of each simulated systems, including the SWNTs type, the total numbers of CsDS and water molecules, and nominal surfactant surface coverages are reported in **Table 5-1**.

Table 5-1: Simulation details for the systems considered

SWNT	No. of CsDS [molecules]	Nominal CsDS surface coverage [molecules per nm ²]
(6,6)	19	1.0
	36	2.3
	64	4.0
(12,12)	71	2.3
	126	4.0
(20,20)	119	2.3
	210	4.0

5.4 Results and discussion

Because fluorescence spectroscopy results are sensitive to the contact between water and carbon nanotubes, the discussion of the simulation results is begun from the analysis of radial water density profiles near the three simulated nanotubes as the density of the surfactants is changed. For brevity, only the density profile of the oxygen atoms of water is reported. The comparison of radial water density profiles away from the SWNT surfaces is shown in **Figure 5-1**. In this figure the position of one water molecule is identified by that of its oxygen atom. The feature of note is the reduction of water density in proximity of the nanotube surface when Na⁺ ions are substituted with the larger Cs⁺ ions. The effect is manifested in the density peak at $r \sim 3.5 \text{ \AA}$, and it is obviously seen at the surfactant surface coverage of 4.0 molecules/nm² ($\cong 0.25$

nm²/headgroup) on the (6,6) SWNTs (**Figure 5-1f**). On (12,12) and (20,20) SWNTs the results indicate that the water density near the nanotubes does not depend on the nature of the counterion (**Figure 5-1b** and **Figure 5-1c**, respectively). The main reason appears to be the fact that, at the surfactant coverage considered in the simulations, water molecules are not at contact with the SWNT surfaces even when Na⁺ is the counterion.

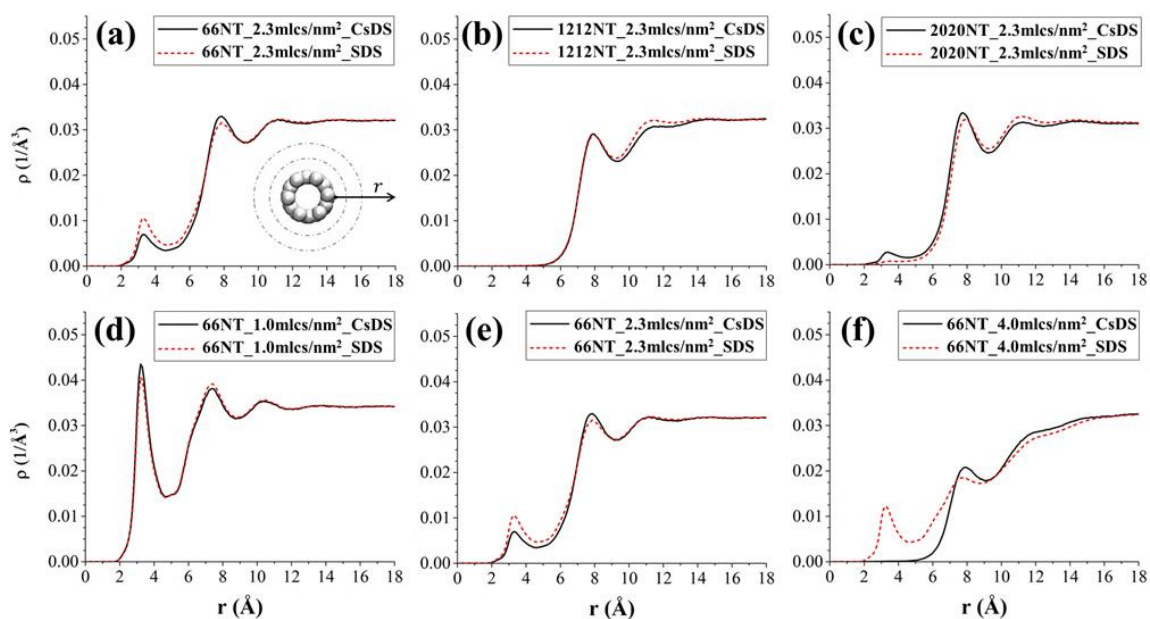


Figure 5-1: Radial density distributions of the oxygen atoms of water near SWNTs (the distance r is measured from the centre of the carbon atoms on the nanotube surface) in the presence of either aqueous CsDS (black-solid line) or SDS surfactants (red-dashed line). In panels (a), (b), and (c) the nominal surfactant per surface area is 2.3 molecules on (6,6), (12,12) and (20,20) SWNTs, respectively. In panels (d), (e), and (f) the nominal surfactant per surface area is 1.0, 2.3, and 4.0 molecules on (6,6) SWNTs, respectively.

To inspect the effect of surfactant coverage on interactions between water molecules and the nanotube surfaces, the density distributions of water molecules away from (6,6) SWNTs were compared when the number of surfactants adsorbed on the nanotubes was changed. The nominal surface coverages: 1.0, 2.3, and 4.0 molecules per nm² (\cong 0.98, 0.44, and 0.25 nm²/headgroup, respectively) were considered (**Figure 5-1d**, **Figure 5-1e**, and **Figure 5-1f**, respectively). Note that the surface coverage is expressed as ‘nominal’ surfactant molecules per surface area. The reason is that, especially at the

largest surfactant densities simulated, it is possible that some surfactants either form small micelles that desorb from the nanotube surfaces or desorb from the nanotube surfaces and from micelles. Such structures will be evident in the analysis of the equilibrated simulation snapshots, discussed in **Figure 5-2** and **Figure 5-3**. The effective surfactant molecules per surface area correspondent to each simulated system are reported as Appendix B.

At low surface coverage (1.0 molecules/nm²), a density peak of high intensity at $r \sim 3.5$ Å is observed for both CsDS and SDS simulations, suggesting that the amount of surfactant available on the nanotube surfaces is too low to prevent water from being in contact with the SWNTs. As the surface coverage increases, the density peak intensity significantly decreases, suggesting that smaller amounts of water molecules can be found near the nanotube surfaces. At the highest surface coverage considered (4.0 molecules/nm²), CsDS surfactants are extremely effective at shielding the (6,6) SWNT from being at contact with water, as demonstrated by the disappearance of the density peak at $r \sim 3.5$ Å.

The results discussed in **Figure 5-1** are likely due to the structure of the self-assembled surfactant aggregates on the various nanotubes. To visualise such structures, representative simulation snapshots of CsDS surfactants adsorbed on SWNTs are shown in **Figure 5-2** and **Figure 5-3**. The panels in **Figure 5-2** and **Figure 5-3** are organised following the formalism adopted in **Figure 5-1**, although only Cs⁺ is considered as counterion. A common feature shared by **Figure 5-2a**, **Figure 5-2b**, and **Figure 5-2c** is a monolayer of CsDS surfactants wrapped around the (6,6), (12,12), and (20,20) SWNTs, respectively. The tail segments are positioned near the SWNT surface, because of hydrophobic attractions between surfactant tails and the SWNT surface, and most surfactant headgroups project into water. In the case of (20,20) SWNTs some CsDS surfactants desorb from the nanotube and yield a few aggregates dispersed in water.

Because of the observed desorption of a few surfactants, nominal and effective surfactant coverages differ. To quantify the effective surface coverages of CsDS surfactants on the SWNTs the time-average number of surfactants adsorbed on the

SWNT was calculated by integrating the number density profiles of the surfactant molecules around the SWNT to a radial cut-off distance of 10 Å. At the nominal surface coverage of 2.3 molecules per nm², the effective surfactant surface coverage on (20,20) SWNT is reduced to 1.6 molecules/nm². For completeness, it should be pointing out that CsDS micelles are also observed in solution at the surface coverage of 4.0 molecules/nm² on both (12,12) and (20,20) SWNTs (**Figure B-2** in Appendix B). The effective surfactant surface coverages on (12,12) and (20,20) SWNTs are 2.7 and 2.4 molecules/nm², respectively, when the nominal surface coverage was 4.0 molecules/nm². Note that also

Finally, and perhaps more interestingly, the simulation snapshots of **Figure 5-2** and **Figure 5-3** suggest that the Cs⁺ ions are strongly associated with the negatively charged surfactant headgroups, probably because of electrostatic attractions. This behaviour has been observed in various simulation studies [41-43,46,54,117,140,155].

CsDS aggregates on (6,6) SWNTs at the nominal surface coverages of 1.0, 2.3, and 4.0 molecules/nm² are shown in **Figure 5-3a**, **Figure 5-3b**, and **Figure 5-3c**, respectively. The simulation snapshots reveal that CsDS surfactants yield a monolayer at the three conditions considered. However, at low coverage the sparse surfactants are parallel to the nanotube axis and yield a ring-like structure, while the aggregate becomes more disordered, with tails adsorbed on the nanotube surface and heads projected into the aqueous solution at high surface density. Note that neither double- nor multi-layered aggregates of CsDS surfactants are observed for CsDS in the systems considered here. On the contrary, at 4.0 molecules/nm² SDS surfactants were found to yield a continuous first layer at contact with the nanotube surface with excess SDS molecules agglomerate on top of the first layer yielding double-layered structures on (6,6) SWNTs, respectively, although those structures might have been due to local minima in the free-energy landscape. More details regarding the structure of the adsorbed self-assembled aggregates (e.g., the orientation probability distribution for CsDS on SWNTs) are presented as Appendix B.

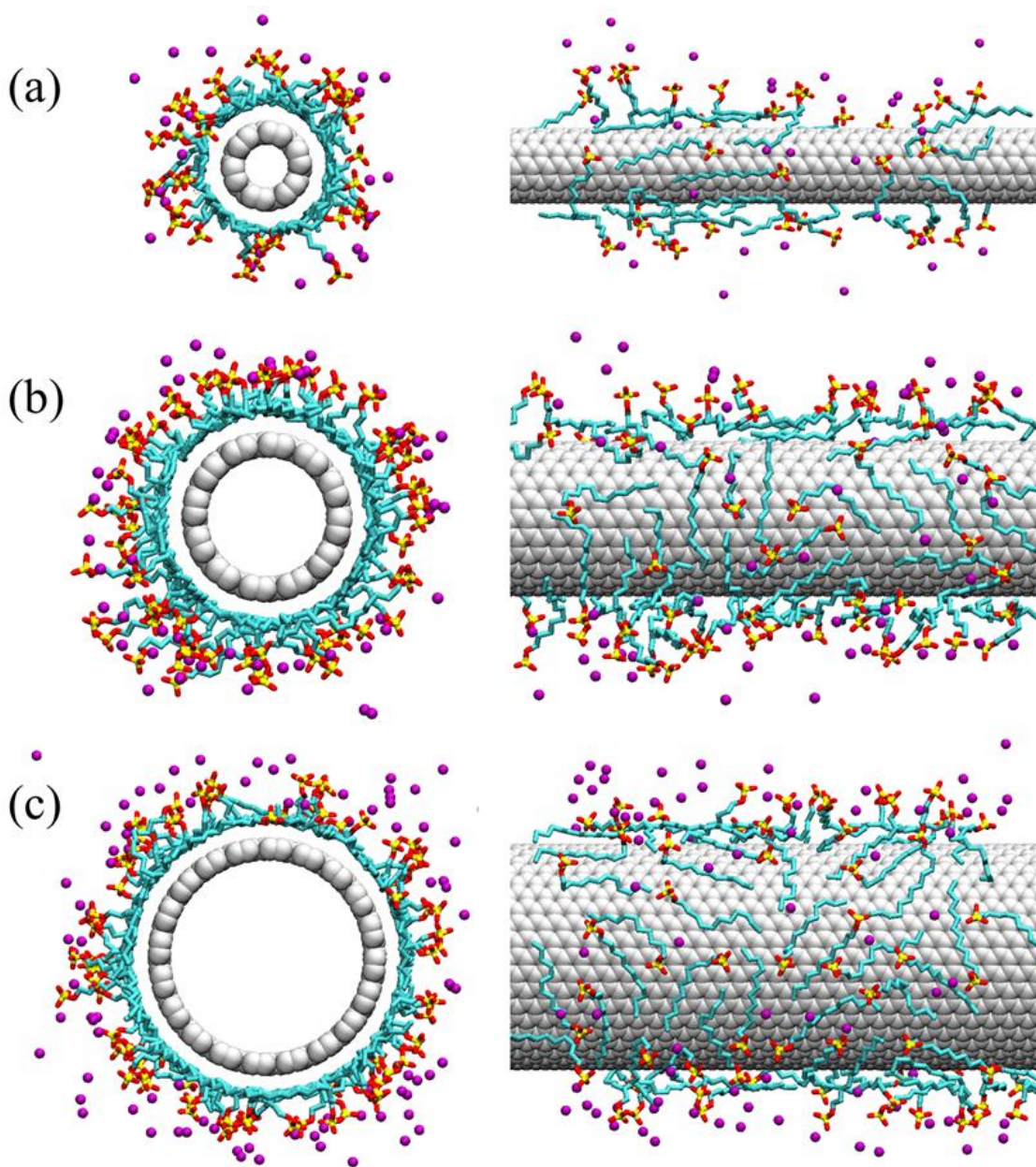


Figure 5-2: Front (left) and side (right) views of representative simulation snapshots for equilibrated CsDS surfactants adsorbed on SWNTs. In panels (a), (b), and (c) the nominal surfactant per surface area is 2.3 molecules on (6,6), (12,12), and (20,20) SWNTs, respectively. Purple spheres are Cs^+ ions, cyan spheres are either CH_2 or CH_3 groups in the surfactant tails, red and yellow spheres are oxygen and sulphur atoms in the CsDS surfactant headgroups. Note the formation of micelles desorbed from the nanotube in panel (c).

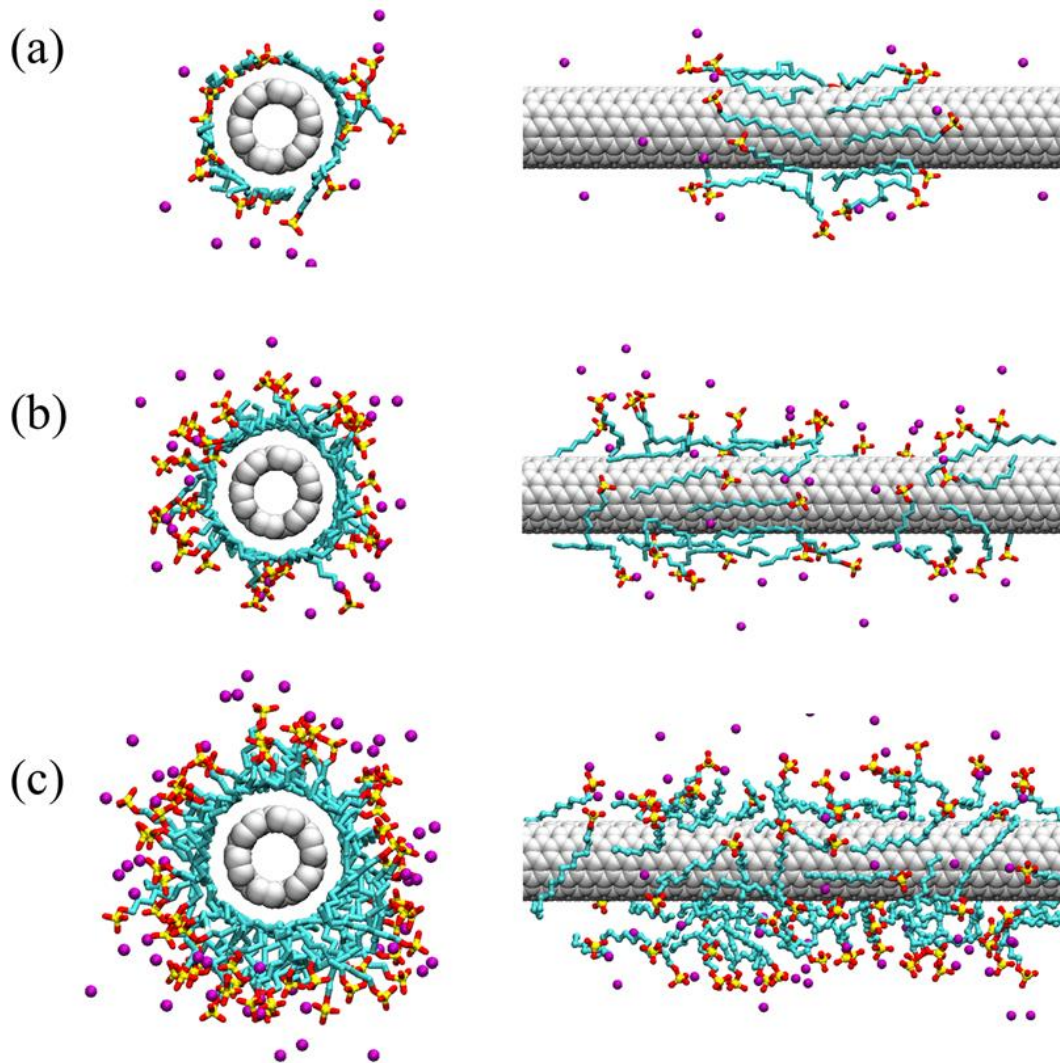


Figure 5-3: Front (left) and side (right) views of representative simulation snapshots for equilibrated CsDS surfactants adsorbed on (6,6) SWNTs. In panels (a), (b), and (c) the nominal surfactant per surface area is 1.0, 2.3, and 4.0 molecules, respectively. Water molecules are not shown for clarity. The color code is the same as that used in **Figure 5-2**.

The results obtained so far suggest that most differences on the morphology of the adsorbed surfactant aggregates as Na^+ ions are substituted with Cs^+ ones are observed on (6,6) SWNTs, and not so much on either (12,12) or (20,20) SWNTs. In what follows details the morphological differences among surfactant self-assembled aggregates, focusing on the (6,6) SWNTs, are characterised.

The main difference between Na^+ and Cs^+ ions is the diameter, and correspondingly the surface charge density. Because it has been observed before that for dodecyl sulphate surfactants the association of the counterions with the surfactant headgroups often determines the morphology of self-assembled aggregates [46], the radial density distributions of CsDS fragments near the (6,6) SWNTs (i.e., CH_2 and CH_3 tail segments, centre of mass of the sulphate group in the headgroups, and Cs^+ ions) were quantified, and the results are compared to those obtained for SDS on the same substrate. The results are shown in **Figure 5-4**. Radial density distributions for CsDS on (12,12) and (20,20) SWNTs do not show strong differences when compared to those obtained for SDS, as discussed in Appendix B (see **Figure B-3** and **Figure B-4**).

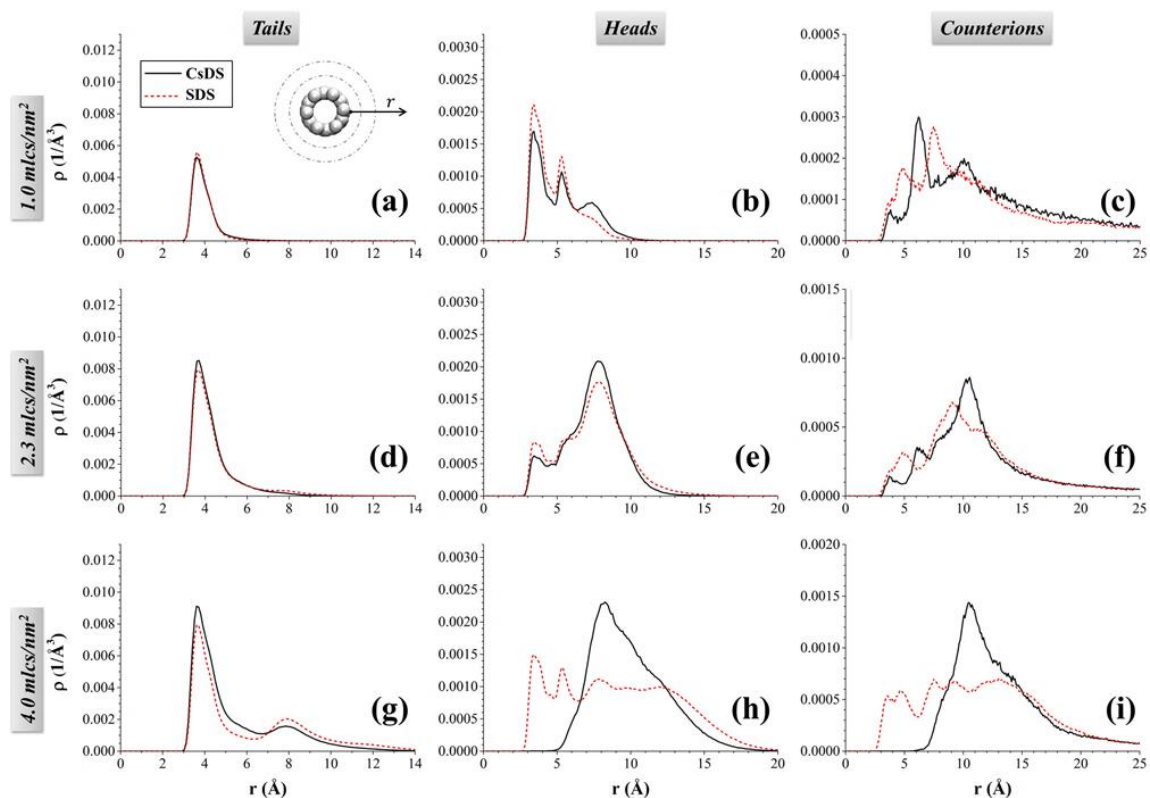


Figure 5-4: Radial density distributions of tail segments (left), surfactant headgroups (centre), and counterions (right) for SDS and CsDS surfactants adsorbed on (6,6) SWNTs. The nominal surfactant per surface area is 1.0 (top panels), 2.3 (middle panels), and 4.0 (bottom panels) molecules. Black-solid and red-dashed lines represent results obtained for CsDS and SDS surfactants, respectively.

At the nominal surface coverage of 1.0 molecules/nm², it is found that the tailgroups are strongly adsorbed on the (6,6) SWNT surfaces, yielding a strong peak at $r \sim 3.5 \text{ \AA}$ (**Figure 5-4a**). The radial density distributions for the tail groups do not seem to depend strongly on the counterion type at this low surfactant loading (results for SDS are very similar to those obtained for CsDS). As the surface coverage increases, the tail segments form a compact monolayer around the SWNTs both of CsDS and SDS. As the surface coverage increases further (**Figure 5-4g**), the second peak at $r \sim 8 \text{ \AA}$ is visible not only for SDS, but also for CsDS. In the case of SDS, double-layered structures were observed on the nanotube. Such structures, which however might be due to local minima of the free-energy landscape, are not visible in the case of CsDS, where the simulation snapshots suggest the formation of disordered mono-layered aggregates instead.

More pronounced is the reorganisation of the surfactant headgroups when the Na⁺ counterions are replaced by Cs⁺ ones (centre panels in **Figure 5-4**). The CsDS headgroups protrude into water, yielding a small shoulder at $r \sim 8 \text{ \AA}$ already at the smallest surface coverage considered (**Figure 5-4b**). As the surface coverage increases, the headgroups become more exposed to the aqueous solution both for CsDS and SDS (**Figure 5-4e**). The protruded CsDS headgroups are obviously seen at nominal surface coverage of 4.0 surfactant molecules per nm², resulting in the strong radial density peaks at $r \sim 8 \text{ \AA}$. In the case of SDS, the curve is broad due to double-layered structures (**Figure 5-4h**).

Note also that in correspondence to the formation of these pronounced density peaks at rather large radial distances, the density of headgroups at contact with the carbon nanotube surfaces is much lower in the case of CsDS than in the case of SDS. This observation is clearly related to the radial density distribution for water molecules, discussed in **Figure 5-1**. Namely, as the large Cs⁺ ions pull the surfactant headgroups away from the nanotube surfaces, water molecules cannot interact favourably with the carbon nanotube surfaces, and are expelled from the interfacial, contact region. On the contrary, in the presence of SDS the surfactant headgroups remain close to the nanotube surfaces even at the highest surface coverage considered. As in the case of the rearrangement of dodecyl sulphate surfactants self-assembled on graphite as a function

of counterion type[46], the results just discussed are only due to steric effects due to the strong tendency of counterions and surfactant headgroups to self-associate.

The differences observed for the headgroup radial density profiles when either Na^+ or Cs^+ ions were used in the simulations were explained in terms of association with between the headgroups and the ions. It is therefore expected to observe the Cs^+ ions located, on average, further from the (6,6) SWNT surfaces than the Na^+ ions are, at otherwise equal conditions. The radial density profiles for the counterions at increasing nominal surface density are shown in **Figure 5-4c**, **Figure 5-4f**, and **Figure 5-4i**. The results follow, qualitatively, the expectations. The counterions accumulate near the surfactant headgroups, and their density decreases as the radial distance from the nanotube surface increases. In general, the Na^+ ions are found closer to the SWNT surfaces than the Cs^+ ions are. The largest differences between radial density profiles observed for Na^+ or Cs^+ ions are obtained at the largest surfactant surface density considered (**Figure 5-4i**), in which case some Na^+ ions are found at contact with the nanotube despite the large surfactant concentration, while the Cs^+ ions are not found at contact with the nanotube surface. As already mentioned, these results are consistent with the radial density distribution of water molecules (**Figure 5-1**) and also with the explanation proposed for the different morphology observed for CsDS and SDS self-assembled aggregates.

For completeness, it should be pointed out that the simulations for both CsDS and SDS surfactants on (6,6) SWNTs discussed in **Figure 5-4** were equilibrated up to 100 ns, longer than those reported previously [41]. Because of the extended simulation time, multi-layered structures observed previously on the (6,6) SWNTs for SDS surfactants at 2.3 and 4.0 molecules/nm² were not observed. It is possible that those structures were representative of local minima on the free energy landscape. Despite the lack of such multi-layered structures, the results show pronounced differences in the structure of the adsorbed surfactants when Na^+ ions are substituted with Cs^+ ones. Additional simulation snapshots for SDS surfactants on (6,6) SWNTs are presented in Appendix B. It should also be pointed out that radial density profiles calculated for tailgroups, headgroups, and counter ions for CsDS on (12,12) and (20,20) SWNTs did not differ substantially

compared to those obtained for SDS at the three surface coverages considered in this work. These results are provided in Appendix B.

5.5 Conclusions

In summary, using all-atom molecular dynamics simulations, it showed that the morphology of dodecyl sulphate surfactants self-assembled on carbon nanotubes can be strongly dependent on the counterion type. This work compares Cs^+ to Na^+ ions. As discussed previously, SDS surfactants yield rather disordered aggregates on (6,6), (12,12), and (20,20) SWNTs. Water molecules can swell these aggregates, and it is often found at contact with the nanotube surface, even at large surfactant surface densities. In this work it showed that when Na^+ ions are substituted with Cs^+ ones the self-assembled surfactant aggregate morphology changes significantly in the presence of narrow carbon nanotubes. On (6,6) SWNTs the CsDS surfactants tend to yield adsorbed monolayers in which the surfactant tails are at contact with the nanotube surfaces, as in the case of SDS, but most of the surfactant headgroups are projected into water. Using density profiles it can be proposed that these morphological changes are due primarily to the association between the surfactant headgroups and the counterions. As a result of the more compact and to some extent more regular self-assembled surfactant aggregates, water molecules are found not to swell the surfactant aggregates, and in some cases not to come in contact with the carbon nanotube surfaces. These results are in qualitative with the experimental fluorescence spectroscopy observations reported by Duque et al [45].

Chapter 6 Self-Assembled Surfactants on Patterned Surfaces: Confinement and Cooperative Effects on Aggregate Morphology

The material presented in this chapter was published in 2014, volume 16, pages 16388–16398 of *Physical Chemistry Chemical Physics*.

6.1 Chapter overview

The adsorption and self-assembly of surfactants are ubiquitous processes in several technological applications, including the manufacture of nano-structured materials using bottom-up strategies. Although much is known about the adsorption of surfactants on homogeneous flat surfaces from experiments, theory, and simulations, limited information is available, in quantifiable terms, regarding the adsorption of surfactants on surfaces with chemical and/or morphological heterogeneity. In an effort to fill this knowledge gap, results obtained using equilibrium dissipative particle dynamics (DPD) simulations for the adsorption of model surfactants onto patterned flat surfaces (i.e., flat surfaces with chemical heterogeneity) are reported. The patterns consist of one or two stripes of variable width on which the surfactants could adsorb. The adsorbing stripes are surrounded by a surface that effectively repels the surfactants. This repelling surface, perhaps not realistic, allows quantifying the effect of lateral confinement on the morphology of surfactant aggregates. When the stripe width is large (effectively providing a homogeneous flat surface), the surfactants yield a flat monolayer. The simulations suggest that the flat monolayers become hemi-cylinders, hemi-spheres, and individual surfactants as the stripe width decreases, a consequence of lateral confinement. In some cases the simulations show evidence of cooperative effects when two adsorbing stripes are present on the surfaces. If the distance between the stripes and the widths of the stripes are both less than about one surfactant length, hemi-cylindrical shells and irregular structures are observed because of cooperativity; otherwise the results match those found for a single isolated stripe. The predictions could be useful for the design of new nano-structured materials and coatings, for applications ranging from nano-fluidic devices to nano-reactors.

6.2 Introduction

The widespread interest in the self-assembly of surfactants on solid surfaces is motivated by many industrial processes [61,156-161]. To describe surfactant self-assembly, the relationship between surfactant properties, surface characteristics, and adsorption thermodynamics must be understood. Many interesting experimental [162-167] and computational [168-176] results concerning surfactant adsorption on flat homogeneous surfaces have been reported in the literature. However, very little has been carefully quantified regarding surfactant adsorption on heterogeneous surfaces. Fundamental questions that might lead to important innovations include, but are not limited to: what is the effect of chemical surface heterogeneity on the amount of surfactants adsorbed? Are the morphologies of surfactant aggregates self-assembled on heterogeneous surfaces different compared to those obtained on flat homogeneous surfaces? And, ultimately, how can surfactant aggregates be manipulated by patterning a surface?

Surface heterogeneity can be caused by geometrical structures (e.g., surface roughness, shapes and sizes of surface features) and varying chemical composition (e.g., lattice defects, surface functional groups, and impurities). At the atomic scale geometrical heterogeneity must be associated with chemical heterogeneity, but chemical heterogeneity can in principle occur without geometrical heterogeneity (i.e., flat surfaces can be characterised by different chemical properties). Some experimental data suggest that surface heterogeneity can lead to rich surfactant behaviour. For example, Foisner *et al.* [177] found that self-assembled monolayers of octadecyltrichlorosilane (OTS) on modified silicon surfaces change to circular island structures when the surface is hydrophobized. Schniepp *et al.* [58,178] showed that the orientation of sodium dodecylsulphate (SDS) surfactants on Au(111) surfaces strongly depends on surface roughness. Wu *et al.* [179] reported that surface roughness affects the amount of cetyltrimethylammonium bromide (CTAB) surfactant adsorbed on gold, as well as the visco-elastic properties of the self-assembled aggregates.

From a theory and simulation point of view, a few authors addressed the adsorption of surfactants on heterogeneous surfaces. Using lattice Monte Carlo (MC) simulations,

Reimer *et al.* [180] investigated the adsorption of surfactants on surfaces in which a hydrophobic (hydrophilic) domain was surrounded by a hydrophilic (hydrophobic) surface, as well as on checkerboard hydrophobic-hydrophilic surfaces. They found that the dimension of the surface patterns influences the adsorption behaviour of surfactants. Zhang *et al.* [181] showed that the surfactant aggregates formed on heterogeneous (checkerboard and striped) surfaces are sufficiently dependent on the surface features that they could be used for surface-recognition purposes. Striolo [182] reported that surfactant adsorption can be problematic when the size of the adsorbing square patch on a surface is less than a surfactant-dependent threshold. Tummala *et al.* [183] conducted molecular dynamics (MD) simulations to investigate the morphology of SDS surfactants on graphene nano-sheets, suggesting that the size of the graphene supports has a strong effect on the surfactants morphology, because of lateral-confinement effects. In the prior work, the adsorption of several aqueous surfactants on various carbon nanotubes was investigated, and it was found that the nanotube diameter strongly influences the morphology of the aggregates, via a sort of lateral-confinement effect due to the cylindrical shape of the nanotubes.

The adsorption of surfactants on flat, chemically heterogeneous surfaces is investigated. Surfactant adsorption is allowed on stripes (considered hydrophobic) surrounded by a surface that is energetically repulsive enough to prohibit surfactant adsorption if a surface is uniform in that energy. As the width of the hydrophobic stripe decreases, the degree of lateral confinement increases. The simulation results for the morphology of the surfactant self-assembled aggregates are reported. The simulations are conducted within the equilibrium dissipative particle dynamics (DPD) formalism. At the expense of representing the surfactants with atomistic precision, DPD allows the investigation of large systems for extended periods of time. For all simulations, a sufficient amount of surfactant is present to maintain concentrations above the critical micelle concentration in the bulk supernatant, which allows comparing surfactant aggregates obtained at comparable thermodynamic conditions.

6.3 Methodology

DPD simulations were carried out in the NVT ensemble using the package LAMMPS, as released on 14May12 [184]. Full details for the DPD methodology are provided elsewhere [93,94,185]. Simulations are conducted for aqueous surfactants near a flat solid surface. Each simulated system is comprised by five interaction beads, representing water, surfactant headgroup, surfactant tailgroup, hydrophobic surface sites, and surfactant-repelling surface sites.

A schematic representation of the coarse-grained model implemented here to represent water and surfactant molecules is provided in **Figure 6-1a**. Because The degree of coarse graining N_m was arbitrarily chosen as 5 (i.e., one DPD water bead represents five water molecules), the volume of one water bead is $\sim 150 \text{ \AA}^3$ [106]. The reduced density ρ was assigned as 5 beads/ r_c^3 , defined as the number of beads in a cubic volume of radius r_c . Accordingly, $r_c = 9.0856 \text{ \AA}$. As customary, the volume of each bead (150 \AA^3) in the simulation is maintained constant. Consequently, because the volume of one sodium dodecyl sulphate (SDS) molecule is $\sim 410 \text{ \AA}^3$ [186], one surfactant can be approximated with three DPD beads: one to represent the headgroup, and two to represent the tailgroups. The three beads are connected via harmonic bonds to yield a single chain. Because the van der Waals end-to-end length of one SDS molecule (L_S) is of 20.8 \AA [187], the equilibrium bond length r_0 was assigned as 10.4 \AA . As suggested by Denham *et al.* [188], the spring constant k_S was set as $100 k_B T / r_c^2$, which yields a 1.2% standard deviation for the bond length around r_0 . Note that, because electrostatic interactions are not explicitly taken into consideration in the simulations, the model is not intended to reproduce all physical properties observed for ionic surfactants. In particular, in the approach counterions are not modelled.

In each simulated system, two solid surfaces are positioned at $Z = 0 r_c$ and at $Z = 42 r_c$. For clarity, in the remainder of this chapter, X and Y directions are referred to as those parallel to the surface, while the Z direction is the one perpendicular to the surface. The solid surface at $Z = 42 r_c$ is repulsive to all surfactants. The one located at $Z = 0 r_c$ is the one on which surfactant adsorption is investigated. A schematic representation of the

solid surfaces is provided in **Figure 6-1b**. The surface is built with 14400 beads treated as rigid bodies. The surface beads are organised in a square lattice with nearest-neighbour distance $P = 0.35 r_c$ in X and Y directions. Four planes of solid beads are stacked on top of each other with interlayer distance $Q = 0.35 r_c$. Two consecutive planes are shifted with respect to each other by the shift distance $R = 0.175 r_c$ along both X and Y directions. Simulations were performed in a rectangular box of dimensions $21 \times 21 \times 42 r_c^3$, with periodic boundary conditions applied along X and Y directions. Selected simulations were repeated in boxes twice as large along X and Y directions, obtaining results consistent with those discussed in the text below.

In **Figure 6-1c**, the patterned surfaces, located at $Z = 0 r_c$, on which surfactants can adsorb are presented. These heterogeneous surfaces are composed by repelling and hydrophobic (adsorbing) beads. The hydrophobic beads are organised in stripes. Surfactant-repelling surface beads surround these hydrophobic stripes. To quantify lateral confinement and possible cooperative behaviour in the simulations, the stripe width L , and the shortest separation between parallel stripes, D were changed systematically. Note that surfactant-repelling surfaces such as those simulated here are probably not realizable experimentally, especially when the surfactants are in water. Despite this short-coming, the model allows systematically investigating the effect of lateral confinement.

The simulations are intended to reproduce ambient conditions. Because DPD is a coarse-grained method, all simulation runs were conducted at the reduced temperature $k_B T = 1$. The random and dissipative parameters were set to $\sigma = 3$ and $\gamma = 4.5$, respectively [93]. The time step $\Delta t = 0.03 \tau$ was used to integrate the equations of motion. The simulation time scale τ was 5.2 ps, as estimated by fitting the self-diffusion coefficient of water from the simulations for bulk water at ambient conditions to experimental data. Each system was simulated for as long as $\sim 1.248 \mu\text{s}$. By quantifying variations in the amount of surfactants present in the bulk supernatant (as micelles) and adsorbed on the surface, it was found that equilibrium was established after $\sim 0.936 \mu\text{s}$. Once in 1000 steps, the configurations were saved for analysis.

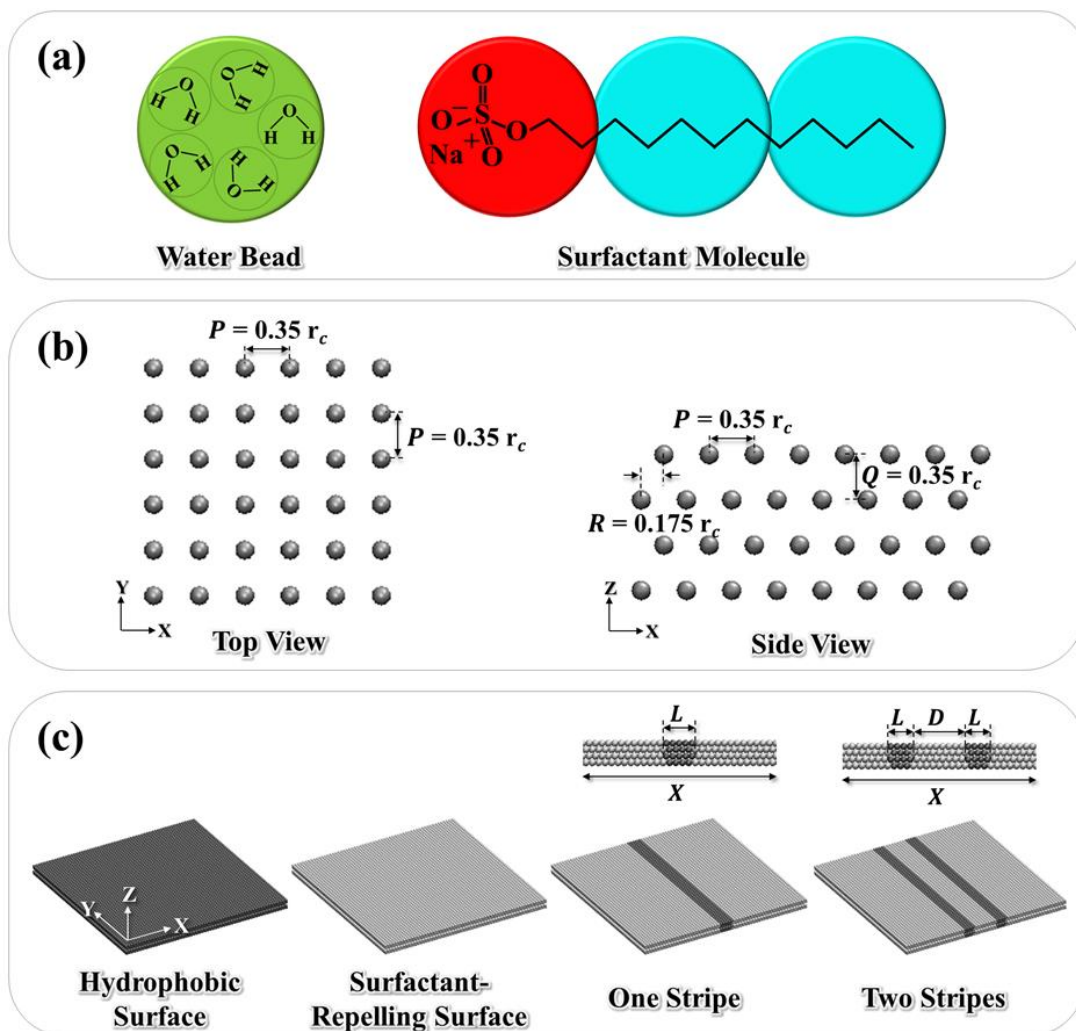


Figure 6-1: Schematic representation of (a) the coarse-grained beads used to represent water and surfactant molecules. The DPD water bead (green) represents five water molecules. The surfactant, which mimics SDS, contains one headgroup bead (red sphere) and two tail beads (cyan spheres). (b) Top (left panel) and side (right panel) views of the solid surface, highlighting the position of the rigid beads. The surface beads in each layer are arranged in a square lattice in which P is the nearest-neighbor distance along both X and Y directions. Q is the interlayer distance between planes of atoms within the solid. R is the shift distance between neighboring surface planes. (c) Patterned flat surfaces employed in this study. The hydrophobic and the surfactant-repelling surfaces are shown as dark and light grey, respectively. L is the stripe width. D is the shortest separation distance between two stripes.

As the DPD method is based on soft interactions, the repulsion parameters that need to be chosen include intra-species a_{ii} and inter-species a_{ij} values. Following the protocol proposed by Groot and Warren [93], a_{ii} was derived from the compressibility of water ($a_{ii} = 75k_B T/\rho$). Because the simulation density was $\rho = 5$ beads/ r_c^3 and $k_B T = 1$, $a_{ii} = 15$. The water-surfactant a_{ij} parameters were borrowed from Kuo *et al.* [189]. However, note that the surfactant simulated here was composed by one head and two tail beads, while Kuo *et al.* represented sodium tetradecyl sulphate with only one head and one tail bead.

The choice of interaction parameters between water and surfactant molecules was validated by performing a series of bulk simulations to estimate critical micelle concentration (CMC) and micelle size. The formation of the first micelle was observed at 7.77 mM. Within a range of surfactant concentrations (up to ~ 332 mM), the results for the micelle radius (~ 20.18 Å) were in general consistent with those reported in literature for SDS surfactants, both from experiments [190-192] and from simulations [193-195]. The CMC from the free surfactant concentration was not estimated, as proposed by Le Bard *et al.* [196]. Surprisingly, however, it was observed only few free surfactants in equilibrium with micelles. Sanders *et al.* [197] reported similar observations, from atomistic MD simulations, in systems of strongly associating surfactants. As the surfactant concentration was increased to 443 mM (~ 57 times the CMC) the formation of cylindrical micelles was observed.

The interactions between the surface beads and the surfactant tail beads were set to replicate tail-tail interactions when the surface bead is hydrophobic and water-tail interactions when the surface bead is repulsive. The interactions between the surface beads and the surfactant head beads were set to replicate tail-head interactions when the surface is hydrophobic and head-head interactions when the surface is repulsive. Implementing these parameters the formation of a surfactant monolayer was observed when a homogeneous hydrophobic surface was exposed to the aqueous surfactants. When the surfactant system was simulated on a homogeneous repelling surface, no surfactant adsorption was observed. Repeatedly, this situation (a surface completely

repelling surfactants) would be difficult to realise experimentally. In the latter case, all surfactants formed micelles in the bulk when the surfactant concentration is sufficiently high. Further details on the adsorption of surfactants on homogeneous surfaces are discussed in the next section. All interaction parameters implemented in this work are reported in **Table 6-1**.

The simulations were initiated with a surfactant concentration of 44.24 mM (370 surfactant molecules). During the course of the simulations, as some surfactants adsorbed on the surfaces, additional surfactants were added to the systems in order to maintain constant concentration in the bulk. Such conditions are representative experimentally of systems where the amount of surfactant adsorbed is small compared to the total amount of surfactant present in the system, such as in ellipsometry [198,199] or quartz crystal microbalance [167,179,200,201] experiments. The bulk concentration was maintained at $\sim 20\text{-}23$ mM ($\cong 3$ CMC). Some simulations were repeated at higher bulk concentration and yielded results similar to those presented below. Not surprisingly, simulation results below the CMC were however different, as the amount of surfactants adsorbed depends on the bulk surfactant concentration. The simulation results discussed herein were obtained from 68 individual simulations. The details for each of these simulations are provided in Appendix C.

Table 6-1: Repulsion parameters in $k_B T/r_c$ units for water (w), surfactant headgroup (h), surfactant tail (t), surfactant-repelling surface (rs), and hydrophobic (adsorbing) surface (as) beads

a_{ii} or a_{ij}	w	h	t	rs	as
w	15	0	81	15	81
h		15	69	15	69
T			15	81	15
rs				15	81
as					15

6.4 Results and discussion

6.4.1 Adsorption on homogeneous surfaces

Surfactant adsorption and self-assembly on the two homogeneous solid surfaces, one hydrophobic and one surfactant repelling was simulated. The initial surfactant concentration was varied in the range 110.73-221.46 mM (\cong 14.25-28.50 CMC), with all surfactants present in the bulk. On the hydrophobic surface, as expected, some surfactants adsorb as the simulation progresses, some form small aggregates in the bulk, and others remain as free monomers. Within a short period of time, however, the strong attractive interactions between the surfactant tail beads and the hydrophobic surface lead to complete adsorption. In **Figure 6-2a**, an example of surfactants adsorption on the hydrophobic surface at the initial surfactant concentration of 141.70 mM is reported. The hydrophobic surface is fully covered by surfactants at the surface coverage of ~ 3.03 surfactant molecule per nm^2 , yielding a flat monolayer. The surfactant tail groups are in contact with the hydrophobic surface, while the surfactant headgroups are exposed to water. The excess surfactants form a spherical micelle in the bulk, where the surfactant concentration is at 7.77 mM (\approx 1 CMC). The monolayer obtained in the simulations is expected, based on prior lattice Monte Carlo simulations for surfactants similar to those employed here [202]. Because electrostatic interactions are not explicitly taken into consideration in the simulations, the results relate to experimental observations for nonionic surfactants on hydrophobic surfaces [203,204].

In **Figure 6-2b** a representative equilibrium simulation snapshot for the self-assembled surfactants when the surface is effectively repulsive is reported. At the initial bulk concentration of 110.73 mM employed, a number of spherical micelles are observed, but no surfactant is found to adsorb on the surface, as desired. However, no or at most only a few free surfactants are found, which is not representative of actual behaviour, as briefly mentioned in the method section.

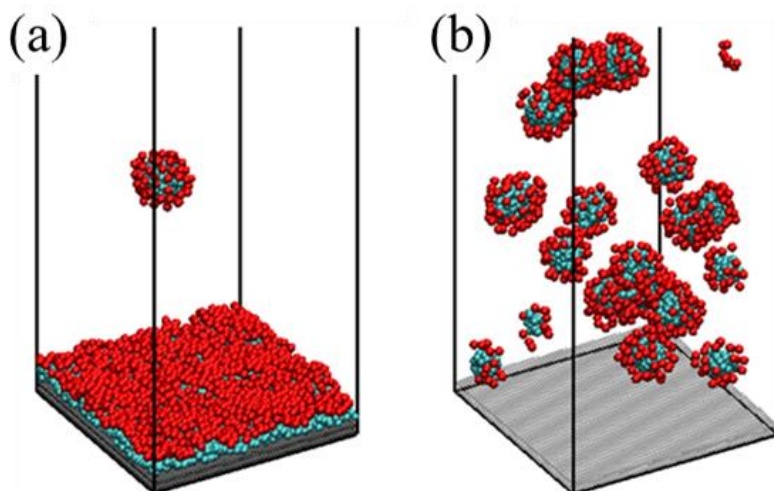


Figure 6-2: Representative simulation snapshots representing self-assembled surfactant aggregates on (a) the hydrophobic and (b) the surfactant-repelling surfaces. The simulations are conducted with initial surfactant concentrations of 141.70 and 110.73 mM, respectively. Surfactant head and tail groups are shown as red and cyan spheres, respectively. The hydrophobic and the surfactant-repelling surfaces are shown as dark and light grey, respectively. Water beads are not shown for clarity.

6.4.2 Lateral confinement: Effect of stripe widths

To quantify the effect of lateral confinement on the properties of surfactant self-assembled aggregates, surfactant adsorption on one individual hydrophobic stripe of variable width surrounded by repelling surface beads was simulated. By changing the stripe width the degree of lateral confinement can be manipulated, with narrow stripes yielding a more pronounced confinement than wide ones. The stripe width is indicated by L , expressed in units of the length of one surfactant molecule L_s . It is worth repeating that to maintain the thermodynamic conditions comparable throughout this study the surfactant concentration in the bulk, after adsorption has reached equilibrium, has been kept at around 20-23 mM ($\cong 3$ CMC). Representative simulation snapshots for surfactant aggregates adsorbed on one hydrophobic stripe of varying width are shown in **Figure 6-3**. From top to bottom the stripe width increases from $L = 0.15L_s$, to $L = 1.68L_s$. In the left and right panels a view perpendicular to the axis of the surface plane and a side view are provided, respectively. For clarity, water beads are not shown, nor

are the surfactants present in the bulk, not adsorbed on the surface. These results should be compared with the simulation snapshot shown in **Figure 6-2a**, where the morphology is a flat monolayer with no lateral confinement.

On the hydrophobic stripe of width $L = 0.15L_s$ (**Figure 6-3a**) the adsorption of one individual surfactant is sometimes observed. When this surfactant is adsorbed, its tail beads are in contact with the hydrophobic stripe, while the headgroup protrudes towards water. Note that no bond angle is used in the model, hence the head bead is free to adopt various angles with respect to the surfactant tail. Besides this computational detail, and more important for the scope of the present study is the observation that the single surfactant adsorbed on the narrow hydrophobic stripe frequently desorbs from it. Even increasing the surfactant concentration in the box to 110.73 mM does not yield a permanently adsorbed surfactant aggregate for this system. Although the adsorption of one surfactant is possible, the formation of an aggregate containing more than one surfactant is not allowed with such a narrow stripe. This behaviour is likely a consequence of the fact that advantageous tail-tail interactions between different surfactants cannot be established because the surrounding repelling surface prevents additional surfactants from adsorbing, and the surfactants adsorbed on the narrow hydrophobic stripe cannot adopt a conformation conducive to favourable tail-tail interactions.

The results obtained on the hydrophobic stripes of width $L = 0.31L_s$ and $L = 0.46L_s$ are shown in **Figure 6-3b** and **Figure 6-3c**, respectively. The main difference compared to the data shown in **Figure 6-3a** is the morphology of the self-assembled aggregate. On the narrowest stripe considered above one individual surfactant was found to adsorb, while on the stripes of width $L = 0.31L_s$ and $L = 0.46L_s$ the surfactants self-assemble yielding a hemi-sphere. As customary for such aggregates, the tail groups are found on the interior of the aggregate so they can be shielded from both water and the repelling surfaces. The surfactant headgroups are exposed to water, with some being positioned at the boundary between hydrophobic and repulsive surface beads. The self-assembled aggregates are found to easily migrate along the stripe. As the simulation progresses,

similarly to the results discussed regarding the stripe of width $L = 0.15L_s$, the results show that the surfactant aggregate can easily desorb from the stripe of width $L = 0.31L_s$. On the stripe of width $L = 0.46L_s$, however, once the aggregate forms on the surface, it does not desorb within the length of the simulations. The main driving force for surfactant adsorption is likely the attraction between surfactant tail groups and the hydrophobic stripe. The fact that the aggregates do not remain adsorbed for long times suggests that lateral confinement effectively reduces the effective attraction between the surfactants and the hydrophobic surface. The effective attraction is reduced compared to the homogeneous surface of **Figure 6-2a** because lateral confinement is so tight that it limits, to some extent, the cooperative tail-tail interactions. These interactions are still present, as demonstrated by the formation of the adsorbed micelles, but they cannot be as extensive as they are on a flat homogeneous hydrophobic surface. These observations seem to be in qualitative agreement with some experimental observations by Huang *et al.* [205], who found that the adsorption of proteins on gold nanoparticles can be influenced by the scale of surface heterogeneity on the nanoparticles.

As the stripe width increases and becomes wider than half of the surfactant length, the simulation results reveal that the self-assembled aggregates change morphology from being roughly hemi-spherical to becoming hemi-cylindrical. These structures are shown in **Figure 6-3d**, **Figure 6-3e** and **Figure 6-3f**, for stripe widths $L = 0.61L_s$, $1.07L_s$, and $1.68L_s$, respectively. Other than the different shape of the aggregates, one important difference between the aggregates observed on these stripes and those obtained on the stripes of width $L = 0.31L_s$ or less is that once these aggregates are formed desorption of the entire aggregate during the length of the simulations is not observed. The results are consistent with prior simulations by others, who reported stable surfactant adsorption when the size of either checkerboard or striped surfaces is commensurate with the self-assembled surfactant aggregates [181].

As expected for surfactant aggregates with the hemi-cylindrical morphology self-assembled on hydrophobic surfaces, analysis of the simulation results confirms that the surfactant tail groups are adsorbed on the hydrophobic stripe, and are for the most part

buried within the interiors of the hemi-cylindrical aggregate. The surfactant headgroups provide a shield that separates the hydrophobic core of the hemi-cylindrical aggregates from the surrounding water. The average orientation of the surfactant molecules within these aggregates is perpendicular to the long axis of the hydrophobic stripes, as this orientation permits the surfactants to minimise hydrophobic surface-water and tail-water contacts, as well as to maximise the tail-tail interactions. Visual inspection of the simulation snapshots, in particular of the left panels of **Figure 6-3** and shown close-up below in **Figure 6-4**, reveals that the surfactant headgroups are in some cases just above the repelling surface beads. This result was not expected, as the interactions between surfactant headgroups and the repelling surface beads are somewhat repulsive (see **Table 6-1**). The energetic advantage of allowing numerous tail-tail and tail-hydrophobic surface interactions is compensating for the energy penalty related to having a few headgroups in proximity of the repelling surface beads.

Comparing the snapshots in **Figure 6-4** (as well as those shown in **Figure 6-3d**, **Figure 6-3e**, and **Figure 6-3f**) it is found that the curvature of the hemi-cylindrical surfactant aggregates decreases as the stripe width increases. On the stripe of width $L = 0.61L_s$ (left panel), because the surfactant molecules cannot extend up to their length while adsorbed on the hydrophobic surface, a few of them align perpendicular to the surface, yielding a hemi-cylinder with large curvature. On the stripe of width $L = 1.07L_s$ (middle panel) the surfactant molecules preferentially orient themselves perpendicular to the direction of the long axis of the stripe, similarly to the results obtained for the stripe of width $L = 1.68L_s$ (right panel). On a much wider stripe, i.e., on a homogenous hydrophobic surface, the surfactants considered here yield a monolayer, as shown in **Figure 6-2a**. Combining all these sets of visual observations, the results suggest that lateral confinement effectively compresses the monolayer laterally, eventually making it bulge away from the surface. As the lateral confinement becomes of the order of the surfactants molecular length, the monolayer becomes a hemi-cylinder. When the lateral confinement is even more pronounced, the hemi-cylinder is no longer stable, and therefore desorbs, allowing some surfactants to adsorb as hemi-spheres, and eventually preventing aggregates from forming on the surface.

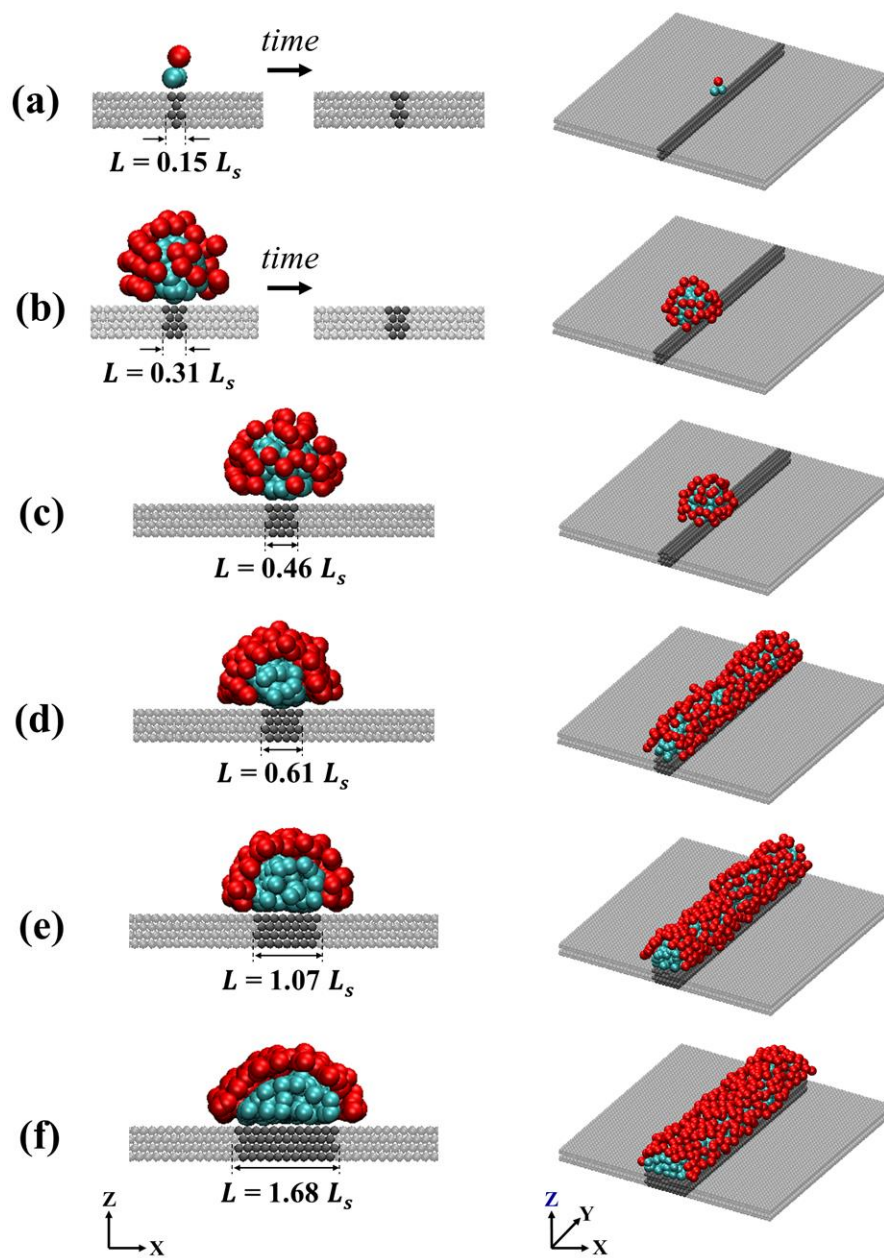


Figure 6-3: Surfactant aggregates self-assembled on one hydrophobic stripe of width $L =$ (a) $0.15L_s$; (b) $0.31L_s$; (c) $0.46L_s$; (d) $0.61L_s$; (e) $1.07L_s$; and (f) $1.68L_s$. Left and right panels are for a view perpendicular to the axis of the surface plane and a side view, respectively. Water beads are not shown for clarity. The colour code is the same as that used in **Figure 6-2**. Note that for systems shown in panels (a) and (b) the aggregates adsorb and desorb frequently from the hydrophobic stripe, as discussed in the text.

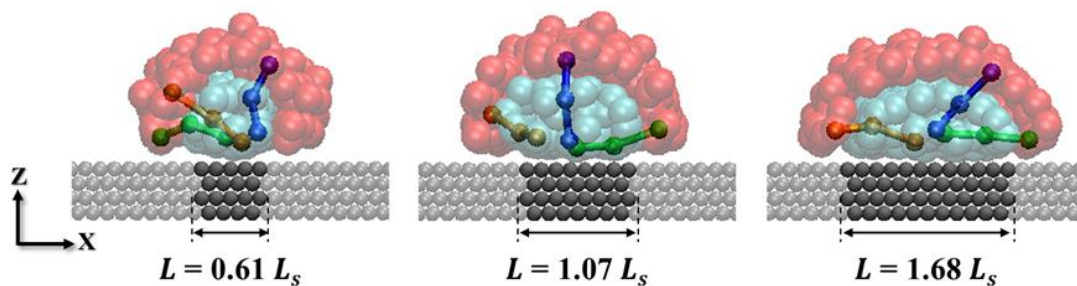


Figure 6-4: Close-up snapshots of surfactant aggregates self-assembled on hydrophobic stripes of width $L = 0.61L_s$, $1.07L_s$, and $1.68L_s$ (left to right panels, respectively). In this figure is shown a view perpendicular to the axis of the surface plane. Water beads are not shown for clarity. The colour code is the same as that used in **Figure 6-2**.

In-plane density profiles of surfactant tail groups, and surfactant headgroups within planes parallel (top panels) and perpendicular (bottom panels) to the surface were also calculated, as presented in **Figure 6-5** and **Figure 6-6**, respectively. From left to right the results are shown at increasing stripe width. Only stripes of width $L = 0.61L_s$ or wider are considered, as in the narrower stripes the aggregates are mobile and the density profiles would provide a misleading characterization.

The main observation from visual inspection of the results, shown in **Figure 6-5**, is that the surfactant tail groups are concentrated near the centre of the stripes. On the stripe of width $L = 0.61L_s$ the surfactant tail groups are effectively curved out at the position of the stripe edges. When the stripe width increases, the surfactant tail groups are less present at the boundary between hydrophobic stripe and repelling surface. In **Figure 6-6** the results confirm the analysis of the snapshots of **Figure 6-4**, in that the curvature of the hemi-cylindrical surfactant aggregates clearly decreases as the stripe width increases. The surfactant headgroups evidently accumulate above the repelling surface beads on the three stripes, especially in the case of the stripe of width $L = 0.61L_s$, most likely because assuming such conformation the surfactants benefit from advantageous tailgroup-hydrophobic surface interactions. On the stripe of width $L = 1.68L_s$, the surfactant headgroups spread, and near the center of the stripe yield a structure comparable to that of a monolayer. These effects are a manifestation of the lateral

confinement, as discussed above. The results in **Figure 6-5** and **Figure 6-6** are in qualitative analogy with the observation reported by Tummala *et al.* [183], who conducted atomistic MD simulations and reported that the size of a graphene sheet can strongly affect the morphology of a self-assembled SDS aggregate, presumably because of lateral confinement effects.

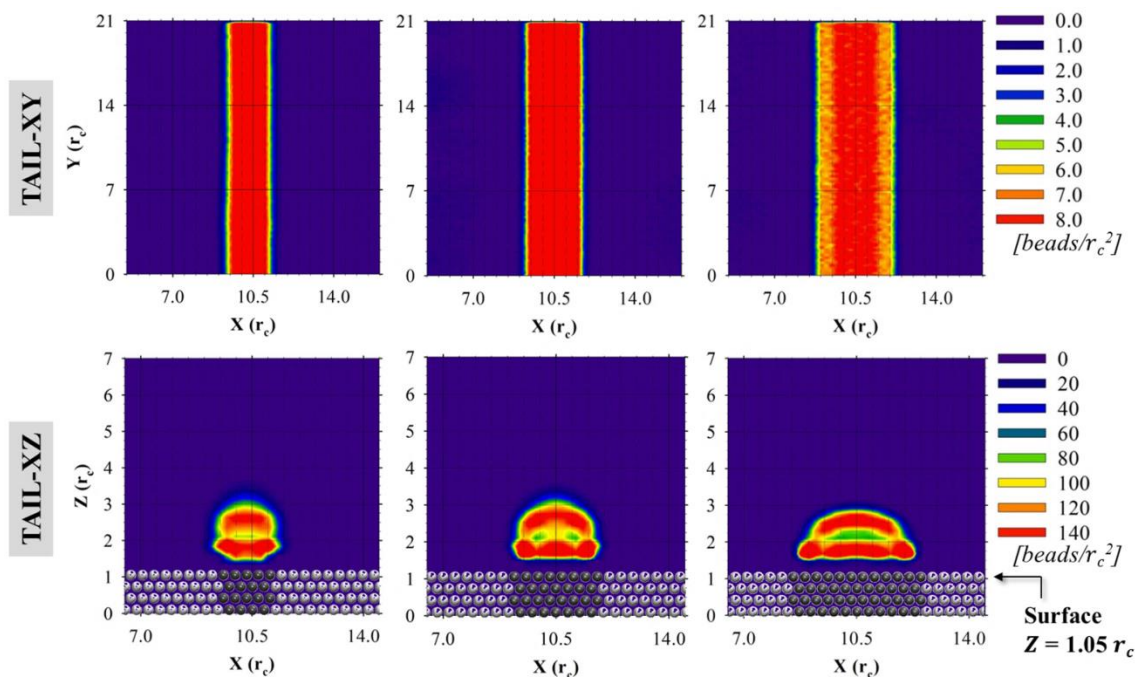


Figure 6-5: In-plane density distributions of surfactant tail groups adsorbed on one individual hydrophobic stripe. The results are obtained along planes parallel (top) and perpendicular (bottom) to the surface. Left to right panels are for stripes of width $L = 0.61L_S$, $1.07L_S$, and $1.68L_S$, respectively. Surface densities are expressed in number of beads per r_c^2 .

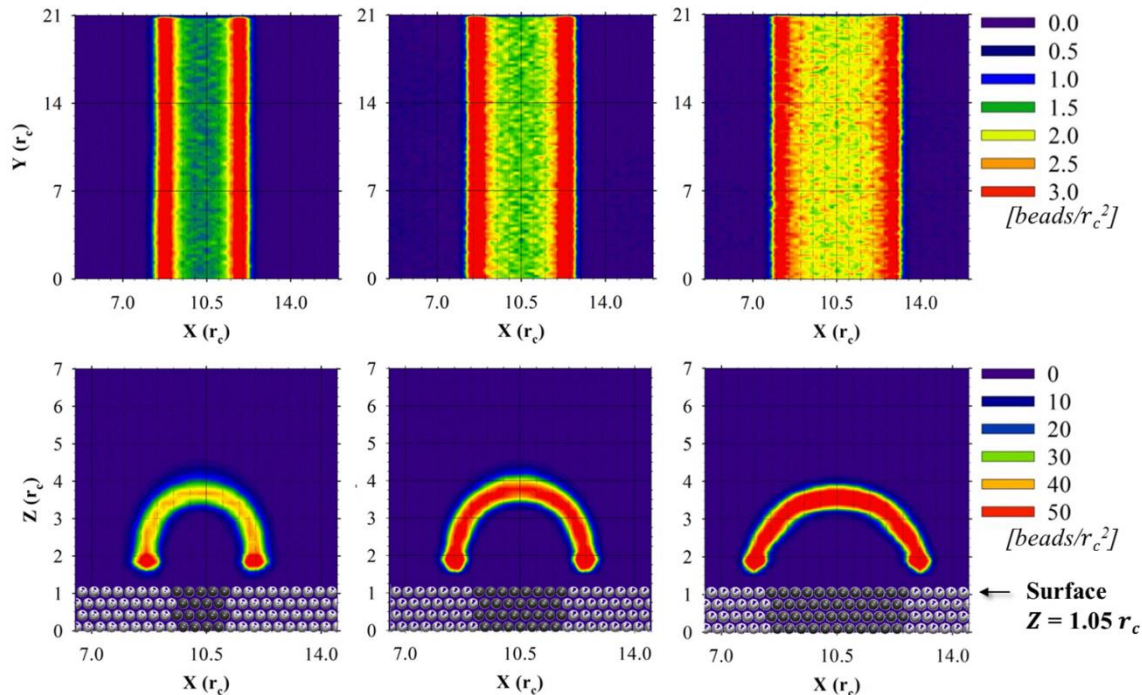


Figure 6-6: Same as **Figure 6-5** but for surfactant headgroups.

6.4.3 Cooperative effects: Adsorption on neighbouring stripes

Cooperative effects have been investigated by simulating the self-assembly of surfactants on two stripes, of variable width, at different separations from each other. The shortest separation between the two stripes is indicated by the symbol D , expressed in units of the length of one surfactant molecule, L_s . Representative simulation snapshots of surfactant aggregates adsorbed on two stripes separated by $D = 0.15L_s$ (top panels) and $0.46L_s$ (bottom panels) are provided in **Figure 6-7**. In all cases considered in this figure the hydrophobic stripes are of width $L = 0.46L_s$. From left and right a view perpendicular to the axis of the surface plane, a side view, and a close-up snapshot for the surfactant aggregates are presented, respectively. It should be noted that on an individual stripe of width $L = 0.46L_s$ the surfactants adsorb yielding hemi-spheres (see **Figure 6-3c**). When the two narrow stripes are separated but close to each other (all cases in **Figure 6-7**), the simulations reveal the formation of a roughly hemi-cylindrical shell. The surfactant tail groups are adsorbed on the hydrophobic stripe, and are

assembled into a monolayer that is curved in the middle so that the hydrophobic tails do not contact the repulsive surface. Within this shell the surfactant headgroups are exposed to water towards the outside of the hemi-cylinder, while some of the tail groups, in the center of the shell, are exposed to the surfactant-repelling surface in between the two hydrophobic stripes. The two parallel hydrophobic stripes essentially provide a support for this monolayer. The results show no evidence of water inside the hemi-cylinders. The self-assembled shells have the features just summarised for two reasons: (1) the surfactants are repelled by the surface separating the two hydrophobic stripes, and, perhaps more importantly, (2) bending of the monolayer allows for the formation of numerous tail-tail contacts at the expense of an elastic deformation of the monolayer (which was not quantified). By changing the molecular properties of the surfactants, the curvature of the hemi-cylindrical shell might be controlled, which could lead to advancements in manufacturing processes and surface modification techniques. Because the results show that the self-assembled surfactant monolayer effectively covers the repelling region that separates the two hydrophobic surfaces, the simulations appear to be consistent with the MC simulation results of Reimer *et al.* [173], who studied surfactant adsorption on checkerboard surfaces. Surfactant adsorption was enhanced when the attractive patches were sufficiently close on an otherwise repelling surface.

To further quantify the results just summarised, planar density distributions obtained for surfactant tail groups (top panels) and headgroups (bottom panels) as observed along planes perpendicular to the surface are presented in **Figure 6-8**. The left and right panels are the results obtained for the separation distance $D = 0.15L_s$ and $0.46L_s$, respectively. Confirming the visual inspection of the simulation snapshots of **Figure 6-7**, the density profiles show that the surfactant tail groups form a dense layer between the two neighbouring hydrophobic stripes, and the headgroups are exposed only to the outside of the hemi-cylinder. Next the effect of increasing D on the results just discussed is quantified.

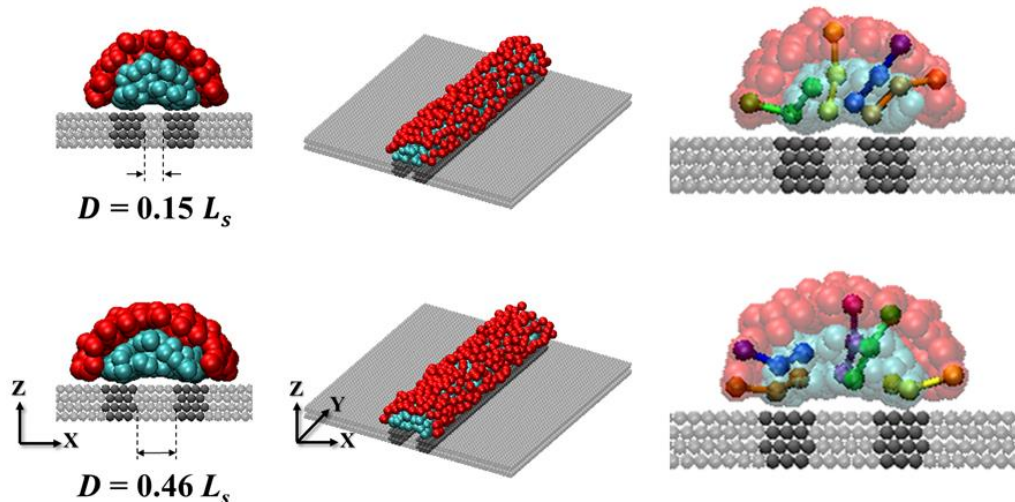


Figure 6-7: Representative simulation snapshots for surfactant aggregates self-assembled on two hydrophobic stripes located at minimum separation distance $D = 0.15L_s$ (top), and $0.46L_s$ (bottom). The results are for stripes of width $L = 0.46L_s$. Left and right panels are for a view perpendicular to the axis of the surface plane, a side view, and a close-up snapshot of surfactant aggregates, respectively. Water beads are not shown for clarity. The colour code is the same as that used in **Figure 6-2**.

Representative simulation snapshots of the surfactant aggregates obtained at increasing D are shown in **Figure 6-9**. For these simulations $L = 0.46L_s$. As discussed in **Figure 6-7**, when the two hydrophobic stripes are parallel and close to each other, hemicylindrical shells were obtained. At intermediate separations it is observed that the hemicylindrical aggregate is spoiled. At $D = 0.76L_s$ the results suggest that the hemicylindrical shell is partially formed, but it does not extend to the entire length of the simulation box. In addition, elongated hemispheres form on each of the two hydrophobic stripes. As D further increases to $D = 1.07L_s$, the hemicylindrical shell can no longer form (most likely because of entropic effects that prevent the formation of an extended partially unsupported monolayer suspended between the two narrow hydrophobic stripes). In addition, the aggregates that form on each hydrophobic stripe appear to be more elongated and irregular than the hemispheres discussed in **Figure 6-3c**. Visual analysis of sequences of simulation snapshots suggests that the aggregates formed at these conditions are very flexible and more freely along the hydrophobic stripes. This property of the self-assembled aggregates suggests the possibility that

aggregates such as those shown in **Figure 6-9** might be responsible for the high energy dissipation reported for quartz crystal microbalance experimental measurements by Wu *et al.* [179] when surfactants adsorbed on molecularly rough surfaces at conditions near the surfactants CMC. No evidence of cooperative effect was observed in the simulations when D was increased to $1.38L_s$ or above; the surfactant aggregates self-assembled on each hydrophobic stripe yield the hemi-spheres shown in **Figure 6-3c**.

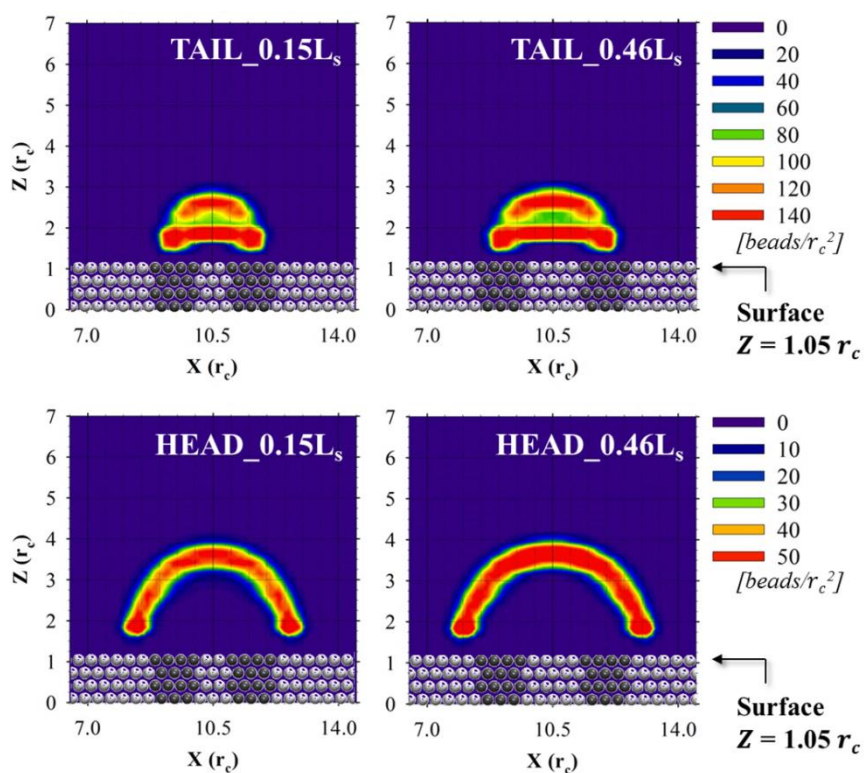


Figure 6-8: In-plane density distributions of surfactant tail groups (top) and headgroups (bottom) for surfactants adsorbed on two hydrophobic stripes located at minimum separation distances $D = 0.15L_s$ and $0.46L_s$ (left and right panels, respectively). The results are obtained for stripes of width $L = 0.46L_s$ along a plane perpendicular to the surface. Surface densities are expressed as number beads per r_c^2 .

Next, cooperative effects on hydrophobic stripes wider than those considered for the simulations of **Figure 6-7**, **Figure 6-8**, and **Figure 6-9** were examined. Representative

simulation snapshots of surfactant aggregates adsorbed on two stripes of width $L = 1.07L_s$ (top panels) and $L = 1.68L_s$ (bottom panels) at the separation $D = 0.15L_s$ are presented in **Figure 6-10**. Although the two hydrophobic stripes are close to each other for each of the systems considered in this figure, the results show that the surfactants yield hemi-cylinders analogous to those obtained on the individual hydrophobic stripes of width comparable to those considered here (compare the snapshots in **Figure 6-10** to those shown in **Figure 6-3**, bottom panels). Because the stripes considered in these simulations are wide with respect to the molecular length of one surfactant, the surfactant molecules do not find it advantageous to alter the stable structures discussed in **Figure 6-3** to **Figure 6-6**, even though two hydrophobic stripes are close to each other. Hemi-cylinders allow the surfactant molecules to maximise the favourable energetic interactions between the hydrophobic stripe and the tail groups, as well as those between those the various surfactant beads within the aggregates. As a consequence, the simulations do not show cooperative effects when the stripes are large enough for the formation of energetically stable aggregates.

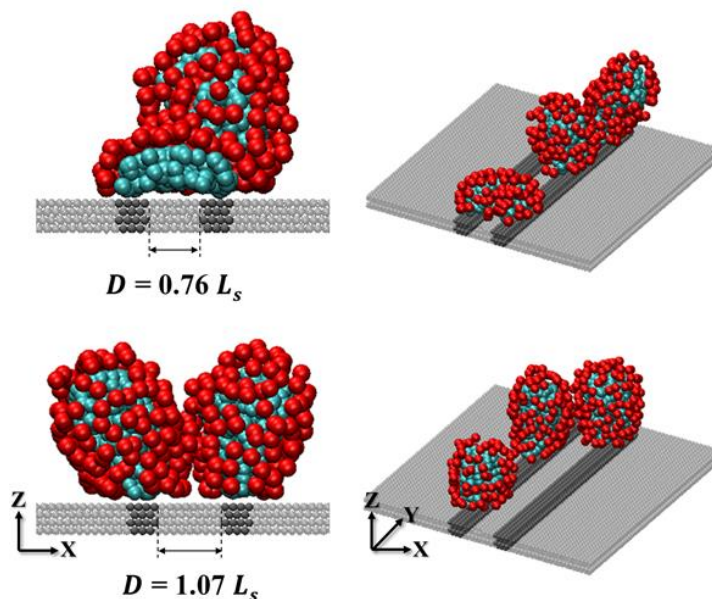


Figure 6-9: Representative simulation snapshots for surfactant aggregates self-assembled on two hydrophobic stripes located at minimum separation distances $D = 0.76L_s$ (top) or $1.07L_s$ (bottom). The results are obtained for hydrophobic stripes of width $L = 0.46L_s$. Left and right panels are for a view perpendicular to the axis of the surface plane and a side view, respectively. Water beads are not shown for clarity. The colour code is the same as that used in **Figure 6-2**.

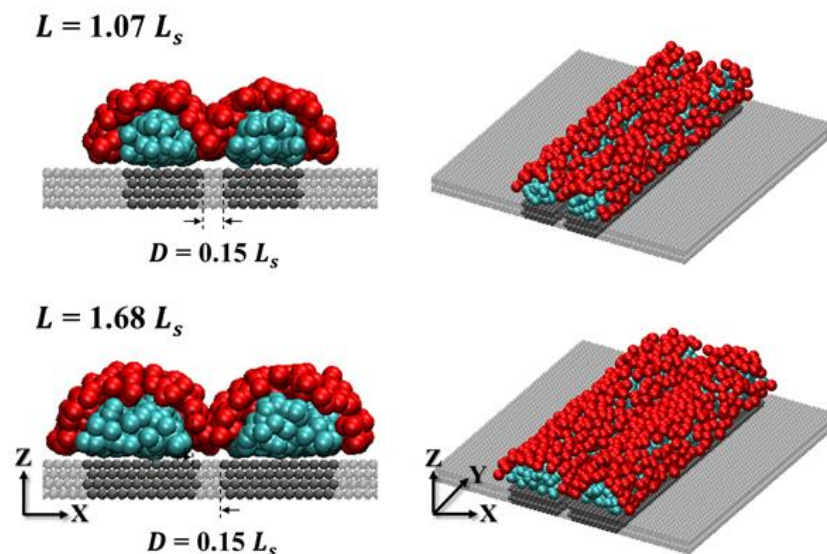


Figure 6-10: Representative simulation snapshots for surfactant aggregates self-assembled on two hydrophobic stripes of width $L = 1.07L_s$ (top) and $1.68L_s$ (bottom) separated by $D = 0.15L_s$. Left and right panels are for a view perpendicular to the axis of the surface plane and a side view, respectively. Water beads are not shown for clarity. The colour code is the same as that used in **Figure 6-2**.

6.5 Conclusions

The adsorption of surfactants on flat heterogeneous surfaces was studied by performing equilibrium dissipative particle dynamics simulations. Surfactant molecules were modelled as having a hydrophobic tail composed by two beads and a hydrophilic head composed by one bead. The surface had one or two hydrophobic stripes on which the surfactants can adsorb with the remainder of the surface repelling the surfactants. To understand the effect of surface heterogeneity on surfactant adsorption, the stripe width and the separation distance between two parallel stripes were varied systematically in the different simulations presented. For all systems, a sufficient amount of surfactant was present to maintain a bulk concentration above the critical micelle concentration after adsorption was completed. The surfactants yield a flat monolayer on a homogeneous hydrophobic surface and did not adsorb on the homogeneous repelling surface. Flat monolayers, hemi-cylinders, hemi-spheres, and individual surfactants were obtained as the width of the hydrophobic stripe decreased. The results showed

cooperative effects when two adsorbing stripes were separated, yet close to each other, but only when the stripes were narrower than the length of one surfactant molecule. Hemi-cylindrical shells and irregular structures were observed, as evidence of cooperativity. No evidence for cooperative behaviour was found when the stripes were close to each other, but wide with respect to the surfactant length, or when the narrow parallel stripes were farther than ~ 1.07 times the length of one surfactant molecule.

Chapter 7 Surfactant Aggregates Templated by Lateral Confinement

The material presented in this chapter was published in 2015, volume 119, pages 5467-5474 of The Journal of Physical Chemistry B.

7.1 Chapter overview

Self-assembly is widely seen as the method of choice for the bottom-up manufacture of supra-colloidal aggregates. Surfactants have been used extensively to appreciate qualitatively and quantify driving forces and methodologies for controlling self-assembling processes and the resultant self-assembled aggregates. However, not much is known regarding self-assembled surfactant aggregates formed on heterogeneous surfaces. If heterogeneous surface features affect the morphology of surfactant aggregates, it is possible that new templating methodologies could be designed by engineering surfaces. In this chapter equilibrium dissipative particle dynamics (DPD) simulation results for surfactants adsorbed on model heterogeneous surfaces are reported. The simulation results reveal that, depending on the morphological and chemical properties of the solid substrate, a number of not-before-reported structures can be obtained for the self-assembled aggregates. The results presented could be useful for the manufacture of new coatings and materials, e.g., via the admicellar polymerization procedure, as well as for interpreting experimental data for surfactant adsorption on heterogeneous surfaces.

7.2 Introduction

The self-assembly of surfactants in solution and on surfaces is a subject of fundamental studies that have a number of directly related important practical consequences. For example, by adsorbing surfactants on substrates it is possible to enhance the stability of dispersions containing nanoparticles [26,206,207], assist the synthesis of composite materials [208,209], promote admicellar polymerization [6,210], facilitate lithography processes [211,212], etc. Because of this vast interest, many have considered the adsorption and a self-assembly of surfactants, experimentally, computationally via

simulations, and theoretically. While most of the research concerning surfactants adsorption and self-assembly on surfaces considered substrates with as uniform surfaces as possible, interest in the effect of heterogeneous surfaces is growing, as understanding regarding self-assembled aggregates formed on flat homogeneous surfaces cannot be used straightforwardly to predict the surfactant behaviour on heterogeneous substrates. In fact, surface heterogeneity seems to affect the shape of surfactant adsorption isotherms [59,181,213-215], the heat of adsorption [215,216], the amount of surfactants adsorbed at given thermodynamic conditions [59,177,180,215,217], and the structures of surfactant aggregates [77,177,180-183,214,217-220]. Better understanding and quantification of the effect of surface heterogeneity on self-assembled surfactant aggregates can have important consequences for all the practical applications in which surfactants are used, some of which are mentioned above, but also for designing new processes for the bottom-up synthesis of supra-colloidal aggregates and perhaps for the production of responsive coatings.

Towards a systematic analysis on the effect of surface heterogeneity over the properties of self-assembled surfactant aggregates, coarse-grained simulation approaches offer the distinct advantage of allowing systematic change of parameters of interest (e.g., the nature of the surface and its molecular-scale roughness). Compared to atomistic simulations, the coarse-grained models lack chemical identity of the molecules being simulated, but allow determination of results representative of equilibrated systems. For example, in some cases it can be observed the reorganisation of surfactants within the self-assembled aggregates when conducting coarse-grained simulations, while observing similar effects is prohibitive when employing atomistic molecular dynamics simulations. The results from coarse-grained simulations can and should be experimentally verified. Experimentally, the manufacture of reproducible surface features of dimension comparable to the size of a surfactant molecule remains challenging, as is the direct observation of self-assembled structures of this size. However, surface spectroscopy methods are being improved and the resolution achieved is becoming comparable to that accessible in simulations [218,219,221-223].

To gain new insights into morphology of the surfactants self-assembled on model heterogeneous surfaces, the coarse-grained dissipative particle dynamics (DPD) simulation method [93,224] is implemented, which was recently used to study Pickering emulsions [225,226] and surfactant adsorption on patterned flat surfaces [217]. DPD simulations have been widely used in the literature to describe the self-assembly of surfactants inside [102] and outside [120] single-walled carbon nanotube (SWNTs), between adjacent SWNTs organised in bundles [119], and to study many other systems.

7.3 Methodology

The simulations are run with the package LAMMPS [184]. The coarse-grained model used to simulate water and surfactant molecules is described in details in Chapter 6, and it is described briefly in **Figure 7-1a**. Each water bead represents five water molecules, and has volume $V_b = \sim 0.15 \text{ nm}^3$ [227]. The reduced density of one DPD bead (the average number of beads in $1 r_c^3$) was set to $\rho = 5$. The DPD cut-off distance r_c was set to 0.90856 nm, as obtained by $r_c = \sqrt[3]{\rho V_b}$. The model surfactant was a single chain of three beads: two hydrophobic tail and one hydrophilic head beads. Consecutive beads in the surfactant chain were connected via harmonic springs with spring constant $k_s = 100 k_B T / r_c^2$ and equilibrium bond length $r_0 = 1.04 \text{ nm}$. The interaction parameters between different beads are summarised in **Table 7-1**. On an atomically flat homogeneously hydrophobic surface this surfactant yields a flat monolayer, as described elsewhere [217].

The surfaces considered are formed by individual trenches, as shown in **Figure 7-1b**. The trench is surrounded by a surface that effectively repels the surfactants, thus reducing the amount of surfactants it is needed to simulate to maintain a desired bulk surfactant concentration. The solid surface within the trench is considered hydrophobic, at least in part. In some cases the beads at the bottom of the trench are considered hydrophobic (fully hydrophobic trench), while in other cases these beads are considered surfactant repellent (partially hydrophobic trench). The interaction parameters chosen to describe the surface properties are shown in **Table 7-1**.

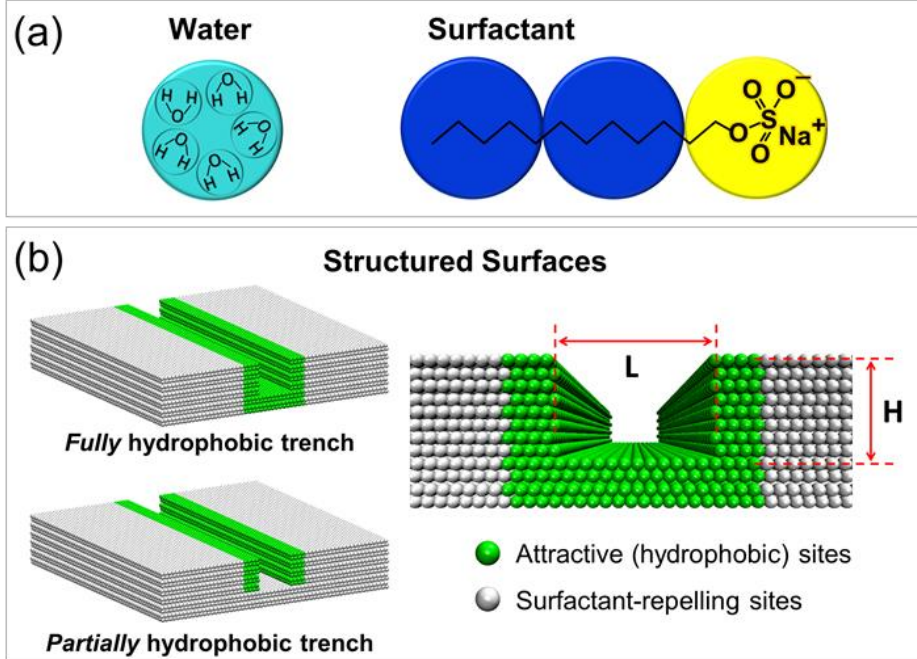


Figure 7-1: Schematic illustration of (a) the coarse-grained water and model surfactant and (b) the structured surface containing either the fully or the partially hydrophobic trench. In panel (a) the DPD water bead (cyan) represents five water molecules. Each bead in panel (a) has the same volume. The surfactant is composed of two tail beads (blue) and one head bead (yellow). The trench depth H and width L are changed systematically. Hydrophobic and surfactant-repelling surface sites are shown as green and grey, respectively, in panel (b).

Table 7-1: DPD interaction parameters in $k_B T / r_c$ units for water (w), surfactant head group (h), surfactant tail group (t), surfactant-repelling surface site (rs), and surfactant attractive (hydrophobic) surface site (as)

a_{ij} or a_{ji}	w	h	t	rs	as
w	15	0	81	15	81
h		15	69	15	69
t			15	81	15
rs				15	81
as					15

All simulations were performed in the NVT ensemble, within a simulation box of size $21 \times 21 \times 42 r_c^3$. The fluid density in the simulation boxes corresponds to 5 beads (either water or surfactant) per r_c^3 . Periodic boundary conditions were applied along X and Y

directions. The reduced temperature was maintained at $k_B T = 1$, and the time step was $\Delta t = 0.156$ ps.

The effect of trench architectural features (i.e., depth H and width L) and chemical properties (i.e., fully and partially hydrophobic trench) on the surfactant aggregate structures is quantified. H and L are expressed in units of one surfactant length (L_S), which is ~ 2.08 nm for sodium dodecyl sulphate [228]. The initial configurations were prepared by placing the surfactant molecules randomly within the aqueous solution above the trenches; after that the systems were filled with water beads to the desired density. From these initial configurations the simulations show that individual surfactant molecules rapidly migrate to the trench; those surfactants remaining in solution form aggregates/micelles within ~ 0.25 μ s of simulation. The kinetics of surfactant aggregation and adsorption were not quantified further. As the surfactant behaviour depends on its chemical potential, all simulations were conducted maintaining the bulk surfactant concentration at around 20-23 mM (≈ 3 CMC) by adding/deleting surfactants as necessary. Each system was simulated for 1.248 μ s, with the last 0.156 μ s used for data analysis. To ensure reproducibility, each system was simulated twice at the same surfactant concentration, and a third time at slightly higher surfactant bulk concentrations. Additional details regarding the computational methodology are reported in Chapter 6.

7.4 Results and Discussion

A systematic report on the effects of changing H and L on the self-assembled surfactant structures is presented as the Appendix D. The most striking effects and unexpected aggregate structures are obtained in trenches of $L = 1.30L_S$, varying H and the chemical features of the trench surface. Representative simulation snapshots that summarise the results obtained for trenches that are fully hydrophobic are shown in **Figure 7-2**. From **Figure 7-2a** to **Figure 7-2f**, the depth of the trench increases from $H = 0.61L_S$ to $6.42L_S$.

In the shallow trench (**Figure 7-2a**) the surfactants yield a monolayer, with the tails perpendicular to the hydrophobic surface. While this morphology could have been

expected, note that no surfactant adsorbs on the terraces of the trench (because their lateral dimension is too small to allow surfactants to adsorb, as discussed in Chapter 6). On flat hydrophobic stripes of width larger than half the surfactant length, the prior simulations predicted the formation of hemi-cylindrical structures. The results in **Figure 7-2a** are different, because the surfactants are aligned perpendicularly to the bottom of the trench. In this configuration favourable tail-hydrophobic surface interactions are maximised, as well as tail-tail interactions. Note that, perhaps not surprisingly, the surfactant head groups are not found near the hydrophobic surface sites in **Figure 7-2a**.

The first unexpected surfactant aggregate forms as the trench depth increases above one surfactant length. The results obtained when $H = 1.22L_s$ are shown in **Figure 7-2b**. At these conditions, the results show that the surfactant yields a bilayer. While the portion of the bilayer exposed to the aqueous bulk solution does not differ substantially compared to the results shown in **Figure 7-2a**, surprisingly, it is observed that in the bottom part of the bilayer the surfactant head groups are found in close proximity of the hydrophobic surface. Analysis of the simulations shows that this is possible because some water beads penetrate near the trench bottom, stabilising the surfactant aggregate (see water density distributions below). In addition, the structure in **Figure 7-2b** must be stabilised by favourable tail-tail and tail-surface interactions.

As the trench depth increases further to $H = 1.83L_s$ a multi-layered structure is observed (**Figure 7-2c**). Analysis of this aggregate shows that some surfactants are self-assembled into a monolayer at the bottom of the trench, with their tails in contact with the solid substrate. This mono-layer effectively changes the chemical nature of the bottom of the trench, as ‘experienced’ by additional surfactants that adsorb in the trench. These additional surfactants are exposed to a layer of heads. The combination of these hydrophilic heads between which some water beads are found, and the surrounding hydrophobic surfaces on the trench walls promotes the self-assembly of a bilayer structure, similar to that shown in **Figure 7-2b**. However, the surfactants are packed more densely in **Figure 7-2c** than in **Figure 7-2b**. Results similar to those just discussed are obtained when $H = 2.14L_s$ (not shown for brevity), and also when $H = 2.45L_s$

(**Figure 7-2d**). Detailed comparison between the structures shown in **Figure 7-2c** and **Figure 7-2d** reveals that in the deeper trenches the surfactants within the bilayer have a tendency to elongate along the hydrophobic walls of the trench, likely to maximise the favourable tail bead-surface contacts. A larger amount of water is found between the heads in the deeper trench. It is also found a larger number of surfactants at the top of the trench in **Figure 7-2c** than in **Figure 7-2d**. This appears to be a consequence of the wider area occupied by the surfactant heads in contact with the bulk water (compare, visually, the top of **Figure 7-2c** to the top of **Figure 7-2d**).

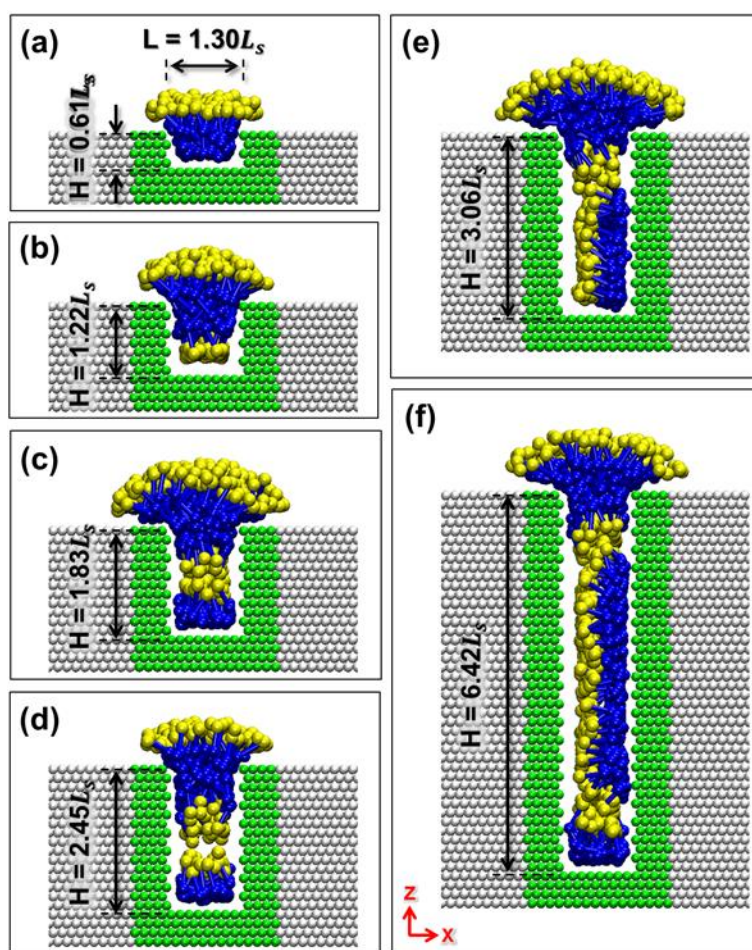


Figure 7-2: Equilibrium simulation snapshots of self-assembled surfactant aggregates in fully hydrophobic trenches of width $L = 1.30L_S$. From (a) to (f), the results are obtained for trenches of increasing depth $H = 0.61L_S$, $1.22L_S$, $1.83L_S$, $2.45L_S$, $3.06L_S$, and $6.42L_S$, respectively. The colour code is the same as that used in **Figure 7-1**. For clarity, water beads are not shown, nor are surfactants present in the bulk.

The second unexpected transition occurs when $H = 3.06L_s$ (**Figure 7-2e**). Visual inspection of the self-assembled aggregate at the top of the trench reveals a layered structure similar to that discussed in **Figure 7-2c**, with the surfactant molecules extending from the trench with their head groups exposed towards the bulk aqueous phase. Analysis of the aggregate structure within the trench shows, however, different behaviour compared to results described in shallower trenches. First, at the bottom of the trench no evidence of a monolayer is found. Instead, from the bottom of the trench to the bottom part of the surface bilayer, remarkably, the surfactants yield a flat monolayer adsorbed on one of the two trench walls. The surfactant tails are in contact to the surface through the removal of hydrophobic tails from contact with water. The heads are projected towards the other hydrophobic wall. Analysis of simulation snapshots reveals that the unfavourable interactions between heads and hydrophobic wall are shielded by water beads, found within the trench. This structure must form because alternative ones would be characterised by higher free energy. For example, if a structure such as the one shown in **Figure 7-2d** had formed, there would be too many water beads in the trench, separating the bottom monolayer and the top bilayer. If a monolayer at the bottom had formed in conjunction with a monolayer at one of the two lateral walls, then the number of tail-tail contacts would not have been maximised.

Increasing the trench depth further to $H = 6.42L_s$ yields the equilibrium structure shown in **Figure 7-2f**. This exotic self-assembled aggregate maintains features that are similar to those discussed in **Figure 7-2c**, **Figure 7-2d**, and **Figure 7-2e**. The surfactant aggregate at top of the trench, exposed to the bulk aqueous solution, is similar to those obtained in **Figure 7-2c**, **Figure 7-2d**, and **Figure 7-2e**, somewhat even to that of **Figure 7-2b**. At the bottom of the trench the surfactants yield a monolayer similar to that discussed in **Figure 7-2c**, and **Figure 7-2d**. In between the top and the bottom of the trench it is observed the self-assembled flat monolayer discussed in **Figure 7-2e**. Evidently, this configuration allows for a sufficiently large number of tail-tail and tail-hydrophobic surface contacts to offset the unfavourable head-hydrophobic surface contacts established. The surfactant heads are associated with water beads, which shield

the unfavourable interactions between the hydrophilic heads and the hydrophobic trench surfaces.

The self-assembled structure discussed in **Figure 7-2e** and **Figure 7-2f** (in particular the monolayer adsorbed on one of the two vertical walls) is consistent with that predicted by self-consistent field (SCF) theory for surfactants confined in between two infinite surfaces (i.e., frontal confinement [214]). The simulations suggest that frontal confinement is the dominant effect for surfactant aggregates confined in trenches of depth $H \geq 3.06L_s$. It appears that the structures formed at the top and at the bottom of the trench represent ‘defects’ due to finite size effects, when the results for frontal confinement due to infinite parallel walls are used to predict the surfactant behaviour in trenches. It is perhaps worth pointing out that assessing experimentally the surfactant self-assembled aggregates shown in **Figure 7-2** using, e.g., an atomic force microscope (AFM) would not be sufficient to differentiate the structures obtained by the simulations, as the shape of the aggregates exposed to the aqueous bulk solution only minimally changes as the depth of the trench varies.

The results shown in **Figure 7-2** suggest that the bottom of the trench strongly affects the structure of the self-assembled surfactant aggregate. To further quantify such effects, additional simulations were conducted for systems analogous to those discussed in **Figure 7-2**, with the exception that the bottom of the trench is described as ‘surfactant-repellent’ rather than hydrophobic (partially hydrophobic trench, as shown in **Figure 7-1**). As discussed in Chapter 6, the surfactants simulated here do not adsorb on a uniform flat surface composed of such beads (see **Figure 6-2b**). The results are summarised in **Figure 7-3**. For each trench depth, the aggregates structure is significantly different compared to the results discussed in relation to **Figure 7-2**.

When $H = 0.61L_s$ (**Figure 7-3a**) the surfactant tails do not adsorb at the bottom of the trench, in contrast to what discussed in **Figure 7-2b**. Instead, the heads are projected towards the bottom of the trench (yet they are separated from the bottom by water beads), and a bilayer is observed instead of the monolayer reported in **Figure 7-2a**. A bilayer structure similar to the one just discussed is also discovered in the trenches of

depth $H = 1.22L_s$ and $1.83L_s$, as shown in **Figure 7-3b** and **Figure 7-3c**, respectively. The main difference is that the surfactants extend towards the interior of the trench, because in so doing they maximise the number of favourable contacts between tails and hydrophobic surface. The structure observed in **Figure 7-3b** is similar to the analogous structure observed in **Figure 7-2b**, with the only difference that the surfactants seem to be pushed a little further from the bottom of the trench in **Figure 7-3b**. Thus it appears that changing the chemistry of the bottom of the trench has little effect on the surfactant aggregate when $H = 1.22L_s$. When $H = 1.83L_s$ the structures shown in **Figure 7-2c** and **Figure 7-3c** differ mostly from the lack of the monolayer at the bottom of the trench when this is surfactant repellent.

It should be noted here one important difference between the self-assembled aggregate observed in the three rather shallow trenches (i.e., $H = 0.61L_s$, $1.22L_s$, and $1.83L_s$) with surfactant-repellent bottom. It concerns the stretching of the surfactant molecules along the trench walls. This is more evident in the deeper trenches (**Figure 7-3b** and **Figure 7-3c**), but it is present also for the shallower trenches. The stretching is most likely a demonstration that the surfactants benefit from advantageous tail-hydrophobic surface interactions, and attempt to maximise these interactions when they can. Another significant difference between the results in **Figure 7-2** and **Figure 7-3** for shallow trenches is the presence of water molecules at the bottom of the trenches with surfactant-repellent surface. Especially for the system shown in **Figure 7-3c**, it is found a large amount of water shielding the surfactant heads from the repelling surface sites (see density distributions below). This is a direct consequence of the bottom of the trench, which repels surfactants in **Figure 7-3**.

The first unexpected transition occurs as the trench depth increases further to $H = 2.45L_s$ (**Figure 7-3d**). The aggregates described for the shallower trenches (i.e., bilayers) cannot stretch further into the trench, but the surprising result is that the aggregates show an irregular structure. The results show cylindrical micellar structures that span the distance between the two walls of the trench (with the heads exposed to water), and pinned to the top of the trench. Most of the trench is filled with water, which was not expected. In

Figure 7-2d the bottom of the trench was covered by a monolayer of surfactants, which effectively transformed the nature of the surface from hydrophobic (the solid) to hydrophilic (the surfactant heads). Comparing **Figure 7-3d** to **Figure 7-2d** suggests that when the trench bottom is strongly repellent to the surfactants, the effect can be very long-ranged, and effectively can lead to the destabilisation of the self-assembled aggregate formed within the trench. Mild hydrophilic features of the trench bottom would not result in the results shown in **Figure 7-3d**.

A second unexpected transition occurs as the trench depth is increased to $H = 3.06L_S$ (**Figure 7-3e**). The irregular self-assembled aggregates shown in **Figure 7-3d** transition to a more space-filling structure characterised by a large number of surfactants confined within the trench. At the top of the trench, it is found a bilayer similar to that discussed in **Figure 7-2e**. At the bottom of the trench, as expected, the surfactants are repelled by the solid surface. Unexpectedly, in the region between the bottom of the trench and the bilayer formed at the top a number of cylindrical aggregates form. These are similar to those discussed in **Figure 7-3d**, but they are completely buried within the trench, and they occupy the entire trench. While the tails favourably interact with either the trench walls or other tails, the heads favourably interact with water beads. It is surprising that the monolayer adsorbed on the trench wall discussed in **Figure 7-2e** is not observed when the bottom of the trench is surfactant-repellent. Instead, the results suggest that the cylindrical micelles formed within the trench minimise the perturbation due to the change in chemistry at the bottom of the trench. It is expected that the monolayer adsorbed on one wall should be recovered as the trench depth increases further, as is indeed observed in the equilibrium self-assembled aggregate obtained when $H = 6.42L_S$ (**Figure 7-3f**). This aggregate shows the features discussed in **Figure 7-3e** at the top and bottom of the trench. In between the top and the bottom, the surfactants yield the flat monolayer discussed in **Figure 7-2e** and **Figure 7-2f**.

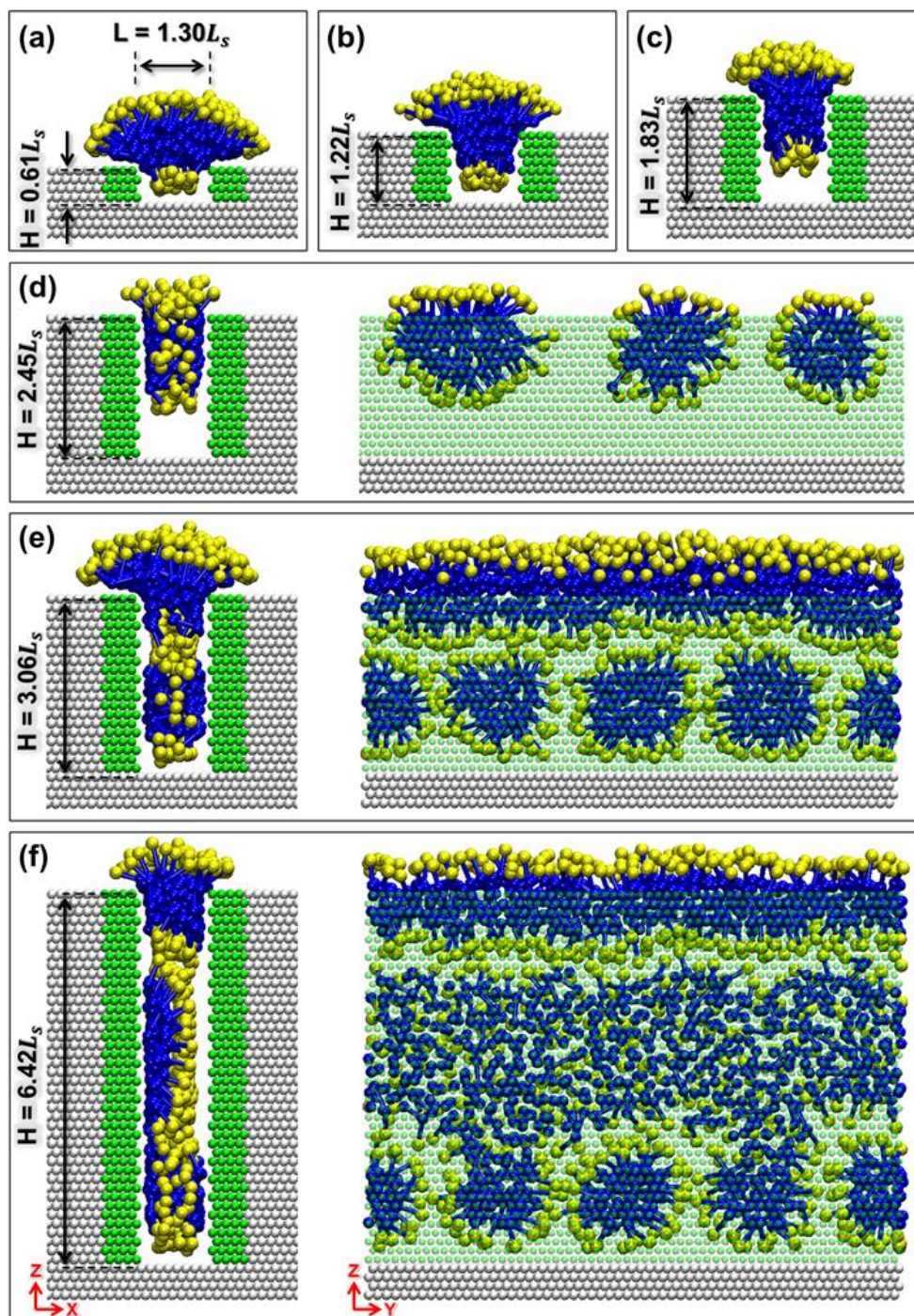


Figure 7-3: Equilibrium simulation snapshots of self-assembled surfactant aggregates in partially hydrophobic trenches of width $L = 1.30L_s$. From (a) to (f), the results are obtained for trenches of increasing depth $H = 0.61L_s$, $1.22L_s$, $1.83L_s$, $2.45L_s$, $3.06L_s$, and $6.42L_s$, respectively. The colour code is the same as that used in **Figure 7-1**. In panels (d), (e), and (f), both front (left) and side (right) views of surfactant aggregates are reported.

To quantify the structural observations discussed above, density profiles within planes perpendicular to the trench were calculated. The results are presented in **Figure 7-4** and **Figure 7-5**. The left panels display the results obtained for surfactant tails, the right panels the heads. From top to bottom the trench depth increases ($H = 0.61L_s$, $1.22L_s$, $1.83L_s$, and $6.42L_s$). The results are consistent with the simulation snapshots. In **Figure 7-4**, when $H = 0.61L_s$, as surfactants self-assemble into a monolayer, the results show evidence of the tails accumulating within the trench. The heads are oriented towards the water phase, as indicated by large densities above the trench. When $H = 1.22L_s$, the density profiles confirm an increased amount of surfactant tails sandwiched between two layers of surfactant heads inside and outside the trench. This is a consequence of the formation of the surfactant bilayer. When $H = 1.83L_s$, the density profiles obtained for the tails display high densities at the bottom of the trench, indicating that the tails remain in contact with the bottom surface of the trench. The results are consistent with the formation of two layers of surfactant heads in the middle of the trench. When $H = 6.42L_s$, in the middle of the trench, the results are consistent with the formation of a flat monolayer adsorbed on one of the two trench walls. In all cases, the density profiles for surfactant heads are found near those for tails.

The results shown in **Figure 7-5** are consistent with the snapshots of **Figure 7-3**, confirming that the surface chemistry at the bottom of the trench strongly affects aggregate morphology. The possible cause for this effect is the accumulation of water beads in contact with the bottom surface of the trench (water density profiles are shown in **Figure 7-6**). The results in **Figure 7-5** show that the surfactants tend to self-assemble into a bilayer near the top of the trench when $H = 0.61L_s$, $1.22L_s$, and $1.83L_s$. When $H = 6.42L_s$, the density profiles for both surfactants tails and the heads show weak intensity, because the cylindrical micelles discussed in **Figure 7-3** are mobile within the trench. In the middle region within the trench, the density profiles appear to be consistent with the formation of a flat monolayer on one of the two walls of the trench.

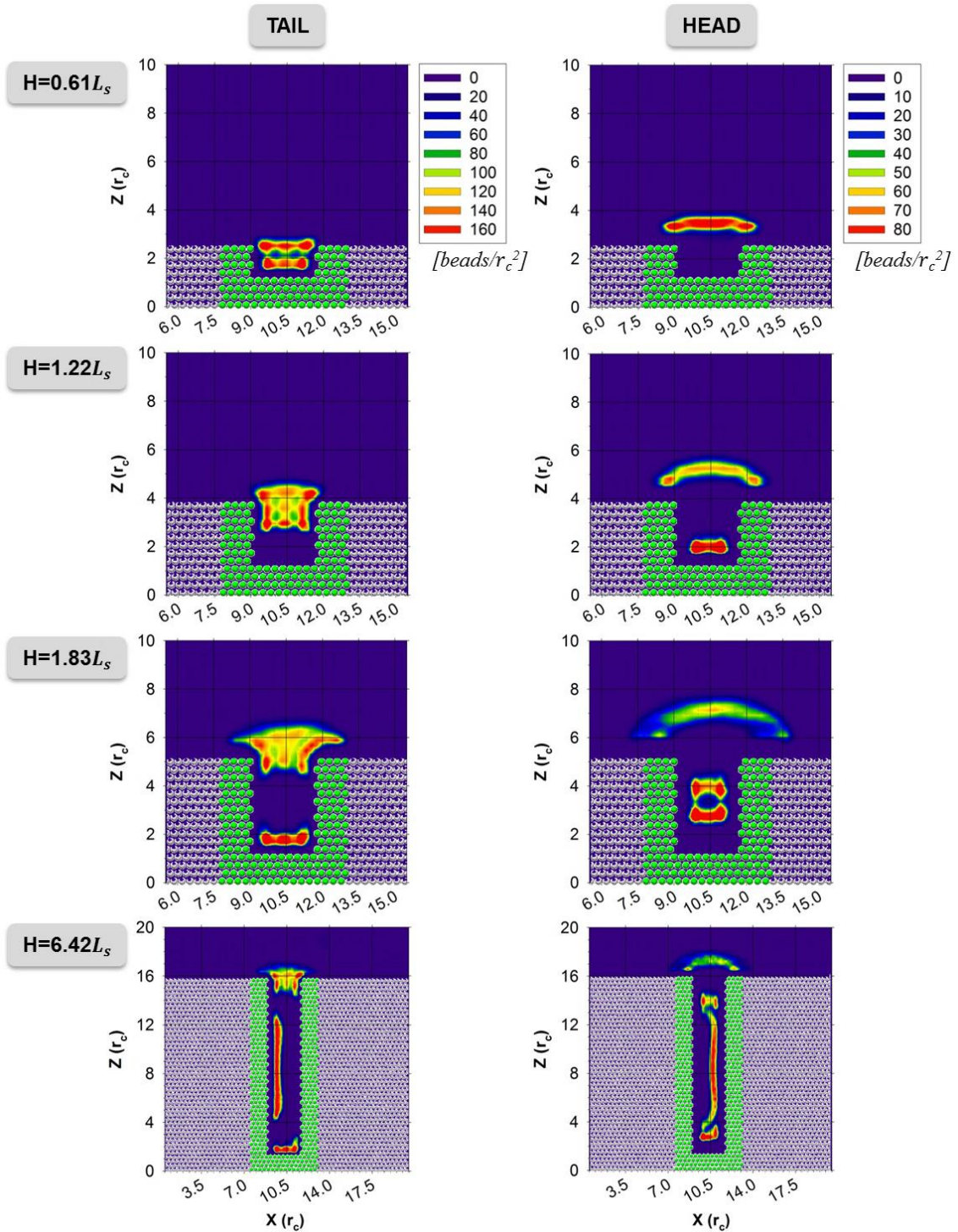


Figure 7-4: Density profiles of surfactant heads (left) and surfactant tails (right) for surfactants self-assembled within fully hydrophobic trenches of width $L = 1.30L_s$. Top to bottom panels are for trenches of depth $H = 0.61L_s$, $1.22L_s$, $1.83L_s$, and $6.42L_s$, respectively. Densities are in beads per r_c^2 and computed along planes perpendicular to the trench axis (XZ plane).

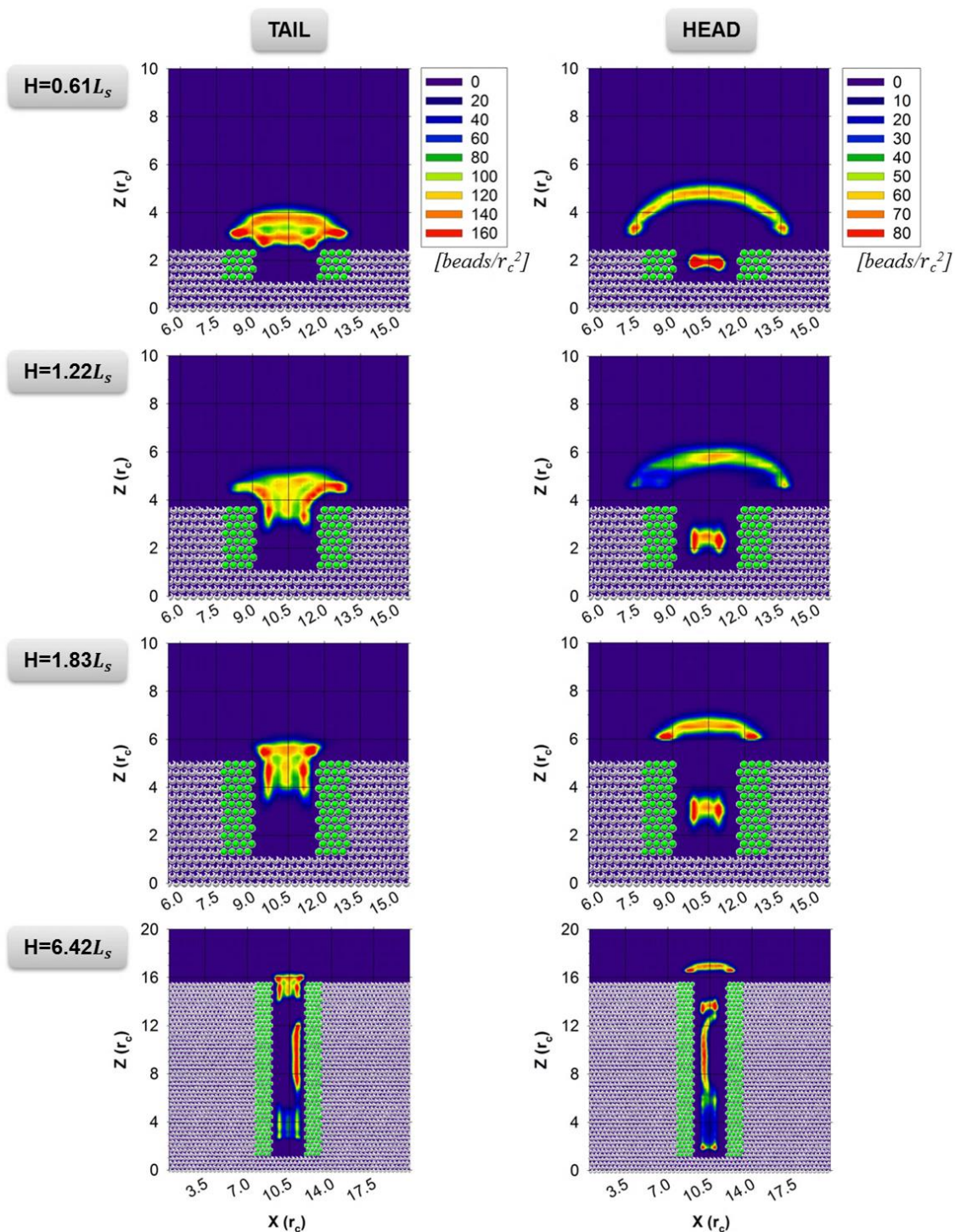


Figure 7-5: Same as **Figure 7-4** but for surfactants self-assembled within partially hydrophobic trenches.

The time-averaged density profiles of water beads within fully and partially hydrophobic trenches in the presence of the surfactant aggregates were also quantified. The results are shown in **Figure 7-6**. When the trench is fully hydrophobic (**Figure 7-6a**) the results show no evidence of adsorbed water when $H = 0.61L_S$. When $H = 1.22L_S$ some water beads penetrate near the bottom of the trench, and they aid the stabilisation of the surfactant bilayer. These beads yield a strong density peak at $\sim 0.4L_S$. As the trench depth increases further to $H = 1.83L_S$, it is found a multi-layered surfactant aggregate. In correspondence, a large amount of water beads associate with two layers of the head groups within the trench, yielding two peaks at $\sim 0.8L_S$ and $1.2L_S$. Increasing the trench depth to $H = 6.42L_S$ yields a flat monolayer on one of two walls, which is consistent with an approximately constant water density profile in the region of 1.8 to $4.6L_S$ near one of the walls. These water beads associate with the surfactant head groups and shield the unfavourable interactions between the hydrophilic head groups and the hydrophobic trench surfaces.

When the trench is partially hydrophobic (**Figure 7-6b**) the results show that a large amount of water adsorbs near the bottom of the trenches, independently of the trench depth. This adsorption yields a large density peak at $0.4L_S$, measured from the bottom of the trench. This large water density seems to push the surfactants away from the bottom of the surface. The water beads favourably interact with the surfactant heads, which is consistent with the simulation snapshots shown above. As the trench depth increases from $H = 0.61L_S$ to $1.83L_S$, the results show a shoulder appearing near the main density peak, because more water adsorbs in the deeper trenches and because the surfactant heads become mobile on the corresponding aggregates. When $H = 6.42L_S$, the results show a region, from 2.8 to $4.6L_S$, with approximately constant water density; this is consistent with the formation of a flat monolayer on one of the trench walls, as discussed in the simulation snapshots above (see **Figure 7-3**).

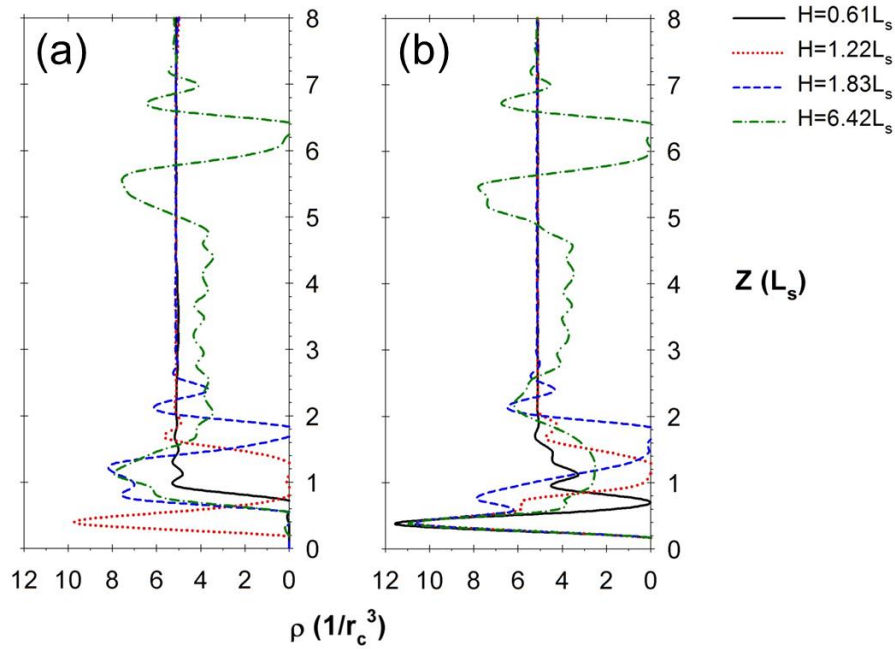


Figure 7-6: Density distributions of water beads in (a) fully and (b) partially hydrophobic trenches of width $L = 1.30L_s$ and depth $H = 0.61L_s$ (solid black line), $1.22L_s$ (red dotted line), $1.83L_s$ (blue dashed line), and $6.42L_s$ (green dashed-dotted line). Densities are expressed in number of beads per r_c^3 and computed from the bottom trench surface along the Z direction. Distances are expressed in units of one surfactant length (L_s).

7.5 Conclusions

In summary, equilibrium dissipative particle dynamics simulations were performed to study the self-assembly of surfactant aggregates within trenches of size comparable to the length of one surfactant. Depending on the geometrical (i.e., depth H , width L) and chemical (i.e., fully or partially hydrophobic) properties of the trenches, the simulation results reveal a number of aggregate structures that cannot be predicted based solely on the results obtained for the same surfactants adsorbed on flat homogeneous surfaces. The most striking results were obtained for surfactants adsorbing in trenches of width 1.30 times the length of a surfactant. In fully hydrophobic trenches of this width, monolayers, bilayers, multilayers, and interconnected structures were obtained depending on the depth of the trench. The results changed significantly when the surface at the bottom of

the trench was rendered repellent to the surfactants. In this case it was observed structures that appeared similar to those just discussed when observed from outside of the trench, but rather irregular inside of the trench. In many cases cylindrical aggregates that span the trench width was observed, which were not observed in trenches that were completely hydrophobic. The simulation results suggested that chemical perturbations at the bottom of the trench manifest in morphological changes in the self-assembled aggregates that extend to lengths comparable to 3-5 surfactant lengths. These findings could be useful for the manufacture of new coatings and materials. For example, the results suggest that adsorbing surfactants on patterned surfaces, perhaps followed by admicellar polymerization procedures, it is possible to alter the surface properties and perhaps manufacture supra-colloidal structures of controlled features.

Chapter 8 Summary and Outlook

Extensive all-atom molecular dynamics (MD) simulations were employed to study the morphology of surfactant aggregates self-assembled on single-walled carbon nanotube (SWNTs). The anionic surfactants including linear and branched sodium dodecyl benzenesulfonate (SDBS), caesium dodecyl sulphate (CsDS), and sodium dodecyl sulphate (SDS) were considered in this study. All simulations were performed at ambient conditions on (6,6), (12,12), and (20,20) SWNTs for different surfactant surface coverages. Because of computing limitations, relatively low surface concentrations were considered. In **Chapter 3**, the results showed that linear and branched SDBS surfactants yield disordered aggregates on the three SWNTs. The self-assembled aggregates of linear SDBS were found to be strongly dependent on the surface coverage and, to a lesser extent, on the nanotube diameter. On (6,6) SWNT, at low surface coverage, the linear SDBS tails have a tendency to orient parallel to the cylindrical axis of the SWNT. At low surface coverage, the linear SDBS tails and benzene rings adsorb close to the nanotube surfaces. As the surface coverage increases, the headgroups are mostly exposed to water, effectively pulling the benzene rings of linear SDBS away from the SWNT surfaces. The results showed that changing the surfactant molecular structure predominantly affects the packing of surfactants on the SWNTs, especially at low surface coverage. The branched SDBS surfactants were found to adsorb via the surfactant tails on the SWNT surfaces, while the benzene rings and the headgroups are exposed to water. The aggregate structure formed by branched SDBS appears to depend on the SWNT diameter. The results suggested that branched molecules should be suitable for stabilising (6,6) SWNT. In **Chapter 4**, when equimolar mixtures of linear and branched SDBS were present, there was no strong effect due to SWNT diameter on the morphology of mixed SDBS aggregates, although the results showed that the adsorbed aggregates are strongly dependent on surface coverages. The surface aggregates of SDBS mixtures were, in general, consistent with those obtained for either pure linear or pure branched SDBS. On (6,6) SWNT, random distributions of linear and branched SDBS molecules were observed on the nanotube surfaces, while on the wider SWNTs there was evidence of segregation (i.e., branched SDBS mostly packs near other

branched molecules). The results suggested that the lack of specificity in stabilising aqueous dispersions of carbon nanotubes using SDBS surfactants is probably due to the presence of multiple isomeric molecules in commercial surfactant samples. Regarding salt effects presented in **Chapter 5**, the results showed that the counterions (Cs^+ instead of Na^+) strongly affect the morphology of dodecyl sulphate surfactants adsorbed on SWNTs. The surface aggregates with Cs^+ ions, compared to Na^+ , yield a more compact coverage of the (6,6) SWNT. The Cs^+ can pull the surfactant heads away from the SWNT surfaces, and thus water molecules did not swell the adsorbed aggregates. On (12,12) and (20,20) SWNTs, the results did not show strong difference between CsDS and SDS aggregate structures. These observations are qualitative agreement with experimental observation.

Coarse-grained dissipative particle dynamics (DPD) simulations were implemented to investigate the adsorption and aggregation of aqueous surfactants on patterned surfaces. The DPD technique was chosen because of its capability to simulate large systems for extended periods of time and to assess the amount of surfactants adsorbed on surfaces as a function of bulk surfactant concentration. The patterns considered were one/two hydrophobic stripes and fully/partially hydrophobic trenches. Surfactant adsorption was allowed on the hydrophobic patterns which surrounded by surfaces that were effectively repulsive to surfactants. For all systems, a sufficient amount of surfactant was present to maintain a bulk concentration above the critical micelle concentration after adsorption was completed. In **Chapter 6**, on the surfaces consisting of one hydrophobic stripe, the results showed evidence of lateral confinement, in which flat monolayers gradually change to hemi-cylinders, to hemi-spheres and eventually to individual surfactants with decreasing stripe width. On the surfaces containing two hydrophobic stripes, the results showed cooperative behaviour. For example, the surfactants yield hemi-cylinder shells and irregular structures when both the distance between the two parallel stripes and the width of the stripe are less than the length of one surfactant molecule. There was no evidence for cooperative effect when the stripes were close to each other, but their widths were wide with respect to the surfactant length, or when the distance between the two narrow stripes was greater than ~ 1.07 times the length of one surfactant molecule.

In **Chapter 7**, the results revealed various aggregate structures self-assembled within the trenches, depending on their geometrical (depth and width) and chemical (fully and partially hydrophobic) properties. In fully hydrophobic trenches of trench width ~ 1.3 times the length of one surfactant molecule, monolayers, bilayers, multilayers, and interconnected structures can be observed as the depth of the trench increases. The aggregate morphology changed significantly when the bottom of the trench was repulsive to the surfactants (i.e., partially hydrophobic trenches). In this case, the results showed that the cylindrical aggregates span the distance between the two walls of the trench. Such an adsorbed aggregate structure was not observed in trenches that were completely hydrophobic.

There are some limitations in the study that should be considered. One limitation in MD simulation study is the computing power limitations preventing simulation of systems of higher surfactant concentrations (comparable to experimental data) as well as capturing the exchange of surfactant monomers between the bulk solution and the surfactant aggregates self-assembled on surfaces. Thus, the results reported here only show local structural features of the adsorbed aggregates on SWNTs under known surfactant coverage. Alternative computational approaches, including DPD should be employed to study larger surfactant densities. Another limitation is, in DPD simulation study, the model surfactant simulated was not intended to reproduce all physical properties observed for ionic SDS surfactants because electrostatic interactions and bond angle bending parameter were not taken into account. However, by quantifying critical micelle concentration and micelle size, the results were generally consistent with those reported in the literature for SDS surfactants, both from experiments [190-192] and from simulations [193-195].

In summary, these findings could (1) provide physical guidelines for selecting and/or designing surfactant formulations to improve the quality of the SWNT dispersions in water, and (2) assist in understanding surfactant adsorption on heterogeneous surfaces and perhaps in facilitating new methods for the fabrication of nano-structured surfaces. Future work could be extended to quantify the potential of mean force (PMF) between SWNTs under the influence of adsorbed surfactant molecules with different structures

and compositions (i.e., SWNTs covered by pure linear, pure branched, mixed linear and branched SDBS, CsDS, and SDS) in aqueous solution. Up till now, only limited studies have explored the SWNT-SWNT PMF. Various methods are available for such calculations, including umbellar sampling, force integration, among others. The umbellar sampling algorithm is commonly applied and reliable, however very time consuming. The force integration algorithm is becoming practice. In the latter approach, two parallel SWNTs are placed at decreasing SWNT-SWNT separations (e.g., every 0.1 nm from contact to ~ 3 nm). The individual PMF is calculated by integrating the average mean force over the separation distance, in which the repulsive potential energy barrier and the attractive potential energy (in terms of the long-range electrostatic repulsion, short-range vdW attraction, and the short-range steric repulsion) are described. Further study could use MD simulations to probe the properties and behaviour of surfactants and/or polymers mixtures stabilized aqueous SWNT dispersions. Moreover, other modelling and simulation techniques, including but not limited to, coarse-grained (CG) MD and DPD could be employed to examine the morphology of adsorbed surfactant aggregates on SWNTs at larger surfactant densities. To fill the knowledge gap concerning surfactant adsorption on heterogeneous surfaces, investigation could be carried out for the adsorption and aggregation of surfactants on hydrophobic stripes crossing each other perpendicularly (i.e., crossing stripes) and on hydrophobic steps. Results should be compared with those obtained for isolated stripes. Consideration would also be made for polymers because of their common and important use as nanofabrication templates in a range of applications, including advanced lithography, next generation batteries, high density magnetic storage media, etc.

Appendix A Supporting Information for Chapter 3

Table A-1: Non-bonded parameters

Atom/Group	σ [Å]	ϵ [kcal mol ⁻¹]	δ [e]
CH ₃	3.9300	0.2265	0.0000
CH ₂	3.9300	0.0934	0.0000
CH	3.3953	0.0934	0.0000
C* (in CH ₂ -C*-C-H)	3.4730	0.0951	-0.0556
C* (in CH-C*-C-H)	3.4730	0.0951	-0.0556
C* (in CH ₂ -C-C*-H)	3.4730	0.0951	-0.1133
C* (in CH-C-C*-H)	3.4730	0.0951	-0.1133
C* (in S-C*-C-H)	3.4730	0.0951	-0.1438
C* (in S-C-C*-H)	3.4730	0.0951	-0.0905
H* (in CH ₂ -C-C-H*)	2.8464	0.0152	0.0631
H* (in CH-C-C-H*)	2.8464	0.0152	0.0631
H* (in S-C-C-H*)	2.8464	0.0152	0.1069
S	3.5903	0.3440	1.1061
O	3.0332	0.0957	-0.6131
Na	2.8010	0.5000	+1.0000
H (in H ₂ O)	0.0000	0.0000	0.4238
O (in H ₂ O)	3.1660	0.1554	-0.8476
C (in SWNT)	3.4000	0.0557	0.0000

where σ is collision diameter, ϵ is well depth, and δ is partial charge.

Table A-2: Bond-stretching parameters

Bond	b_0 [Å]	k_b [kcal mol ⁻¹ Å ⁻²]
CH ₃ -CH ₂	1.540	260.000
CH ₂ -CH ₂	1.540	260.000
CH ₂ -CH	1.540	260.000
CH ₂ -C	1.460	350.000
CH-C	1.460	350.000
C-C	1.390	525.000
C-H	1.020	350.000
C-S	1.480	350.000
S-O	1.480	350.000
O-H	0.945	N/A

where b_0 is equilibrium value of bond length and k_b is force constant.

Table A-3: Angle-bending parameters

Angle	θ_0 [deg]	k_θ [kcal mol ⁻¹ rad ⁻²]
CH ₃ -CH ₂ -CH ₂	114.000	62.095
CH ₂ -CH ₂ -CH ₂	114.000	62.095
CH ₂ -CH-CH ₂	114.000	62.095
CH ₂ -CH ₂ -C	124.193	109.491
CH ₂ -CH-C	124.193	109.491
CH ₂ -C-C	124.193	109.491
CH-C-C	124.193	109.491
C-C-C	124.193	109.491
C-C-H	124.193	109.491
C-S-O	175.000	115.500
O-S-O	175.000	115.500

where θ_0 is equilibrium value of bond angle and k_θ is force constant.

Table A-4: Dihedral parameters

Dihedral	c_0	c_1	c_2	c_3
		[kcal mol ⁻¹]		
CH ₃ -CH ₂ -CH ₂ -CH ₂	7.6481	14.5396	1.1339	-23.3216
CH ₂ -CH ₂ -CH ₂ -CH ₂	7.6481	14.5396	1.1339	-23.3216
CH ₂ -CH-CH ₂ -CH ₂	7.6481	14.5396	1.1339	-23.3216
CH ₂ -CH ₂ -C-C	20.0840	0.0000	-20.0840	0.0000
CH ₂ -CH-C-C	20.0840	0.0000	-20.0840	0.0000
CH ₂ -C-C-H	20.0840	0.0000	-20.0840	0.0000
CH-C-C-H	20.0840	0.0000	-20.0840	0.0000
C-C-C-C	25.9400	0.0000	-25.9400	0.0000
C-C-C-H	35.1460	0.0000	-35.1460	0.0000
C-C-C-S	35.1460	0.0000	-35.1460	0.0000
H-C-C-H	35.1460	0.0000	-35.1460	0.0000
H-C-C-S	35.1460	0.0000	-35.1460	0.0000
C-C-S-O	8.3680	0.0000	-8.3680	0.0000

Dihedral angles were constrained through the Ryckaert and Bellemans potential: $U_{\text{dihedral}} = \sum_{k=0}^5 c_k \cos^k(\phi)$, where U_{dihedral} is the dihedral energy, c_k are the energy constants, and ϕ is the dihedral angle.

Table A-5: Simulation details for the systems considered

System	SWNT	No. of SDBS	No. of water	SDBS surface coverage	Simulation time
		[molecules]		[molecules per nm ²]	[ns]
Linear SDBS	(6,6)	19	24145	1.0	250
	(12,12)	38	23188	1.0	250
	(20,20)	63	21460	1.0	250
	(6,6)	53	23427	2.8	400
	(12,12)	106	21711	2.8	500
	(20,20)	178	18953	2.8	500
Branched SDBS	(6,6)	19	24107	1.0	250
	(12,12)	38	23172	1.0	250
	(20,20)	63	21468	1.0	250
	(6,6)	53	23418	2.8	500
	(12,12)	106	21684	2.8	400
	(20,20)	178	19022	2.8	400

Appendix B Supporting Information for Chapter 5

B.1 SDS surfactants self-assembled on (6,6) SWNTs

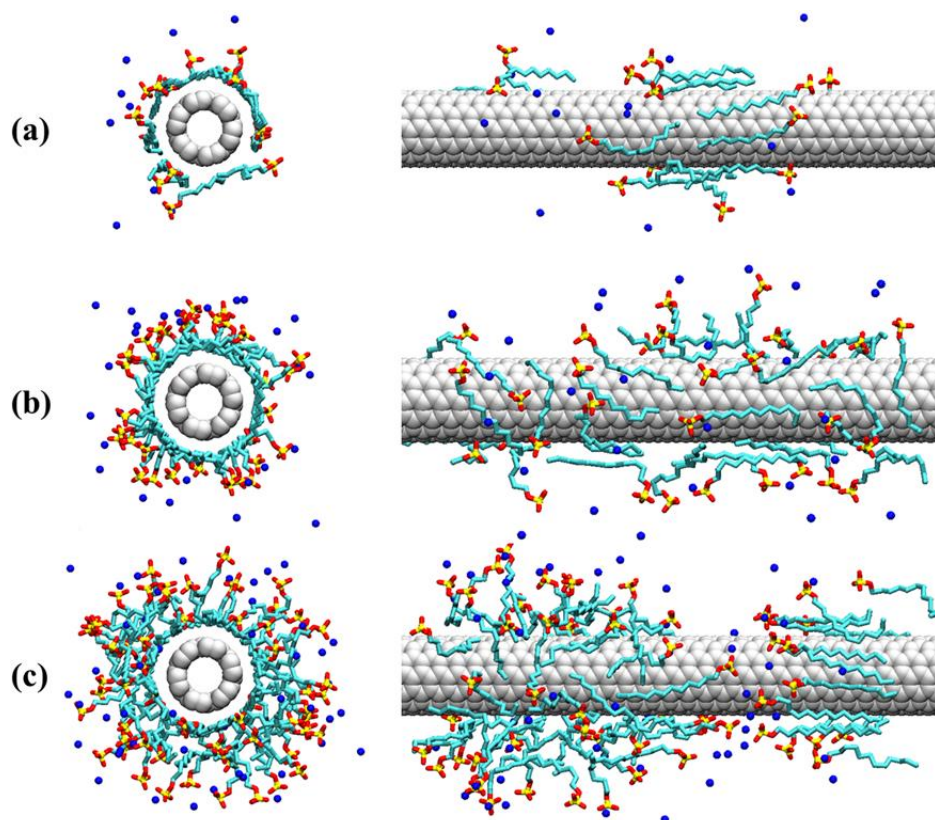


Figure B-1: Front (left) and side (right) views of representative simulation snapshots for SDS surfactant aggregates adsorbed on (6,6) SWNTs. In panels (a), (b), and (c) the nominal surfactant per surface area is 1.0, 2.3, and 4.0 molecules, respectively. Water molecules are not shown for clarity. Blue spheres are Na⁺ ions. Cyan spheres are either CH₂ or CH₃ groups in the surfactant tails. Red and yellow spheres are oxygen and sulphur atoms in the surfactant headgroups.

At surfactant surface coverage of 1.0 molecules/nm², SDS molecules wrap around the nanotube forming a ring. Some surfactant headgroups are positioned close to the hydrophobic SWNT surfaces (**Figure B-1a**). As the surface coverage increases, SDS surfactants form one layer structure, and the surfactant heads protrude into the aqueous solution (**Figure B-1b**). It was found bi-layered aggregates at the highest surfactant surface coverage considered (4.0 molecules/nm²). SDS surfactants were found to yield a

continuous first layer at contact with the nanotube surfaces with excess SDS molecules agglomerated on top of the first layer, yielding double-layered structures (**Figure B-1c**). Note that this behaviour is slightly different, albeit consistent, compared to that discussed in the previous work [41]. The multi-layered structures observed before were probably due to local minima in the free-energy landscape.

B.2 Effective surface area per surfactant headgroup

As discussed in **Chapter 5**, at the highest surface coverage considered (i.e., 4.0 molecules/nm²) a compact monolayer of CsDS surfactants wrapped around the three SWNTs was observed. The tail segments are positioned near the nanotube surfaces resulting from hydrophobic attractions. Most of the surfactant headgroups project into water. Details regarding the aggregate morphology are dependent on the nanotube diameter. On the (6,6) SWNT, all CsDS surfactants remained densely adsorbed on the nanotubes, and SDS surfactants yield rather disordered multi-layered structures. When (12,12) and (20,20) SWNTs were simulated, some of the surfactants initially in contact with the nanotubes desorbed yielding small aggregates, maybe micelles, in the aqueous phase at the nominal surfactant surface density of 4.0 molecules/nm² (**Figure B-2**). When the nominal surface density was of 2.3 molecules/nm², a few surfactants desorbed and formed micelles, but only in the case of (20,20) SWNT. This behaviour was also observed for SDS surfactant systems at similar coverages. The effective surface coverages of either CsDS or SDS surfactants on (12,12) and (20,20) SWNTs at the surface coverages of 2.3 and 4.0 molecules/nm² were quantified. The time-average number of surfactants adsorbed on the SWNT was calculated by integrating the number density profiles of the surfactant molecules around the SWNT to a cut-off distance of 10 Å. The results are summarised in **Table B-1**.

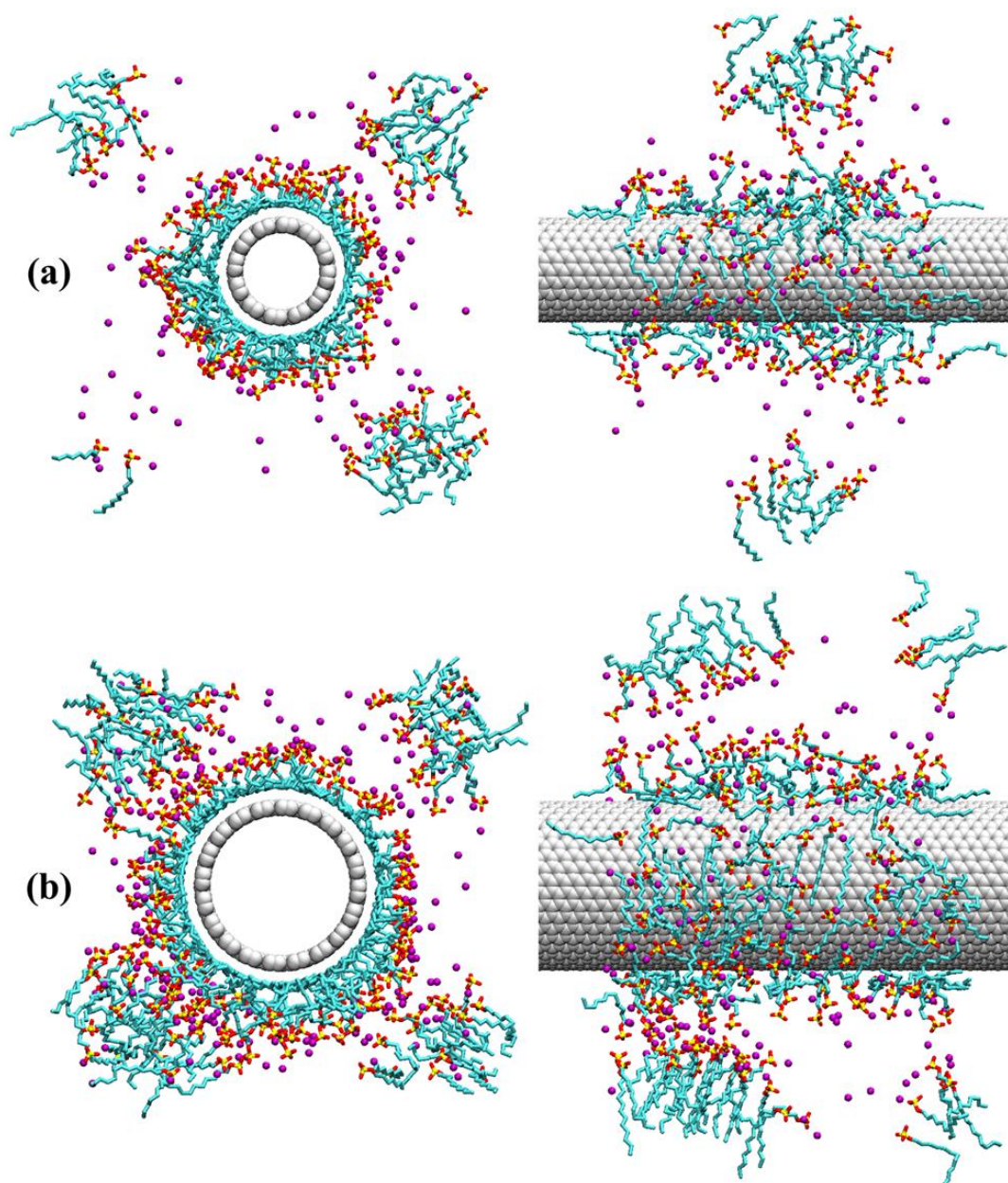


Figure B-2: Front (left) and side (right) views of representative simulation snapshots for CsDS surfactant aggregates adsorbed on SWNTs. The nominal surfactant per surface area is 4.0 molecules. Panels (a) and (b) are for (12,12) and (20,20) SWNTs, respectively. Water molecules are not shown for clarity. Purple spheres are Cs⁺ ions. Cyan spheres are either CH₂ or CH₃ groups in the surfactant tails. Red and yellow spheres are oxygen and sulphur atoms in the surfactant headgroups.

Table B-1: Effective surfactant surface coverage for CsDS and SDS surfactants adsorbed on SWNTs

Surfactant	SWNT	No. of surfactants simulated	Nominal surface coverage	No. of adsorbed [non-adsorbed] surfactants	Effective surface coverage
		[molecules]	[molecules per nm ²]	[molecules]	[molecules per nm ²]
CsDS	(12,12)	71	2.3	71 [0]	2.3
	(20,20)	119	2.3	82 [37]	1.6
	(12,12)	126	4.0	86 [40]	2.7
	(20,20)	210	4.0	124 [86]	2.4
SDS	(12,12)	71	2.3	71 [0]	2.3
	(20,20)	119	2.3	85 [34]	1.6
	(12,12)	126	4.0	90 [36]	2.9
	(20,20)	210	4.0	125 [85]	2.4

B.3 Radial density distributions of CsDS and SDS surfactants on (12,12) and (20,20) SWNTs

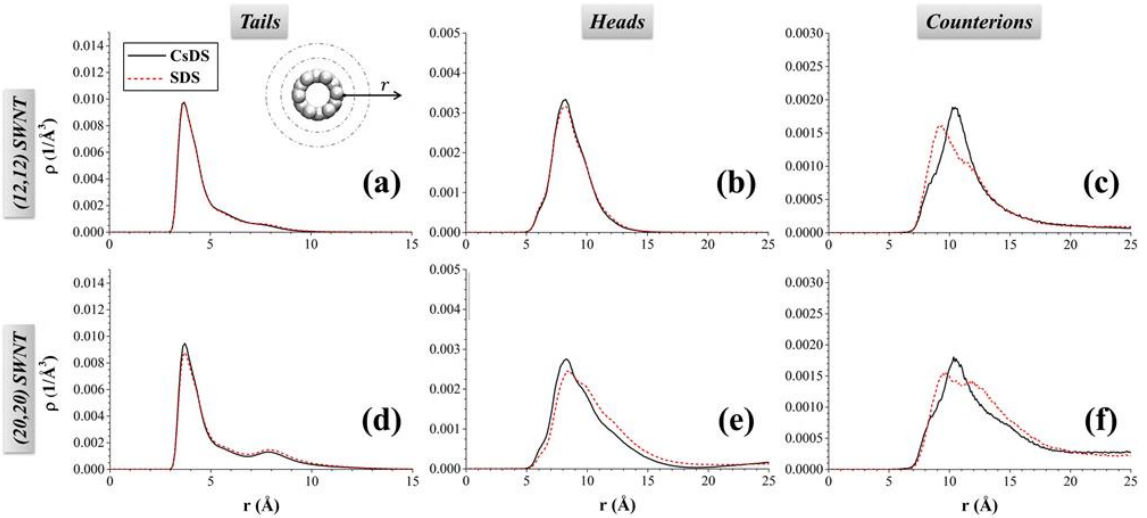


Figure B-3: Radial density distributions of (a, d) tail segments, (b, e) surfactant headgroups, and (c, f) counterions obtained on (12,12) (top panels) and (20,20) SWNTs (bottom panels). The nominal surfactant per surface area is 0.44 molecules. Blue-solid and red-dashed lines represent results obtained for CsDS and SDS systems, respectively.

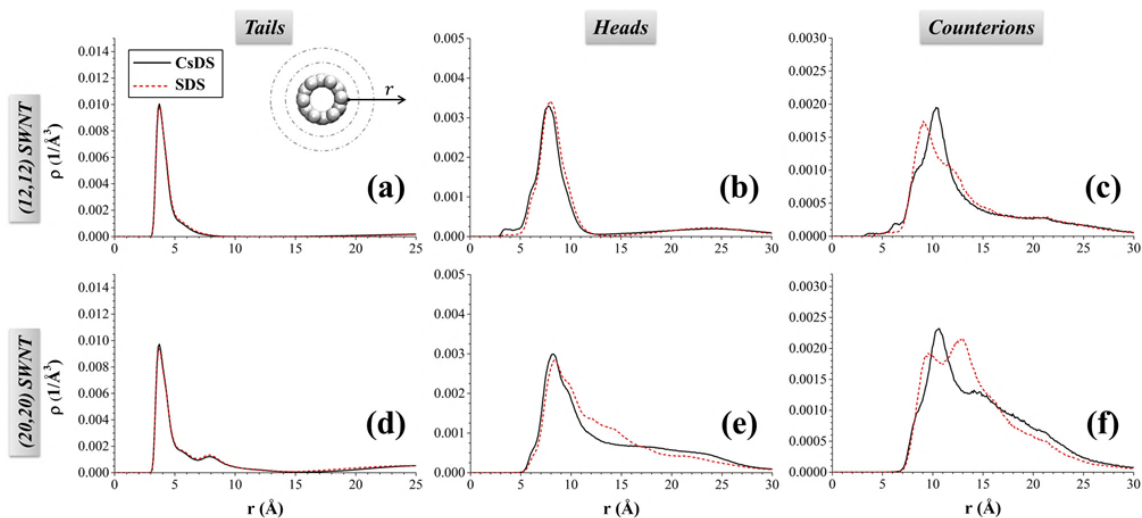


Figure B-4: Same as **Figure B-3** but for nominal surfactant per surface area of 4.0 molecules.

Density distributions of tail segments, surfactant headgroups, and counterions for CsDS and SDS surfactants on (12,12) and (20,20) SWNTs at nominal surface coverages of 2.3 and 4.0 molecules per nm^2 are shown in **Figure B-3** and **Figure B-4**, respectively. The results obtained for CsDS are similar to those obtained for SDS.

B.4 Orientation of adsorbed CsDS and SDS surfactants

To quantify the orientations both of CsDS and of SDS surfactants adsorbed on (6,6), (12,12), and (20,20) SWNT surfaces, the probability distribution of the angle between three vectors identified by one surfactant molecule and the SWNT axis was calculated. The three vectors considered are the tail-to-head vector, indicative of the overall orientation of the whole surfactant with respect to the carbon nanotube, the C12-to-C6 vector, indicative of the orientation of the surfactant hydrophobic tail, and the C5-to-S vector, which can be used to qualitatively understand how much the surfactant headgroup protrudes into the aqueous phase. A schematic for the three vectors is provided in **Figure B-5**. Note that when the angle between one of the three vectors and the SWNT axis is 0° or 180° , the vector is parallel to the nanotube axis, while when the angle is 90° , the vector is perpendicular to the nanotube axis.

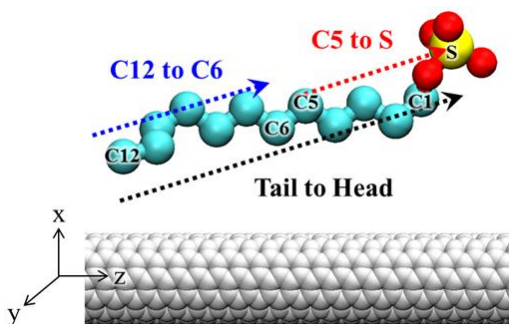


Figure B-5: Schematic representing the three vectors identified by one surfactant molecule that are used to study the surfactant orientation on the nanotube. For each surfactant, the tail-to-head vector, the C12-to-C6 vector in the tail, and the C5-to-S vector are identified.

The orientation distributions for CsDS and SDS molecules on (6,6) SWNTs at various surface coverages are shown in **Figure B-6**. For these calculations, only the surfactants adsorbed at contact with the nanotube surface (as defined by the radial cut-off distance 10 Å) were considered. The orientation distribution strongly depends on the surface coverage. At low surface coverage (top panels), both CsDS and SDS surfactants preferentially lie parallel to the nanotube axis. Cs⁺ counterions induce an orientation less parallel to the nanotube surface, which is particularly evident in the results of **Figure B-6c** (C5-to-S vector). As the surface coverage increases (middle and bottom panels), CsDS surfactants tend to yield more disordered structures compared to SDS ones (the angles distributions are much more distributed). The surfactant headgroups are much more pronouncedly projected towards the aqueous phase in the presence of Cs⁺ than in the presence of Na⁺ (see the preferential orientation centred around 90° for black-solid as opposed to red-dashed lines in **Figure B-6f** and **Figure B-6i**). In all cases, SDS surfactants preferentially lie parallel to the SWNT axis.

The orientation distributions for CsDS and SDS molecules on (12,12) and (20,20) SWNTs at nominal surface coverages of 2.3 and 4.0 molecules/nm² are shown in **Figure B-7** and **Figure B-8**, respectively. Note that only adsorbed surfactants were considered for these calculations. One surfactant was considered adsorbed if found within the radial cut-off distance of 10 Å from the nanotube surface. No significant differences were

observed when the Na^+ ions were replaced with Cs^+ ones, in agreement with other results discussed above.

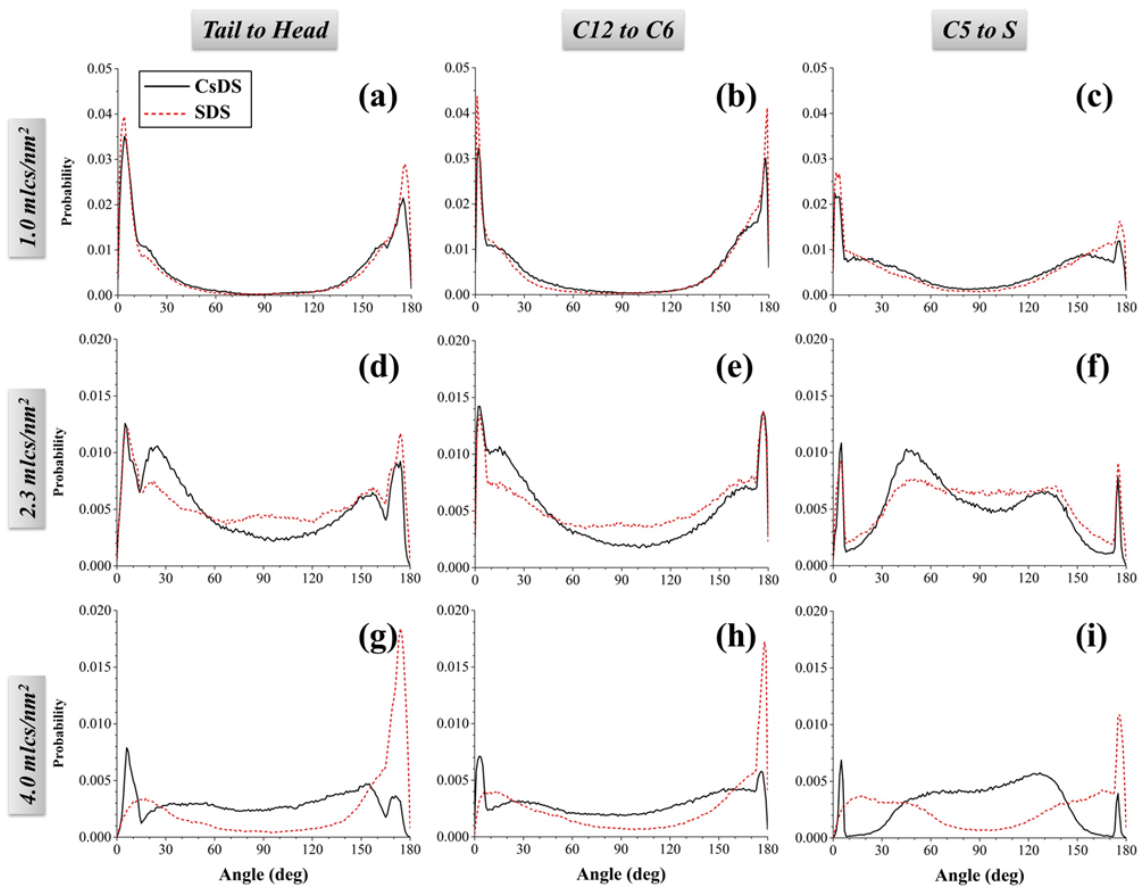


Figure B-6: Orientation probability distributions observed for CsDS (black-solid line) and SDS (red-dashed line) surfactants on (6,6) SWNTs. Left, middle, and right panels are for the angle formed between the surfactant head-to-tail vector, that formed between the C12-to-C6 vector, and that formed between the C5-to-S vector and the nanotube axis, respectively. Top, middle, and bottom panels are for results obtained for nominal surface coverages of 1.0, 2.3, and 4.0 molecules/nm², respectively.

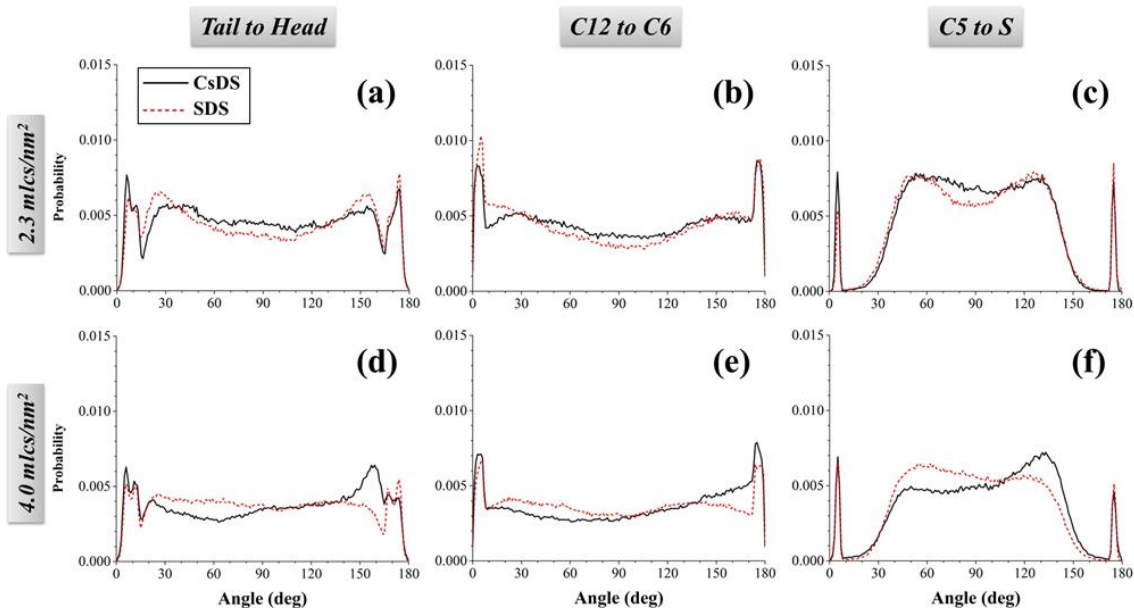


Figure B-7: Orientation probability distributions observed for CsDS (black-solid line) and SDS (red-dashed line) surfactants on (12,12) SWNTs. Left, middle, and right panels are for the angle formed between the surfactant tail-to-head vector, that formed between the C12-to-C6 vector, and that formed between the C5-to-S vector and the nanotube axis, respectively. Top and bottom panels are for results obtained for nominal surface coverages of 2.3 and 4.0 molecules/nm², respectively.

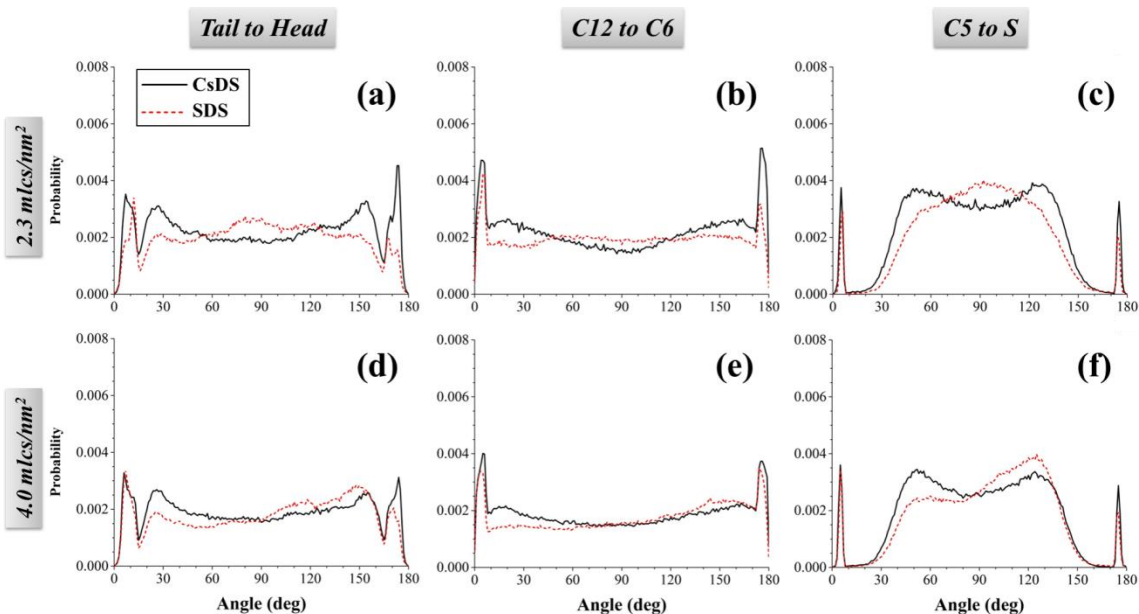


Figure B-8: Same as **Figure B-7** but for (20,20) SWNTs.

B.5 Experimental validation

The experiments were carried out by Carlos Silvera Batista and Jeffrey Fagan, National Institute of Standards and Technology, Materials Science and Engineering Division, Gaithersburg, MD 20899, USA.

Two sets of experimental samples were prepared using nanotubes with average diameters close to the (6,6) (NIST SWNT soot SRM 2483) [179] and the (12,12) (Hanwha Chemicals ASP-100F). The two samples are identified as ‘small diameter’ and ‘large diameter’ in the discussion below. For each set of samples, the nanotubes (0.1 mg mL^{-1}) were initially dispersed in the presence of 25 mM SDS via tip sonication. After sonication, the parent dispersion was used to create a series of samples containing 25 mM, 50 mM or 100 mM of either NaCl or CsCl salt, while maintaining the SDS concentration at 25 mM. All of the samples were 1:1 volumetric dilutions of the parent dispersion; an additional dilution with only SDS was also prepared so that comparison would be made on equal SWNT concentration samples. These samples were measured in a spectrophotometer to monitor for shifts in the absorbance spectra relative to the parent dispersion, and then centrifuged for 2 hours at an acceleration of $21000 \times 9.81 \text{ ms}^{-2}$ (small diameter sample) or for 90 minutes at an acceleration of $15000 \times 9.81 \text{ ms}^{-2}$ (large diameter sample, change due to equipment failure). Centrifugation of nanotube dispersion preferentially removes impurities and poorly dispersed nanotubes. After centrifugation the supernatant from each sample was carefully removed and the absorbance spectra measured.

It should be pointed out that, unfortunately, (6,6) and (12,12) SWNTs comprise relatively small percentages of the nanotube populations in the small and large diameter samples, respectively. This eliminates their utility for monitoring absorbance changes due to the salt addition, as the peaks are small and sit upon a large underlying absorbance feature. As an alternative metric to measure potential structural changes in the bound surfactant layer it can be monitored the effects of the salt addition on the absorbance of the similarly sized semiconducting species in each sample. For the small diameter nanotubes it can be identified a primary peak in the near-infrared region to be

the response of the (6,5) SWNT [diameter of (6,5) SWNT is 0.747 nm compared to 0.814 nm for (6,6) SWNT]. For the larger diameter sample the absorbance of the semiconducting feature is comprised of contributions from several SWNT species in the diameter range of the (12,12) SWNT.

To evaluate changes in the absorbance, two metrics were used, intensity of the optical transition, and the location of the optical transition relative to the parent sample. Both of these parameters have been demonstrated in the literature to be affected by the packing density of surfactant on the SWNT surfaces [229-233]. As previously reported, an increase in the optical transition strength is correlated with improved individualization of the nanotubes. It is also related, along with blue shifts (towards shorter wavelengths) of the peak position, to better isolation of the SWNT surface from the aqueous environment, which affects both properties through the effective dielectric environment experienced by the nanotube.

Addition of either NaCl or CsCl salt was found to measurably increase, by $\cong 10\%$, the intensity of the nanotube excitonic optical transitions relative to the SDS only sample for all samples prior to centrifugation. This can be seen in **Figure B-9**, in which the absorbance spectra of the small diameter (panel A) and the larger diameter samples (panel B) after the addition of salt to the dispersion are reported. Focusing on the peak absorbance in the near-infrared region (E_{11} optical transition for the small diameter SWNTs, E_{22} optical transition for the large diameter SWNTs), for the small diameter nanotube population the increase in peak intensity is consistently larger for CsCl, as compared to NaCl, at all concentrations; for the larger diameter nanotubes however, the increase was larger with 25 mM NaCl than for 25 mM CsCl.

As shown in **Figure B-10**, it is found that the locations of the peak features also shifted with the addition of salt to the two nanotube dispersions. In the case of the small diameter SWNTs the shift of the (6,5) peak is significantly larger for the addition of CsCl salt than for addition of NaCl salt. This result, combined with the greater increase in peak intensity of the optical transition for the small diameter nanotubes indicates that the Cs^+ ion is specifically acting to drive densification of the adsorbed surfactant layer

on the small diameter nanotubes beyond the non-specific effects of increasing the ionic strength of the solution. This is in direct correspondence to the simulation results demonstrating increased density of the surfactant coverage in the presence of the Cs⁺ ions. For the larger diameter nanotube population, however, the degree of the monitored peak shift and the peak intensity change are significantly less indicative of a specific ion effect.

Measurement of the supernatant absorbance after centrifugation determined similar trends in both sets of samples for the peak optical transition wavelength, and in the optical transition intensity scaled by the absorbance between peak features (at 785 nm and 800 nm for the small and large diameter samples, respectively) to account for concentration differences. This is shown in **Figure B-11**.

As mentioned above, centrifugation preferentially removes larger particles as well as dense impurities and poorly dispersed SWNTs. In all cases the intensity of the remaining peaks (scaled comparison) in the supernatants was significantly increased by the process, indicating selective retention of well dispersed nanotubes. Contrary to the results of the optical peak metrics however, a larger percentage of the dispersed mass, as measured by the absolute absorbance of the samples, was depleted for the CsCl added samples than for the NaCl added samples. These results are summarised in **Figure B-12**. It should be pointed out that the greatest retained mass for both diameter populations occurred in the absence of additional salt. This may indicate that many of the nanotubes in the original sample were not well individualised and that a denser adsorbed surfactant layer increased the effective density of the particles or allowed for additional attractive interactions.

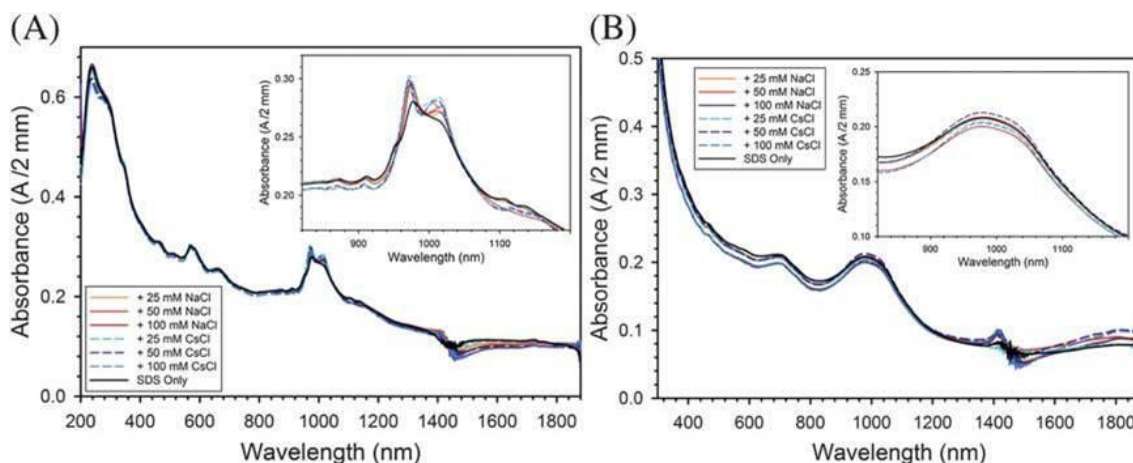


Figure B-9: UV-Vis-NIR absorbance spectra of the 25 mM SDS dispersed SWNTs with different amounts of added salt. Left: small diameter SWNTs. Inset: close up of (6,5) peak feature. Right: large diameter SWNT population. Inset: close up of E_{22} optical transition region for the large diameter population. The addition of salt induces more noticeable changes to the spectra of the small diameter SWNTs, particularly for the addition of CsCl.

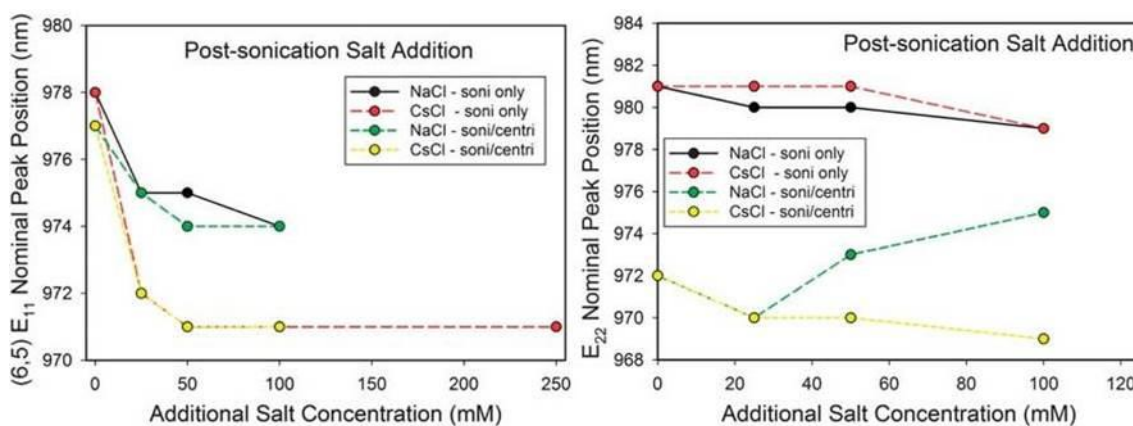


Figure B-10: Peak locations (shifts) as a function of salt addition. Left: small diameter SWNTs. Right: large diameter SWNT population.

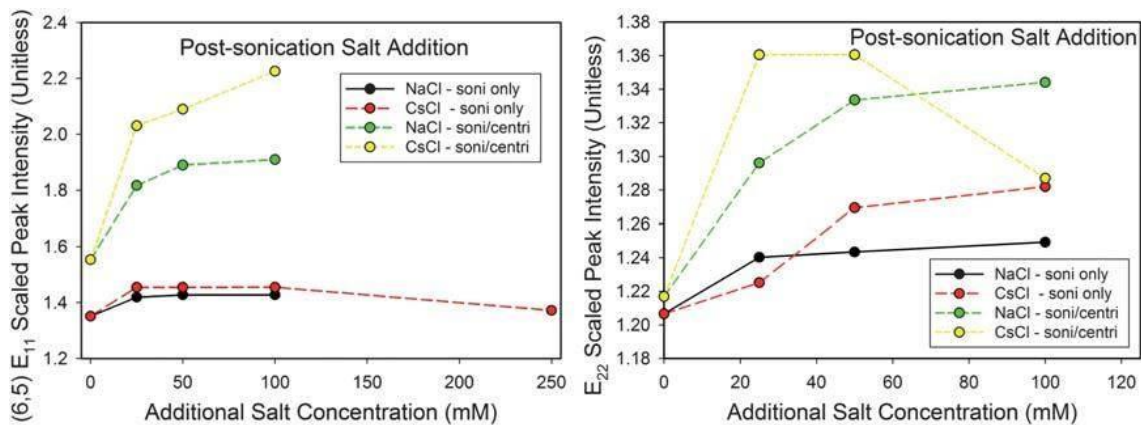


Figure B-11: Scaled peak intensity before and after centrifugation as a function of added salt concentration. Left: small diameter SWNTs. Right: large diameter SWNT population.

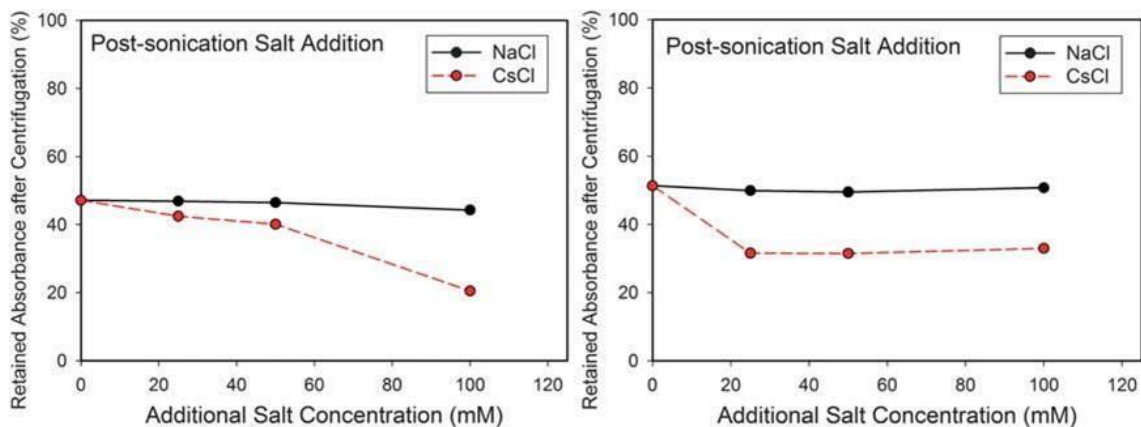


Figure B-12: Retained absorbance in the supernatant after centrifugation as a function of added salt concentration. Left: small diameter SWNTs, 785 nm. Right: large diameter SWNT population, 800 nm.

Appendix C Supporting Information for Chapter 6

C.1 Spring constant

In this study each surfactant consists of one bead for the head, and two beads for the tail. The three beads are connected by harmonic springs. The harmonic spring force (F_{ij}^S) is described as

$$F_{ij}^S = k_S(r_{ij} - r_0)\vec{n}_{ij} \quad (\text{C-1})$$

where r_{ij} is the relative displacement of beads i and j , \vec{n}_{ij} is the corresponding unit vector, k_S is the spring constant, and r_0 is the equilibrium bond length.

Because the van der Waals end-to-end length of one SDS molecule (L_S) is of 20.8 Å [234], r_0 is set equal to 10.4 Å. The approach of Denham *et al.* [235], who simulated non-ionic surfactants in water using DPD simulations, and suggested how to determine the optimal k_S was applied. Based on this protocol, k_S should be set to the lowest value that is able to maintain the average bond distance to r_0 .

A bulk simulation with surfactant concentration of 44.24 mM (370 surfactant molecules) was conducted in a $21 \times 21 \times 42 r_c^3$ rectangular box, for up to $\sim 0.31 \mu\text{s}$. Three simulations were conducted varying k_S from 4 (as suggested by Kuo *et al.* [189]) to 100 and $200 k_B T / r_c^2$. The average equilibrium bond length (\bar{r}_0) and its standard deviation (SD) for all surfactant bonds (740 bonds) were calculated and the data are summarised in **Table C-1**. The analysis indicates that when $k_S = 100 k_B T / r_c^2$ the bond length converges to r_0 with the SD of 1.2%.

Table C-1: The average bond length (\bar{r}_0) and standard deviation (SD) as a function of spring constant (k_S) = 4, 100, and 200 $k_B T/r_c^2$

k_S [$k_B T/r_c^2$]	\bar{r}_0 [Å]	SD [%]
4	12.73	16.5
100	10.23	1.2
200	10.18	1.5

C.2 Simulated system

Table C-2: Systems simulated for bulk studies

No. of surfactants [molecules]	Surfactant concentration [mM]
19	2.27
28	3.35
37	4.42
46	5.50
56	6.70
65	7.77
74	8.85
83	9.93
93	11.12
102	12.20
111	13.27
130	15.55
148	17.70
167	19.97
185	22.12
370	44.24
556	66.49
741	88.61
926	110.73
1111	132.85
1297	155.09
1482	177.22
1667	199.34
1852	221.46
2778	332.19
3704	442.92

Table C-3: Systems simulated for surfactant adsorption on a homogeneous hydrophobic (adsorbing) surface

No. of surfactants	Initial surfactant concentration	No. of surfactants adsorbed on the surface	Surfactant surface coverage	Surfactant concentration in the bulk obtained from non-adsorbed surfactants
[molecules]	[mM]	[molecules]	[molecules per nm ²]	[mM]
926	110.73	926	2.56	0.00
945	113.00	945	2.56	0.00
963	115.15	963	2.63	0.00
982	117.43	982	2.70	0.00
1000	119.58	1000	2.78	0.00
1019	121.85	1019	2.78	0.00
1037	124.00	1037	2.86	0.00
1056	126.28	1056	2.94	0.00
1074	128.43	1074	2.94	0.00
1093	130.70	1093	3.03	0.00
1111	132.85	1111	3.03	0.00
1130	135.12	1130	3.13	0.00
1148	137.28	1100	3.03	5.74
1167	139.55	1110	3.03	6.82
1185	141.70	1120	3.03	7.77
1204	143.97	1124	3.13	9.57
1222	146.13	1125	3.13	11.60
1241	148.40	1100	3.03	16.86
1259	150.55	1100	3.03	19.01
1278	152.82	1112	3.03	19.85
1297	155.09	1074	2.94	26.67
1482	177.22	1099	3.03	45.80
1667	199.34	1085	2.94	69.59
1852	221.46	1090	3.03	91.12

Table C-4: Systems simulated for surfactant adsorption on a homogeneous hydrophilic (surfactant-repelling) surface

No. of surfactants	Initial surfactant concentration	No. of surfactants adsorbed on the surface	Surfactant surface coverage	Surfactant concentration in the bulk obtained from non-adsorbed surfactants
[molecules]	[mM]	[molecules]	[molecules per nm ²]	[mM]
926	110.73	0	0	110.73
1852	221.46	0	0	221.46

Table C-5: Systems simulated for surfactant adsorption on one hydrophobic stripe

Stripe width L			Initial surfactant concentration	Simulation progress			Surfactant concentration in the bulk at equilibrium
				No. of surfactants adsorbed on the stripe	Surfactant concentration in the bulk	No. of surfactants added into (+) the system	
$[\tau_c]$	$[\text{\AA}]$	$[L_s]$	[mM]	[molecules]	[mM]	[molecules]	[mM]
0.35	3.18	0.15	21.52	1	21.40	N/A	21.40
			44.24	0	44.24	N/A	44.24
			110.73	1	110.61	N/A	110.61
0.70	6.36	0.31	28.70	45	23.32	N/A	23.32
			44.24	40	39.46	N/A	39.46
			110.73	41	105.83	N/A	105.83
1.05	9.54	0.46	28.70	48	22.96	N/A	22.96
			44.24	49	38.38	N/A	38.38
			110.73	45	105.35	N/A	105.35
1.40	12.72	0.61	44.24	189	21.64	0	21.64
1.75	15.90	0.76	44.24	185	22.12	0	22.12
2.10	19.08	0.92	44.24	195	20.93	0	20.93
2.45	22.26	1.07	44.24	190	21.52	0	21.52
			110.73	192	87.77	N/A	87.77
2.80	25.44	1.22	44.24	197	20.69	0	20.69
3.15	28.62	1.38	44.24	199	20.45	0	20.45
3.50	31.80	1.53	44.24	235	16.14	+ 55	22.72
			110.73	236	82.51	N/A	82.51
3.85	34.98	1.68	44.24	260	13.15	+ 70	21.52
			110.73	260	79.64	N/A	79.64
4.20	38.16	1.83	44.24	261	13.03	+ 70	21.40
			110.73	258	79.88	N/A	79.88
4.55	41.34	1.99	44.24	276	11.24	+ 100	23.20
			110.73	280	77.25	N/A	77.25
4.90	44.52	2.14	44.24	287	9.93	+ 100	21.88
			110.74	290	76.05	N/A	76.05

Table C-6: Systems simulated for surfactant adsorption on two hydrophobic stripes

Stripe width L	Separation distance D	Initial surfactant concentration	Simulation progress			Surfactant concentration in the bulk at equilibrium
			No. of surfactants adsorbed on the stripes	Surfactant concentration in the bulk	No. of surfactants added into (+) the system	
$[L_s]$	$[L_s]$	[mM]	[molecules]	[mM]	[molecules]	[mM]
0.46	0.15	44.24	210	19.13	+ 20	21.52
		110.73	208	85.86	N/A	85.86
	0.46	44.24	265	12.56	+ 80	22.12
		110.73	266	78.92	N/A	78.92
	0.76	44.24	370	0.00	+ 180	21.52
	1.07	44.24	370	0.00	+ 180	21.52
	1.38	44.24	370	32.17	+ 100	20.21
1.68	44.24	94	33.00	+ 100	21.05	
1.07	0.15	44.24	349	2.51	+ 160	21.64
		110.73	353	68.52	N/A	68.52
	0.46	44.24	357	1.55	+ 160	20.69
		110.73	354	68.40	N/A	68.40
1.68	0.15	44.24	370 [†]	0.00	+ 400	23.20
		110.73	576	41.85	N/A	41.85
	0.46	44.24	370 [‡]	0.00	+ 400	22.72
		110.73	577	41.73	N/A	41.73

^{†,‡} In order to maintain constant concentration in the bulk some surfactants were added into the systems, and the total number of surfactants adsorbed on two stripes for these two systems was 576 and 580 molecules, respectively.

Appendix D Supporting Information for Chapter 7

D.1 Self-assembled surfactant aggregates within fully hydrophobic trenches of width $L = 0.99L_s$, $1.91L_s$, and $3.75L_s$

Equilibrium simulation snapshots obtained in fully hydrophobic trenches of width $L = 0.99L_s$, $1.91L_s$, and $3.75L_s$ are shown in **Figure D-1**. From top to bottom the depth of the trench increases from $H = 0.61L_s$ to $6.42L_s$. When $L = 0.99L_s$, in the shallow trenches (**Figure D-1a**, **Figure D-1b**, and **Figure D-1c**) the self-assembled structures (i.e., monolayer, bilayer, and multilayer) are similar to those reported in $L = 1.30L_s$ (see **Figure 7-2**). As the trench depth increases further to $H = 6.42L_s$ (**Figure D-1d**), unexpectedly, at the bottom of the trench no evidence of a monolayer is found. Instead, it is observed hemi-spherical surfactant aggregates. In the region between the top and the bottom, the results suggest flat cylindrical micelles formed within the trench. Such aggregates can be seen clearly from the side view of simulation snapshot as shown in **Figure D-2**. The tails are found to orient parallel to the trench walls to maximise tail-hydrophobic surface interactions, while the surfactant heads are found outside of the micelle, where water is present. The results suggest that lateral confinement has a stronger effect in the deeper trenches. When L is twice the length of one surfactant molecule (i.e., $L = 1.91L_s$), confinement-induced structural transitions with changing the trench depth are not observed (**Figure D-1e** to **Figure D-1h**). The surfactants yield a flat monolayer on both walls of the trench with the water film in between. At the top of the trench the surfactants agglomerate strongly on the trench edges. In the wider trench (i.e., $L = 3.75L_s$) it can be seen that surfactants are assembled in a flat monolayer when $H = 0.61L_s$ (**Figure D-1i**). As the trench depth increases further, the surfactants yield a flat monolayer on both walls of the trench (**Figure D-1j**, **Figure D-1k**, and **Figure D-1l**). This aggregate is similar to those obtained in **Figure D-1f**, **Figure D-1g**, and **Figure D-1h**. At the bottom of the trench the surfactants compressed by these two monolayers form a hemi-cylindrical structure, with the tails at contact with the wall and the surfactant heads associated to water.

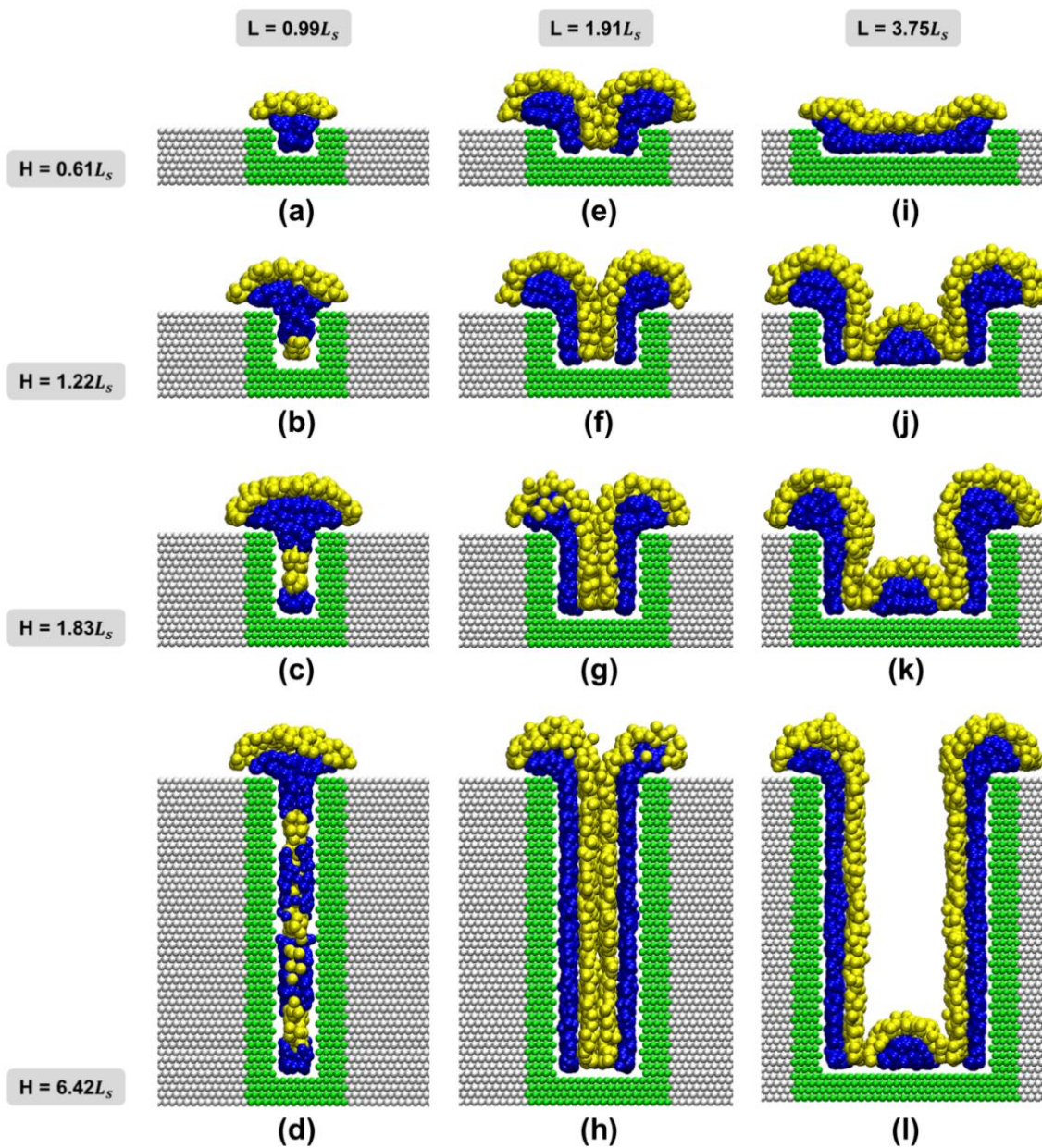


Figure D-1: Equilibrium simulation snapshots of self-assembled surfactant aggregates within fully hydrophobic trenches of varying width L and depth H . The results are obtained for trenches of width $L = 0.99L_s$, $1.91L_s$, and $3.75L_s$ (left to right panels) and depth $H = 0.61L_s$, $1.22L_s$, $1.83L_s$, and $6.42L_s$ (top to bottom panels). The surfactant head groups, the surfactant tail groups, the hydrophobic surface sites, and the surfactant-repelling surface sites are shown as yellow, blue, green and grey, respectively. For clarity, water beads are not shown, nor are surfactants present in the bulk, i.e., not adsorbed on the trenches. L is expressed in units of one surfactant length L_s , which is ~ 2.08 nm for sodium dodecyl sulphate [228].

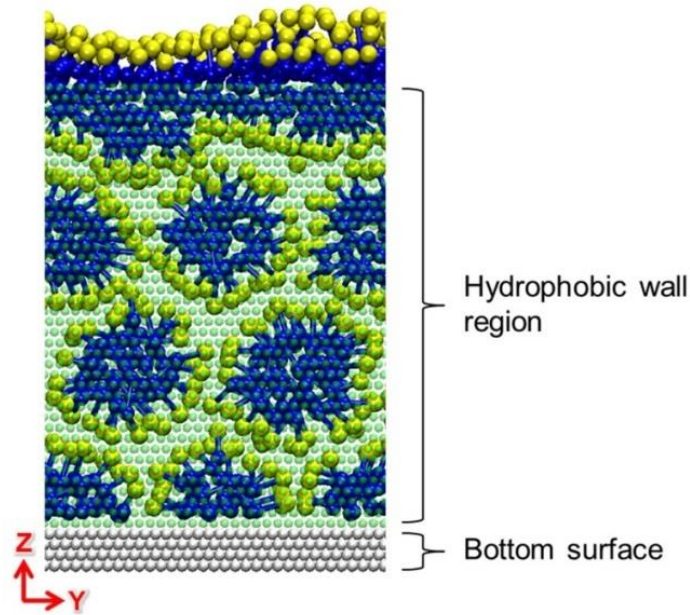


Figure D-2: Side view of equilibrium simulation snapshots of self-assembled surfactant aggregates in fully hydrophobic trenches of width $L = 0.99L_s$ and depth $H = 6.42L_s$. The colour code is the same as that used in **Figure D-1**. For clarity, water beads are not shown, nor are the surfactants present in the bulk.

D.2 Water-trench system

Simulations of water beads and trench were performed in order to quantify the behaviour of water near the structured surface. Trenches, both fully and partially hydrophobic, of width $L = 1.30L_s$ with varying $H = 0.61L_s$, $3.06L_s$, and $6.42L_s$ were considered. Water shows similar behaviour within all trenches. Shown in **Figure D-3** is a representative simulation snapshot and density profile of water beads within the fully hydrophobic trench of $L = 1.30L_s$ and $H = 3.06L_s$. Note that L is ~ 4 times the diameter of one water bead. The results show that water wets the trench. Above the top of the trench ($Z = \sim 3.6L_s$) water density reaches the constant value correspondent to the bulk density (~ 5 beads per r_c^3).

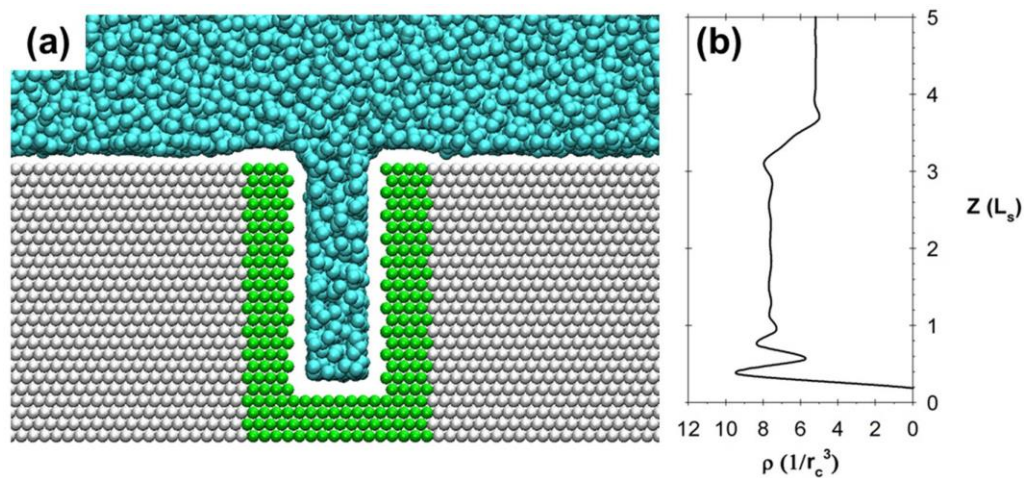


Figure D-3: (a) Representative simulation snapshot and (b) water density distribution for the system of water and fully hydrophobic trench of width $L = 1.30L_s$ and depth $H = 3.06L_s$. In panel (a), water beads, hydrophobic surface sites, and surfactant-repelling surface sites are shown in cyan, green, and grey, respectively. In panel (b), density of water beads is expressed in number of beads per r_c^3 and computed from the bottom trench surface along the Z direction. r_c is defined as a cubic volume of radius (cut-off radius) and is of 9.0856 \AA . Z is expressed in unit of one surfactant length (L_s).

Bibliography

- [1] D. Myers, in *The Organic Chemistry of Surfactants* (John Wiley & Sons, Inc., 2005), pp. 29-79.
- [2] A. Mohamed, T. Ardyani, S. A. Bakar, P. Brown, M. Hollamby, M. Sagisaka, and J. Eastoe, *Adv. Colloid Interface Sci.* **230**, 54 (2016).
- [3] H. Kato, A. Nakamura, and M. Horie, *RSC Adv.* **4**, 2129 (2014).
- [4] M. Suttipong and A. Striolo, *RSC Adv.* **5**, 90049 (2015).
- [5] M. Marquez, K. Patel, A. D. W. Carswell, D. W. Schmidtke, and B. P. Grady, *Langmuir* **22**, 8010 (2006).
- [6] M. Marquez, S. Kim, J. Jung, N. Truong, D. Teeters, and B. P. Grady, *Langmuir* **23**, 10008 (2007).
- [7] S. Hanumansetty and E. O'Rear, *Langmuir* **30**, 3665 (2014).
- [8] S. Iglauer, Y. Wu, P. Shuler, Y. Tang, and W. A. Goddard III, *J. Pet. Sci. Eng.* **71**, 23 (2010).
- [9] D. S. Bethune, C. H. Klang, M. S. de Vries, G. Gorman, R. Savoy, J. Vazquez, and R. Beyers, *Nature* **363**, 605 (1993).
- [10] H. Dai, *Acc. Chem. Res.* **35**, 1035 (2002).
- [11] C. Backes, in *Noncovalent Functionalization of Carbon Nanotubes: Fundamental Aspects of Dispersion and Separation in Water* (Springer Berlin Heidelberg, Berlin, Heidelberg, 2012) pp. 1-37.

- [12] S. Iijima and M. S. Dresselhaus, in *Carbon Nanotubes* (Pergamon, Oxford, 1996).
- [13] T. C. Dinadayalane and J. Leszczynski, in *Theoretical and Computational Chemistry*, edited by B. Balbuena Perla and M. Seminario Jorge (Elsevier, 2007), pp. 167-199.
- [14] M. S. Arnold, A. A. Green, J. F. Hulvat, S. I. Stupp, and M. C. Hersam, *Nat. Nanotechnol.* **1**, 60 (2006).
- [15] J. A. Fagan, C. Y. Khripin, C. A. Silvera Batista, J. R. Simpson, E. H. Háróz, A. R. Hight Walker, and M. Zheng, *Adv. Mater.* **26**, 2800 (2014).
- [16] J. A. Fagan, E. H. Háróz, R. Ihly, H. Gui, J. L. Blackburn, J. R. Simpson, S. Lam, A. R. Hight Walker, S. K. Doorn, and M. Zheng, *ACS Nano* **9**, 5377 (2015).
- [17] F. A. Lemasson, T. Strunk, P. Gerstel, F. Hennrich, S. Lebedkin, C. Barner-Kowollik, W. Wenzel, M. M. Kappes, and M. Mayor, *J. Am. Chem. Soc.* **133**, 652 (2010).
- [18] M. J. O'Connell, P. Boul, L. M. Ericson, C. Huffman, Y. Wang, E. Haroz, C. Kuper, J. Tour, K. D. Ausman, and R. E. Smalley, *Chem. Phys. Lett.* **342**, 265 (2001).
- [19] I. Pochorovski, H. L. Wang, J. I. Feldblyum, X. D. Zhang, A. L. Antaris, and Z. N. Bao, *J. Am. Chem. Soc.* **137**, 4328 (2015).
- [20] N. Minami, Y. Kim, K. Miyashita, S. Kazaoui, and B. Nalini, *Appl. Phys. Lett.* **88**, 093123 (2006).

- [21] L. Y. Yan, Y. F. Poon, M. B. Chan-Park, Y. Chen, and Q. Zhang, *J. Phys. Chem. C* **112**, 7579 (2008).
- [22] M. Zheng, A. Jagota, E. D. Semke, B. A. Diner, R. S. McLean, S. R. Lustig, R. E. Richardson, and N. G. Tassi, *Nat. Mater.* **2**, 338 (2003).
- [23] H. Cathcart, S. Quinn, V. Nicolosi, J. M. Kelly, W. J. Blau, and J. N. Coleman, *J. Phys. Chem. C* **111**, 66 (2007).
- [24] A. J. Blanch, C. E. Lenehan, and J. S. Quinton, *J. Phys. Chem. B* **114**, 9805 (2010).
- [25] R. Haggemueller, S. S. Rahatekar, J. A. Fagan, J. Chun, M. L. Becker, R. R. Naik, T. Krauss, L. Carlson, J. F. Kadla, P. C. Trulove, D. F. Fox, H. C. DeLong, Z. Fang, S. O. Kelley, and J. W. Gilman, *Langmuir* **24**, 5070 (2008).
- [26] M. F. Islam, E. Rojas, D. M. Bergey, A. T. Johnson, and A. G. Yodh, *Nano Lett.* **3**, 269 (2003).
- [27] O. Matarredona, H. Rhoads, Z. Li, J. H. Harwell, L. Balzano, and D. E. Resasco, *J. Phys. Chem. B* **107**, 13357 (2003).
- [28] T. J. McDonald, C. Engtrakul, M. Jones, G. Rumbles, and M. J. Heben, *J. Phys. Chem. B* **110**, 25339 (2006).
- [29] T. Okazaki, T. Saito, K. Matsuura, S. Ohshima, M. Yumura, and S. Iijima, *Nano Lett.* **5**, 2618 (2005).
- [30] Y. Tan and D. E. Resasco, *J. Phys. Chem. B* **109**, 14454 (2005).
- [31] K. Yurekli, C. A. Mitchell, and R. Krishnamoorti, *J. Am. Chem. Soc.* **126**, 9902 (2004).

- [32] V. C. Moore, M. S. Strano, E. H. Haroz, R. H. Hauge, R. E. Smalley, J. Schmidt, and Y. Talmon, *Nano Lett.* **3**, 1379 (2003).
- [33] L. Verlet, *Phys. Rev.* **159**, 98 (1967).
- [34] Z. Sun, V. Nicolosi, D. Rickard, S. D. Bergin, D. Aherne, and J. N. Coleman, *J. Phys. Chem. C* **112**, 10692 (2008).
- [35] A. Di Crescenzo, R. Germani, E. Del Canto, S. Giordani, G. Savelli, and A. Fontana, *Eur. J. Org. Chem.* **2011**, 5641 (2011).
- [36] S.-Y. Ju, J. Doll, I. Sharma, and F. Papadimitrakopoulos, *Nat. Nanotechnol.* **3**, 356 (2008).
- [37] T. Tanaka, Y. Urabe, D. Nishide, and H. Kataura, *J. Am. Chem. Soc.* **133**, 17610 (2011).
- [38] M. D. Clark, S. Subramanian, and R. Krishnamoorti, *J. Colloid Interface Sci.* **354**, 144 (2011).
- [39] U. Shigenori, K. Mamiko, H. Hiroaki, K. Hirofumi, T. Hideki, O. Takahiro, S. Hideki, A. Masahiko, and K. Katsumi, *Adv. Colloid Interface Sci.* **308**, 276 (2007).
- [40] H. Wang, *Curr. Opin. Colloid Interface Sci.* **14**, 364 (2009).
- [41] N. R. Tummala and A. Striolo, *ACS Nano* **3**, 595 (2009).
- [42] N. R. Tummala, B. H. Morrow, D. E. Resasco, and A. Striolo, *ACS Nano* **4**, 7193 (2010).
- [43] S. Lin and D. Blankschtein, *J. Phys. Chem. B* **114**, 15616 (2010).

- [44] M. Bystrzejewski, A. Huczko, H. Lange, T. Gemming, B. Büchner, and M. H. Rummeli, *J. Colloid Interface Sci.* **345**, 138 (2010).
- [45] J. G. Duque, C. G. Densmore, and S. K. Doorn, *J. Am. Chem. Soc.* **132**, 16165 (2010).
- [46] N. R. Tummala and A. Striolo, *J. Phys. Chem. B* **112**, 1987 (2008).
- [47] F. Tiberg, J. Brinck, and L. Grant, *Curr. Opin. Colloid Interface Sci.* **4**, 411 (1999).
- [48] M. Soria-Sánchez, A. Maroto-Valiente, A. Guerrero-Ruiz, and D. M. Nevskaja, *J. Colloid Interface Sci.* **343**, 194 (2010).
- [49] S. Manne and H. E. Gaub, *Science* **270**, 1480 (1995).
- [50] S. Manne, J. P. Cleveland, H. E. Gaub, G. D. Stucky, and P. K. Hansma, *Langmuir* **10**, 4409 (1994).
- [51] P. C. Ke, *PCCP* **9**, 439 (2007).
- [52] N. Mackiewicz, G. Surendran, H. Remita, B. Keita, G. Zhang, L. Nadjo, A. Hagege, E. Doris, and C. Mioskowski, *J. Am. Chem. Soc.* **130**, 8110 (2008).
- [53] M. R. Farrow, P. J. Camp, P. J. Dowding, and K. Lewtas, *PCCP* **15**, 11653 (2013).
- [54] N. R. Tummala and A. Striolo, *Phys. Rev. E* **80**, 021408 (2009).
- [55] J. M. Cases and F. Villieras, *Langmuir* **8**, 1251 (1992).
- [56] L. Macakova, E. Blomberg, and P. M. Claesson, *Langmuir* **23**, 12436 (2007).

- [57] H. C. Schniepp, H. C. Shum, D. A. Saville, and I. A. Aksay, *J. Phys. Chem. B* **111**, 8708 (2007).
- [58] H. C. Schniepp, H. C. Shum, D. A. Saville, and I. A. Aksay, *J. Phys. Chem. C* **112**, 14902 (2008).
- [59] S. Q. Wu, L. Shi, L. B. Garfield, R. F. Tabor, A. Striolo, and B. P. Grady, *Langmuir* **27**, 6091 (2011).
- [60] N. Kumar, S. Garoff, and R. D. Tilton, *Langmuir* **20**, 4446 (2004).
- [61] S. Paria and K. C. Khilar, *Adv. Colloid Interface Sci.* **110**, 75 (2004).
- [62] L. Mivehi, R. Bordes, and K. Holmberg, *Langmuir* **27**, 7549 (2011).
- [63] S. B. Velegol, B. D. Fleming, S. Biggs, E. J. Wanless, and R. D. Tilton, *Langmuir* **16**, 2548 (2000).
- [64] M. Suttipong, N. R. Tummala, A. Striolo, C. S. Batista, and J. Fagan, *Soft Matter* **9**, 3712 (2013).
- [65] N. R. Tummala and A. Striolo, *J. Phys. Chem. B* **112**, 1987 (2008).
- [66] R. E. Lamont and W. A. Ducker, *J. Am. Chem. Soc.* **120**, 7602 (1998).
- [67] R. Atkin, V. S. J. Craig, and S. Biggs, *Langmuir* **16**, 9374 (2000).
- [68] H. Domínguez, *Langmuir* **25**, 9006 (2009).
- [69] Z. Kiraly, G. H. Findenegg, E. Klumpp, H. Schlimper, and D. I., *Langmuir* **17**, 2420 (2001).
- [70] H. Domínguez, *J. Phys. Chem. B* **111**, 4054 (2007).

- [71] A. G. Hsieh, C. Punckt, S. Korkut, and I. A. Aksay, *J. Phys. Chem. B* **117**, 7950 (2013).
- [72] P. C. Pavan, E. L. Crepaldi, A. de, and J. B. Valim, *Colloid Surf. A-Physicochem. Eng. Asp.* **154**, 399 (1999).
- [73] J. Radulovic, K. Sefiane, and M. E. R. Shanahan, *J. Colloid Interface Sci.* **332**, 497 (2009).
- [74] J. C. Schulz and G. G. Warr, *Langmuir* **18**, 3191 (2002).
- [75] C. Gutig, B. P. Grady, and A. Striolo, *Langmuir* **24**, 4806 (2008).
- [76] D. Mütter, T. Shin, B. Demé, P. Fratzl, O. Paris, and G. H. Findenegg, *J. Phys. Chem. Lett.* **1**, 1442 (2010).
- [77] M. Sammalkorpi, A. Z. Panagiotopoulos, and M. Haataja, *J. Phys. Chem. B* **112**, 12954 (2008).
- [78] N. R. Tummala, B. P. Grady, and A. Striolo, *PCCP* **12**, 13137 (2010).
- [79] D. Frenkel and B. Smit, *Understanding Molecular Simulation: From Algorithms to Applications* 1st ed. (Academic Press: Orlando, FL, 1996).
- [80] D. Van Der Spoel, E. Lindahl, B. Hess, G. Groenhof, A. E. Mark, and H. J. C. Berendsen, *J. Comput. Chem.* **26**, 1701 (2005).
- [81] M. P. Allen and D. J. Tildesley, in *Computer Simulation of Liquids* (Clarendon Press, Oxford, 1987).
- [82] A. Cheng and W. A. Steele, *J. Chem. Phys.* **92**, 3867 (1990).
- [83] M. G. Martin and J. I. Siepmann, *J. Am. Chem. Soc.* **119**, 8921 (1997).

- [84] J. I. Siepmann, S. Karaborni, and B. Smit, *Nature* **365**, 330 (1993).
- [85] B. Smit, S. Karaborni, and J. I. Siepmann, *J. Chem. Phys.* **102**, 2126 (1995).
- [86] S. L. Mayo, B. D. Olafson, and W. A. Goddard, *J. Phys. Chem.* **94**, 8897 (1990).
- [87] S. S. Jang, S.-T. Lin, P. K. Maiti, M. Blanco, W. A. Goddard, P. Shuler, and Y. Tang, *J. Phys. Chem. B* **108**, 12130 (2004).
- [88] H. Dominguez and M. L. Berkowitz, *J. Phys. Chem. B* **104**, 5302 (2000).
- [89] K. J. Schweighofer, U. Essmann, and M. Berkowitz, *J. Phys. Chem. B* **101**, 3793 (1997).
- [90] D. E. Smith and L. X. Dang, *J. Chem. Phys.* **101**, 7873 (1994).
- [91] H. J. C. Berendsen, J. R. Grigera, and T. P. Straatsma, *J. Phys. Chem.* **91**, 6269 (1987).
- [92] E. Elbeltagi, T. Hegazy, and D. Grierson, *Adv. Eng. Inform.* **19**, 43 (2005).
- [93] R. D. Groot and P. B. Warren, *J. Chem. Phys.* **107**, 4423 (1997).
- [94] R. D. Groot and K. L. Rabone, *Biophys. J.* **81**, 725 (2001).
- [95] A. Maiti and S. McGrother, *J. Chem. Phys.* **120**, 1594 (2004).
- [96] E. Moeendarbary, T. Y. Ng, and M. Zangeneh, *Int. J. Appl. Mech.* **01**, 737 (2009).
- [97] P. J. Hoogerbrugge and J. Koelman, *Europhys. Lett.* **19**, 155 (1992).
- [98] J. M. V. A. Koelman and P. J. Hoogerbrugge, *Europhys. Lett.* **21**, 363 (1993).

- [99] R. D. Groot, T. J. Madden, and D. J. Tildesley, *J. Chem. Phys.* **110**, 9739 (1999).
- [100] E. S. Boek, P. V. Coveney, H. N. W. Lekkerkerker, and P. van der Schoot, *Phys. Rev. E* **55**, 3124 (1997).
- [101] J. C. Shelley and M. Y. Shelley, *Curr. Opin. Colloid Interface Sci.* **5**, 101 (2000).
- [102] N. Arai, K. Yasuoka, and X. C. Zeng, *J. Am. Chem. Soc.* **130**, 7916 (2008).
- [103] Y. Liu, C. Y. Yu, H. B. Jin, B. B. Jiang, X. Y. Zhu, Y. F. Zhou, Z. Y. Lu, and D. Y. Yan, *J. Am. Chem. Soc.* **135**, 4765 (2013).
- [104] P. Meakin and A. M. Tartakovsky, *Rev. Geophys.* **47**, RG3002 (2009).
- [105] I. V. Pivkin, B. Caswell, and G. E. Karniadakisa, in *Reviews in Computational Chemistry* (John Wiley & Sons, Inc., 2010) pp. 85-110.
- [106] J. R. Lu, Z. X. Li, R. K. Thomas, E. J. Staples, I. Tucker, and J. Penfold, *J. Phys. Chem.* **97**, 8012 (1993).
- [107] J. R. Partington, R. F. Hudson, and K. W. Bagnall, *Nature* **169**, 583 (1952).
- [108] B. Bhushan, in *Springer handbook of nanotechnology* (Springer, Berlin; New York, 2006).
- [109] L. A. Girifalco, M. Hodak, and R. S. Lee, *Phys. Rev. B* **62**, 13104 (2000).
- [110] V. A. Davis, A. N. G. Parra-Vasquez, M. J. Green, P. K. Rai, N. Behabtu, V. Prieto, R. D. Booker, J. Schmidt, E. Kesselman, W. Zhou, H. Fan, W. W. Adams, R. H. Hauge, J. E. Fischer, Y. Cohen, Y. Talmon, R. E. Smalley, and M. Pasquali, *Nat. Nanotechnol.* **4**, 830 (2009).

- [111] A. N. G. Parra-Vasquez, N. Behabtu, M. J. Green, C. L. Pint, C. C. Young, J. Schmidt, E. Kesselman, A. Goyal, P. M. Ajayan, Y. Cohen, Y. Talmon, R. H. Hauge, and M. Pasquali, *ACS Nano* **4**, 3969 (2010).
- [112] S. Ramesh, L. M. Ericson, V. A. Davis, R. K. Saini, C. Kittrell, M. Pasquali, W. E. Billups, W. W. Adams, R. H. Hauge, and R. E. Smalley, *J. Phys. Chem. B* **108**, 8794 (2004).
- [113] S. D. Bergin, Z. Sun, P. Streich, J. Hamilton, and J. N. Coleman, *J. Phys. Chem. C* **114**, 231 (2009).
- [114] J. Zhao, H. Park, J. Han, and J. P. Lu, *J. Phys. Chem. B* **108**, 4227 (2004).
- [115] N. Grossiord, P. van der Schoot, J. Meuldijk, and C. E. Koning, *Langmuir* **23**, 3646 (2007).
- [116] S. Utsumi, M. Kanamaru, H. Honda, H. Kanoh, H. Tanaka, T. Ohkubo, H. Sakai, M. Abe, and K. Kaneko, *Adv. Colloid Interface Sci.* **308**, 276 (2007).
- [117] Z. Xu, X. Yang, and Z. Yang, *Nano Lett.* **10**, 985 (2010).
- [118] X. He, O. Guvench, A. D. MacKerell, and M. L. Klein, *J. Phys. Chem. B* **114**, 9787 (2010).
- [119] P. Angelikopoulos and H. Bock, *Langmuir* **26**, 899 (2009).
- [120] M. Calvaresi, M. Dallavalle, and F. Zerbetto, *Small* **5**, 2191 (2009).
- [121] D. Kunzel, T. Markert, Gro, and D. M. Benoit, *PCCP* **11**, 8867 (2009).
- [122] B. Hess, C. Kutzner, D. van der Spoel, and E. Lindahl, *J. Chem. Theory Comput.* **4**, 435 (2008).

- [123] W. G. Hoover, *Phys. Rev. A* **31**, 1695 (1985).
- [124] U. Essmann, L. Perera, M. L. Berkowitz, T. Darden, H. Lee, and L. G. Pedersen, *J. Chem. Phys.* **103**, 8577 (1995).
- [125] J. Määttä, S. Vierros, and M. Sammalkorpi, *J. Phys. Chem. B* **119**, 4020 (2015).
- [126] T. Hertel, A. Hagen, V. Talalaev, K. Arnold, F. Hennrich, M. Kappes, S. Rosenthal, J. McBride, H. Ulbricht, and E. Flahaut, *Nano Lett.* **5**, 511 (2005).
- [127] E. A. Whitsitt and A. R. Barron, *Nano Lett.* **3**, 775 (2003).
- [128] B. Fang, G. Martyna, and Y. F. Deng, *Comput. Phys. Commun.* **177**, 362 (2007).
- [129] W. Wenseleers, I. I. Vlasov, E. Goovaerts, E. D. Obraztsova, A. S. Lobach, and A. Bouwen, *Adv. Funct. Mater.* **14**, 1105 (2004).
- [130] F. Bonaccorso, T. Hasan, P. H. Tan, C. Sciascia, G. Privitera, G. Di Marco, P. G. Gucciardi, and A. C. Ferrari, *J. Phys. Chem. C* **114**, 17267 (2010).
- [131] A. Di Crescenzo, S. Cambré, R. Germani, P. Di Profio, and A. Fontana, *Langmuir* **30**, 3979 (2014).
- [132] H. Wang, W. Zhou, D. L. Ho, K. I. Winey, J. E. Fischer, C. J. Glinka, and E. K. Hobbie, *Nano Lett.* **4**, 1789 (2004).
- [133] C. Fantini, J. Cassimiro, V. S. T. Peressinotto, F. Plentz, A. G. Souza Filho, C. A. Furtado, and A. P. Santos, *Chem. Phys. Lett.* **473**, 96 (2009).
- [134] S. Niyogi, S. Boukhalfa, S. B. Chikkannanavar, T. J. McDonald, M. J. Heben, and S. K. Doorn, *J. Am. Chem. Soc.* **129**, 1898 (2007).

- [135] S. Niyogi, C. G. Densmore, and S. K. Doorn, *J. Am. Chem. Soc.* **131**, 1144 (2009).
- [136] S. Ou, S. Patel, and B. A. Bauer, *J. Phys. Chem. B* **116**, 8154 (2012).
- [137] B. White, S. Banerjee, S. O'Brien, N. J. Turro, and I. P. Herman, *J. Phys. Chem. C* **111**, 13684 (2007).
- [138] S. Lin, A. J. Hilmer, J. D. Mendenhall, M. S. Strano, and D. Blankschtein, *J. Am. Chem. Soc.* **134**, 8194 (2012).
- [139] C. Shih, S. Lin, M. S. Strano, and D. Blankschtein, *J. Phys. Chem. C* **119**, 1047 (2015).
- [140] M. Suttipong, N. R. Tummala, B. Kitiyanan, and A. Striolo, *J. Phys. Chem. C* **115**, 17286 (2011).
- [141] B. Hess, C. Kutzner, D. van der Spoel, and E. Lindahl, *J. Chem. Theory Comput.* **4**, 435 (2008).
- [142] A. Cheng and W. A. Steele, *J. Chem. Phys.* **92**, 3867 (1990).
- [143] J. I. Siepmann, S. Karaborni, and B. Smit, *Nature* **365**, 330 (1993).
- [144] B. Smit, S. Karaborni, and J. I. Siepmann, *J. Chem. Phys.* **102**, 2126 (1995).
- [145] S. L. Mayo, B. D. Olafson, and W. A. Goddard, *J. Phys. Chem.* **94**, 8897 (1990).
- [146] H. J. C. Berendsen, J. R. Grigera, and T. P. Straatsma, *J. Phys. Chem.* **91**, 6269 (1987).
- [147] B. Sohrabi, N. Poorgholami-Bejarpasi, and N. Nayeri, *J. Phys. Chem. B* **118**, 3094 (2014).

- [148] T. Yang, S. Berber, J. F. Liu, G. P. Miller, and D. Tomanek, *J. Chem. Phys.* **128** (2008).
- [149] K. Younge, C. Christenson, A. Bohara, J. Crnkovic, and P. Saulnier, *Am. J. Phys.* **72**, 1247 (2004).
- [150] R. H. Baughman, A. A. Zakhidov, and W. A. de Heer, *Science* **297**, 787 (2002).
- [151] R. Van Noorden, *Nature* **469**, 14 (2011).
- [152] E. Nativ-Roth, R. J. Nap, I. Szleifer, and R. Yerushalmi-Rozen, *Soft Matter* **6** 5289 (2010).
- [153] R. W. Hockney, S. P. Goel, and J. W. Eastwood, *J. Comput. Phys.* **14**, 148 (1974).
- [154] U. Essmann, *J. Chem. Phys.* **103**, 8577 (1995).
- [155] W. H. Duan, Q. Wang, and F. Collins, *Chem. Sci.* **2**, 1407 (2011).
- [156] R. Butler, I. Hopkinson, and A. I. Cooper, *J. Am. Chem. Soc.* **125**, 14473 (2003).
- [157] M. L. Campbell, D. L. Apodaca, M. Z. Yates, T. M. McCleskey, and E. R. Birnbaum, *Langmuir* **17**, 5458 (2001).
- [158] K. Ghosh, S. M. Vyas, H. J. Lehmler, S. E. Rankin, and B. L. Knutson, *J. Phys. Chem. B* **111**, 363 (2007).
- [159] J. P. Hanrahan, M. P. Copley, K. M. Ryan, T. R. Spalding, M. A. Morris, and J. D. Holmes, *Chem. Mat.* **16**, 424 (2004).
- [160] I. U. Vakarelski, S. C. Brown, Y. I. Rabinovich, and B. M. Moudgil, *Langmuir* **20**, 1724 (2004).

- [161] K. M. K. Yu, A. M. Steele, J. Zhu, Q. J. Fu, and S. C. Tsang, *J. Mater. Chem.* **13**, 130 (2003).
- [162] F. Tiberg, B. Jonsson, and B. Lindman, *Langmuir* **10**, 3714 (1994).
- [163] F. Tiberg, B. Jonsson, J. Tang, and B. Lindman, *Langmuir* **10**, 2294 (1994).
- [164] R. Atkin, V. S. J. Craig, E. J. Wanless, and S. Biggs, *Adv. Colloid Interface Sci.* **103**, 219 (2003).
- [165] S. Manne and H. E. Gaub, *Science* **270**, 1480 (1995).
- [166] S. Manne, J. P. Cleveland, H. E. Gaub, G. D. Stucky, and P. K. Hansma, *Langmuir* **10**, 4409 (1994).
- [167] P. M. Karlsson, A. E. C. Palmqvist, and K. Holmberg, *Langmuir* **24**, 13414 (2008).
- [168] S. O. Nielsen, G. Srinivas, C. F. Lopez, and M. L. Klein, *Phys. Rev. Lett.* **94**, 228301 (2005).
- [169] K. Shah, P. Chiu, and S. B. Sinnott, *J. Colloid Interface Sci.* **296**, 342 (2006).
- [170] T. Zehl, A. Wahab, P. Schiller, and H. J. Mogel, *Langmuir* **25**, 2090 (2009).
- [171] Z. J. Xu, X. N. Yang, and Z. Yang, *J. Phys. Chem. B* **112**, 13802 (2008).
- [172] X. R. Zhang, B. H. Chen, and Z. H. Wang, *J. Colloid Interface Sci.* **313**, 414 (2007).
- [173] U. Reimer, M. Wahab, P. Schiller, and H. J. Mogel, *Langmuir* **17**, 8444 (2001).

- [174] H. Dominguez, A. G. Goicochea, N. Mendoza, and J. Alejandre, *J. Colloid Interface Sci.* **297**, 370 (2006).
- [175] K. Shah, P. Chiu, M. Jain, J. Fortes, B. Moudgil, and S. Sinnott, *Langmuir* **21**, 5337 (2005).
- [176] G. Srinivas, S. O. Nielsen, P. B. Moore, and M. L. Klein, *J. Am. Chem. Soc.* **128**, 848 (2006).
- [177] J. Foisner, A. Glaser, T. Leitner, H. Hoffmann, and G. Friedbacher, *Langmuir* **20**, 2701 (2004).
- [178] H. C. Schniepp, H. C. Shum, D. A. Saville, and I. A. Aksay, *J. Phys. Chem. B* **111**, 8708 (2007).
- [179] S. Wu, L. Shi, L. B. Garfield, R. F. Tabor, A. Striolo, and B. P. Grady, *Langmuir* **27**, 6091 (2011).
- [180] U. Reimer, M. Wahab, P. Schiller, and H. J. Mogel, *Langmuir* **21**, 1640 (2005).
- [181] X. R. Zhang, B. H. Chen, W. Dong, and W. C. Wang, *Langmuir* **23**, 7433 (2007).
- [182] A. Striolo, *J. Chem. Phys.* **125**, 094709 (2006).
- [183] N. R. Tummala, B. P. Grady, and A. Striolo, *PCCP* **12**, 13137 (2010).
- [184] S. Plimpton, *J. Comput. Phys.* **117**, 1 (1995).
- [185] E. Moeendarbary, T. Y. Ng, and M. Zangeneh, *Int. J. Appl. Mech.* **1**, 737 (2009).
- [186] R. Nagarajan and C. C. Wang, *Langmuir* **16**, 5242 (2000).

- [187] H. Zhao and K. L. Nagy, *Adv. Colloid Interface Sci.* **274**, 613 (2004).
- [188] N. Denham, M. C. Holmes, and A. V. Zvelindovsky, *J. Phys. Chem. B* **115**, 1385 (2011).
- [189] M. Y. Kuo, H. C. Yang, C. Y. Hua, C. L. Chen, S. Z. Mao, F. Deng, H. H. Wang, and Y. R. Du, *ChemPhysChem* **5**, 575 (2004).
- [190] K. J. Mysels, *Langmuir* **2**, 423 (1986).
- [191] P. H. Elworthy and K. J. Mysels, *J. Colloid Interface Sci.* **21**, 331 (1966).
- [192] B. Cabane, R. Duplessix, and T. Zemb, *J. Physique* **46**, 2161 (1985).
- [193] S. Jalili and M. Akhavan, *Colloid Surf. A-Physicochem. Eng. Asp.* **352**, 99 (2009).
- [194] C. D. Bruce, M. L. Berkowitz, L. Perera, and M. D. E. Forbes, *J. Phys. Chem. B* **106**, 3788 (2002).
- [195] A. D. Mackerell, *J. Phys. Chem.* **99**, 1846 (1995).
- [196] D. N. LeBard, B. G. Levine, P. Mertmann, S. A. Barr, A. Jusufi, S. Sanders, M. L. Klein, and A. Z. Panagiotopoulos, *Soft Matter* **8**, 2385 (2012).
- [197] S. A. Sanders, M. Sammalkorpi, and A. Z. Panagiotopoulos, *J. Phys. Chem. B* **116**, 2430 (2012).
- [198] F. Tiberg, B. Joansson, J.-a. Tang, and B. Lindman, *Langmuir* **10**, 2294 (1994).
- [199] F. Tiberg, B. Joesson, and B. Lindman, *Langmuir* **10**, 3714 (1994).
- [200] C. Gutig, B. P. Grady, and A. Striolo, *Langmuir* **24**, 4806 (2008).

- [201] D. Johannsmann, I. Reviakine, E. Rojas, and M. Gallego, *Anal. Chem.* **80**, 8891 (2008).
- [202] F. X. Zheng, X. R. Zhang, W. C. Wang, and W. Dong, *Langmuir* **22**, 11214 (2006).
- [203] L. M. Grant, T. Ederth, and F. Tiberg, *Langmuir* **16**, 2285 (2000).
- [204] L. M. Grant and W. A. Ducker, *J. Phys. Chem. B* **101**, 5337 (1997).
- [205] R. Huang, R. P. Carney, F. Stellacci, and B. L. T. Lau, *Nanoscale* **5**, 6928 (2013).
- [206] M. Iijima, M. Kobayakawa, M. Yamazaki, Y. Ohta, and H. Kamiya, *J. Am. Chem. Soc.* **131**, 16342 (2009).
- [207] M. Lotya, Y. Hernandez, P. J. King, R. J. Smith, V. Nicolosi, L. S. Karlsson, F. M. Blighe, S. De, Z. M. Wang, I. T. McGovern, G. S. Duesberg, and J. N. Coleman, *J. Am. Chem. Soc.* **131**, 3611 (2009).
- [208] X. Y. Gong, J. Liu, S. Baskaran, R. D. Voise, and J. S. Young, *Chem. Mat.* **12**, 1049 (2000).
- [209] A. Yamaguchi, F. Uejo, T. Yoda, T. Uchida, Y. Tanamura, T. Yamashita, and N. Teramae, *Nat. Mater.* **3**, 337 (2004).
- [210] C. H. See and J. O'Haver, *J. Appl. Polym. Sci.* **89**, 36 (2003).
- [211] H. Jung, C. K. Dalal, S. Kuntz, R. Shah, and C. P. Collier, *Nano Lett.* **4**, 2171 (2004).
- [212] C. W. Wu, T. Aoki, and M. Kuwabara, *Nanotechnology* **15**, 1886 (2004).

- [213] J. M. Cases and F. Villieras, *Langmuir* **8**, 1251 (1992).
- [214] F. A. M. Leermakers, L. K. Koopal, W. J. Lokar, and W. A. Ducker, *Langmuir* **21**, 11534 (2005).
- [215] L. Lajtar, J. Narkiewicz-michalek, W. Rudzinski, and S. Partyka, *Langmuir* **9**, 3174 (1993).
- [216] J. Narkiewicz-michalek, W. Rudzinski, and S. Partyka, *Langmuir* **9**, 2630 (1993).
- [217] M. Suttipong, B. P. Grady, and A. Striolo, *PCCP* **16**, 16388 (2014).
- [218] H. C. Schniepp, H. C. Shum, D. A. Saville, and I. A. Aksay, *J. Phys. Chem. B* **111**, 8708 (2007).
- [219] H. C. Schniepp, H. C. Shum, D. A. Saville, and I. A. Aksay, *J. Phys. Chem. C* **112**, 14902 (2008).
- [220] N. R. Tummala and A. Striolo, *J. Phys. Chem. B* **112**, 1987 (2008).
- [221] J. Y. Park, Y. B. Qi, P. D. Ashby, B. L. M. Hendriksen, and M. Salmeron, *J. Chem. Phys.* **130**, 114705 (2009).
- [222] Y. Qi, I. Ratera, J. Y. Park, P. D. Ashby, S. Y. Quek, J. B. Neaton, and M. Salmeron, *Langmuir* **24**, 2219 (2008).
- [223] X.-L. Yin, L.-J. Wan, Z.-Y. Yang, and J.-Y. Yu, *Appl. Surf. Sci.* **240**, 13 (2005).
- [224] S. O. Nielsen, C. F. Lopez, G. Srinivas, and M. L. Klein, *J. Phys.-Condes. Matter* **16**, R481 (2004).
- [225] H. Fan and A. Striolo, *Soft Matter* **8**, 9533 (2012).

- [226] X. C. Luu, J. Yu, and A. Striolo, *J. Phys. Chem. B* **117**, 13922 (2013).
- [227] J. R. Lu, Z. X. Li, R. K. Thomas, E. J. Staples, I. Tucker, and J. Penfold, *J. Phys. Chem.* **97**, 8012 (1993).
- [228] H. T. Zhao and K. L. Nagy, *J. Colloid Interface Sci.* **274**, 613 (2004).
- [229] J. H. Choi and M. S. Strano, *Appl. Phys. Lett.* **90**, 223114 (2007).
- [230] S.-Y. Ju, W. P. Kopcha, and F. Papadimitrakopoulos, *Science* **323**, 1319 (2009).
- [231] B. A. Larsen, P. Deria, J. M. Holt, I. N. Stanton, M. J. Heben, M. J. Therien, and J. L. Blackburn, *J. Am. Chem. Soc.* **134**, 12485 (2012).
- [232] A. J. Siitonen, D. A. Tsyboulski, S. M. Bachilo, and R. B. Weisman, *Nano Lett.* **10**, 1595 (2010).
- [233] C. A. Silvera-Batista, R. K. Wang, P. Weinberg, and K. J. Ziegler, *PCCP* **12**, 6990 (2010).
- [234] H. Zhao and K. L. Nagy, *J. Colloid Interface Sci.* **274**, 613 (2004).
- [235] N. Denham, M. C. Holmes, and A. V. Zvelindovsky, *J. Phys. Chem. B* **115**, 1385 (2011).

Curriculum Vitae



MANASWEE SUTTIPONG

manaswee.suttipong.13@ucl.ac.uk
gmanaswee@gmail.com
+44(0)75 4783 1754

Department of Chemical Engineering
University College London
Torrington Place, London
WC1E 7JE
United Kingdom

❖ EDUCATION

Ph.D., Chemical Engineering (<i>transferred from University of Oklahoma</i>) Department of Chemical Engineering UNIVERSITY COLLEGE LONDON , London, United Kingdom	September 2016
Ph.D., Chemical Engineering School of Chemical, Biological and Materials Engineering UNIVERSITY OF OKLAHOMA , Norman, Oklahoma, United States	September 2013 <i>GPA: 3.50/4.00</i>
M.S., Petroleum Technology Petroleum and Petrochemical College CHULALONGKORN UNIVERSITY , Bangkok, Thailand	May 2011 <i>GPA: 3.56/4.00</i>
B.Eng., Petrochemical and Polymeric Materials (2 nd Class Honours) Faculty of Engineering and Industrial Technology SILPAKORN UNIVERSITY , Nakorn Pathom, Thailand	March 2009 <i>GPA: 3.24/4.00</i>

❖ RESEARCH EXPERIENCE

September 2010 – Present

Employed computer simulations to obtain molecular-level knowledge regarding the role of (1) surfactant-assisted aqueous dispersions of single-walled carbon nanotubes (SWNTs), (2) surfactant adsorption on heterogeneous surfaces, and (3) surfactant adsorption on minerals.

- A wide variety of surfactants have been investigated for stabilisation of SWNT dispersions in water. Understanding why some surfactants behave better than others at particular conditions would allow the design of novel compounds to stabilise SWNTs of desired diameter, and perhaps chirality. *All-atom molecular dynamics (MD) simulations were carried out to determine the morphology of different surfactants self-assembled on the nanotube surface.* The results suggest that the packing of surfactants depends on their molecular architecture, concentration and composition, the presence of counterion, and the nanotube diameter.
- Not much is known regarding self-assembled surfactant aggregates formed on heterogeneous surfaces. *Coarse-grained dissipative particle dynamics (DPD) simulations were performed to study the adsorption and aggregation of surfactants on patterned surfaces.* The results reveal that the adsorbed surfactant aggregates strongly depend on the morphological and chemical properties of substrates. These findings could assist in the understanding of surfactant adsorption on heterogeneous surfaces and perhaps in facilitating new methods for the fabrication of nano-structured surfaces.
- *MD simulations were used to model the interaction between aqueous Aerosol-OT (AOT) surfactants and the surface of calcite.* The results provide significant new insight into the adsorption behaviour of AOT.

June 2008 – February 2009

Conducted a research project: Biodiesel production from crude palm oil and waste cooking oil using heterogeneous catalysts.

❖ INTERNSHIP EXPERIENCE

March 2008 – May 2008

Process Engineer at Esso (Thailand) Public Co., Ltd.

❖ COMPUTER SKILLS

GROMACS, LAMMPS, Fortran, Aspen Plus®, Aspen HYSYS®, PRO/II, and Microsoft Office

❖ PUBLICATIONS

1. M. Suttipong and A. Striolo, *Doubled-Tailed AOT Surfactants Simulated on Single-Walled Carbon Nanotubes – A Molecular Dynamics Simulation Study* (2016), [in preparation].
 2. M. Suttipong, G. Brian P., and A. Striolo, *Surfactant Adsorption on Crossing Stripes and Steps* (2016), [submitted].
 3. M. Suttipong and A. Striolo, *Equimolar Mixtures of Aqueous Linear and Branched SDBS Surfactants Simulated on Single-Walled Carbon Nanotubes*, **RCS Adv.**, 5 (2015), 90049-90060.
 4. M. Suttipong, G. Brian P., and A. Striolo, *Surfactant Aggregates Templated by Lateral Confinement*, **J. Phys. Chem. B**, 119 (2015), 5467-5474. Also featured in the cover art of J. Phys. Chem. B, issue 17, 2015.
 5. M. Suttipong, G. Brian P., and A. Striolo, *Self-Assembled Surfactants on Patterned Surfaces: Confinement and Cooperative Effects on Aggregate Morphology*, **Phys. Chem. Chem. Phys.**, 16 (2014), 16388-16398. Also featured in the cover art of Phys. Chem. Chem. Phys., issue 31, 2014.
 6. M. Suttipong, N.R. Tummala, A. Striolo, B. Carlos Silvera, and F. Jeffrey, *Salt-Specific Effects in Aqueous Dispersions of Carbon Nanotubes*, **Soft Matter**, 9 (2013), 3712-3719. Also featured in the cover art of Soft Matter, issue 114, 2013.
 7. M. Suttipong, N.R. Tummala, B. Kitiyanan, and A. Striolo, *Role of Surfactant Molecular Structure on Self Assembly: Aqueous SDBS on Carbon Nanotubes*, **J. Phys. Chem. C**, 115 (2011) 17286-17296. Also featured in the cover art of J. Phys. Chem. C, issue 35, 2011.
-

❖ CONFERENCE PRESENTATIONS

1. M. Suttipong, G. Brian P., and A. Striolo, *Some Effects of Surface Heterogeneity on the Morphology of Surfactant Self-Assembled Aggregates*, The 252nd **ACS National Meeting & Exposition**, Philadelphia, PA, USA, 21st – 25th August, 2016.
2. M. Suttipong and A. Striolo, *Doubled-Tailed Surfactants Simulated on SWNTs – A Molecular Dynamics Simulation Study*, The 251st **ACS National Meeting & Exposition**, San Diego, CA, USA, 13th – 17th March, 2016.
3. M. Suttipong, G. Brian P., and A. Striolo, *Adsorption and Self-Assembly of Surfactants on Model Heterogeneous Surfaces*, **ChemEngDayUK**, University of Sheffield, Sheffield, UK, 8th – 9th April, 2015.
4. M. Suttipong, G. Brian P., and A. Striolo, *Self-Assembly of Aqueous Surfactants on Chemical and Morphological Heterogeneous Surfaces*, **AIChE Annual Meeting**, Atlanta, GA, USA, 16th – 21st November, 2014.
5. M. Suttipong, G. Brian P., and A. Striolo, *Adsorption and Self-Assembly of Surfactants on Model Heterogeneous Surfaces*, The 1st **Directed Assembly Network Summer School**, Department of Chemistry, University of Cambridge, Cambridge, UK, 6th – 11th July, 2014.
6. M. Suttipong, G. Brian P., and A. Striolo, *Self-Assembly of Aqueous Surfactants on Patterned Surfaces*, **AIChE Annual Meeting**, San Francisco, CA, USA, 3rd – 8th November, 2013.
7. M. Suttipong, T.A. Ho, and A. Striolo, *Nano-Size Particles and Lipid Membranes: What Can We Learn from Computer Modelling?*, **Outreach Seminars**, Department of Natural Sciences, Northeastern State University, Tahlequah, OK, USA, 14th November, 2012.
8. M. Suttipong, N.R. Tummala, B. Kitiyanan, and A. Striolo, *Role of Surfactant Molecular Structure on Self Assembly: Aqueous SDBS On Carbon Nanotubes*, **AIChE Annual Meeting**, Minneapolis, MN, USA, 16th – 21st October, 2011.
9. M. Suttipong, N.R. Tummala, B. Kitiyanan, and A. Striolo, *Role of Surfactant Molecular Structure on Self Assembly: Aqueous SDBS On Carbon Nanotubes*, The 2nd **Research Symposium on Petroleum, Petrochemicals, and Advanced Materials** and The 17th **PPC Symposium on Petroleum, Petrochemicals, and Polymers**, Bangkok, Thailand, 26th April, 2011.
10. M. Suttipong, N.R. Tummala, B. Kitiyanan, and A. Striolo, *Role of Surfactant Molecular Structure on Self Assembly: Aqueous SDBS On Carbon Nanotubes*, **APS March Meeting**, Dallas, TX, USA, 21st – 25th March, 2011.

❖ AWARDS AND ACTIVITIES	
Volunteer for education at the primary/secondary school, Ban Don Mun School, Nan, Thailand.	January 2012 – Present
Postgraduate teaching assistant in an event: Year 12 Summer School, Department of Chemical Engineering, University College London, London, UK.	22 nd – 26 th August 2016
Supervisor for an undergraduate student for a research project – Effect of surfactants on the hydration of fatty acids in hair fibre, Department of Chemical Engineering, University College London, London, UK.	May – July 2016
Awarded “ best presentation ” of a session: Computational Modelling & Simulations in Colloids & Surface Chemistry, The 251st ACS National Meeting & Exposition, San Diego, CA, USA.	13 th – 17 th March 2016
Demonstrator in CENG201P: Design and Professional Skills II, Department of Chemical Engineering, University College London, London, UK.	September 2015 – March 2016
Participated in Quartz Crystal Microbalance with Dissipation (QCM-D) Training.	27 th – 28 th October 2015
Postgraduate teaching assistant in an event: Chemical Engineering Summer Challenge 2015, Department of Chemical Engineering, University College London, London, UK.	16 th June – 28 th July 2015
Postgraduate teaching assistant in an event: How to Change the World, University College London, London, UK.	28 th May – 4 th June, 2015
Demonstrator in CENG2003: Process Engineering, Department of Chemical Engineering, University College London, London, UK.	January – March 2015
Supervisor for a master student for a research project – Effect of surfactants on the hydration of fatty acids in hair fibre, Department of Chemical Engineering, University College London, London, UK.	September 2014 – March 2015
Participated in the 1st Directed Assembly Network Summer School, Department of Chemistry, University of Cambridge, Cambridge, UK.	6 th – 11 th July 2014
Participated in CECAM CHARMM Tutorial, University College Dublin, Dublin, Ireland.	3 rd – 8 th June 2014
Administrator in an organisation: OU Chemical Engineering Graduate Society, School of Chemical, Biological and Materials Engineering, University of Oklahoma, Norman, OK, USA.	September 2012 – September 2013
Vice-president in an organisation: OU ThaiSA, University of Oklahoma, Norman, OK, USA.	September 2012 – September 2013
Participated in 2012 IASR Annual Conference, Institute for Applied Surfactant Research, University of Oklahoma, Norman, OK, USA.	November 2012
Demonstrator in ChE3473: Thermodynamics, School of Chemical, Biological and Materials Engineering, University of Oklahoma, Norman, OK, USA.	August – December 2012
Volunteer for the OU Big Event, University of Oklahoma, Norman, OK, USA.	3 rd March 2012
Demonstrator in ChE3473: Thermodynamics, School of Chemical, Biological and Materials Engineering, University of Oklahoma, Norman, OK, USA.	August – December 2011
Recognised in “ best student award ”, 2011 Appreciation Banquet, Petroleum and Petrochemical College, Chulalongkorn University, Bangkok, Thailand.	18 th July 2011
Awarded “ best poster presentation ”, The 2 nd Research Symposium on Petroleum, Petrochemicals and Advanced Materials and The 17 th PPC Symposium on Petroleum, Petrochemicals and Polymers, Bangkok, Thailand.	26 th April 2011
Recognised in “ first prize for the best poster presentation award ”, 2011 March Meeting of the American Physical Society, Dallas, TX, USA.	21 st – 25 th March 2011
Participated in Refining Industry, Sustainable Development and International Business Development Course, TOTAL Professor Associate.	30 th November – 4 th December, 2009
Won “ grand prize award ” Energy of Energy Efficiency Project, Esso (Thailand) Public Company Limited and Ministry of Energy Thailand.	9 th June 2008
“ One of 30 undergraduate students selected ” to participate in 2008 Esso Challenge Innovation Internship Program, Esso (Thailand) Public Co., Ltd.	March – May 2008